30k Feet Hybrid Challenge

MAE 157A - Aerospace Design Laboratory
Spring 2020

Group #3:
Team Members:
Aimee Pak
Anna Zhong
China Hagström
Jesus Legoretta
Jose Guerrero
Willy Teav

University of California, Los Angeles
Department of Mechanical and Aerospace Engineering

Contents

1 Design Challenge Overview

The Spaceport America Cup is one of the most widely participated intercollegiate rocket engineering competitions in America. Emulating the rigor of the Spaceport America Cup, the 30,000 Feet Solid/Hybrid Team Challenge called on the knowledge and creativity of the students enrolled in MAE 157A to collaborate and design from scratch a sounding rocket capable of carrying the predetermined payload to a minimum apogee of 30,000 feet and be recoverable within a 10 mile ground radius. Divided into teams comprised of 5 to 6 students, they were expected to select between building a two-stage solid fueled or single-stage hybrid fueled rocket incorporating a clean-sheet experimentally designed motor. Given an ambitious design window of 10 weeks, teams were expected to evolve from a thoughtful conceptual design to an optimized, feasible vehicle integrating elements learned from various laboratory assignments and meeting the requirements of the challenge. In the preliminary design phase, students would perform trade studies and model the trajectory of the vehicle to converge on the features and characteristics of a potential final design. Following the preliminary design checkpoint, students would refine the design of subsystems and components, performing high-fidelity analysis such as FEA and CFD to validate the viability of the rocket. Students were also expected to devise resourceful solutions in response to the limitations presented by the allotted budget and the potential disagreements arising from production and manufacturing of the conceptual design in the real world. The goal of the 30,000 Feet Solid/Hybrid Team Challenge was to test and teach students the skills of efficient collaborative design that will become invaluable moving forward in their mechanical and aerospace engineering careers.

Table 1: Design Requirements

Specified	Quantity and Unit
Apogee	30,000 ft
Launch rail length	20 ft
Min off rail speed	100 ft/s
Max cross wind speed	15 mph
Payload mass	2.2 lb
Payload diameter	3 in
Payload length	6 in
Max total impulse	9200 s
Propellant type	solid or hybrid
Feed system	pressure fed or blow down
Min FOS	1.5
Recovery system	dual-deployment parachute
Max descent velocity	50 ft/s
Max expected range	10 miles
Launch rail angle	4°
Budget	$15,000

2 Vehicle Design

2.1 Vehicle Layout

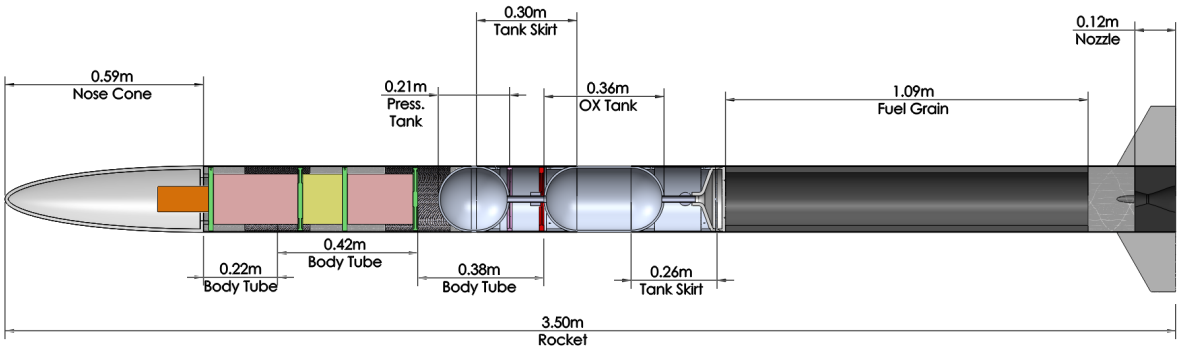

Figure 1: Cutaway View of CAD Model

The rocket was designed around the requirements outlined in Section 1. Initial sizing was conducted using an open-source model rocket simulator called OpenRocket. The rest of the sizing was performed using a custom trajectory script written in MATLAB. This is detailed more in Section 4.

The finalized design has a length of 3.5087 m and a diameter of 0.19803 meters. Out of that length, approximately 2.21 m is filled by the motor, and the remaining 1.3 m is used to house components such as the payload, avionics, and main and drogue parachutes. Figure 2 shows these components.

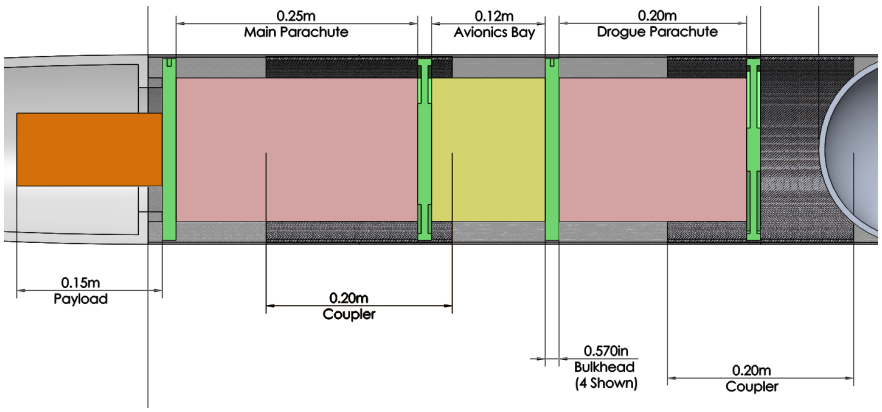

Figure 2: Components local to the nosecone

The nose cone, seen in Figure 3, is about 59.4 cm long. It has a shoulder that extends 1.5 cm out from the base. The shoulder's outer diameter is 15 cm and its inner diameter is 13 cm.

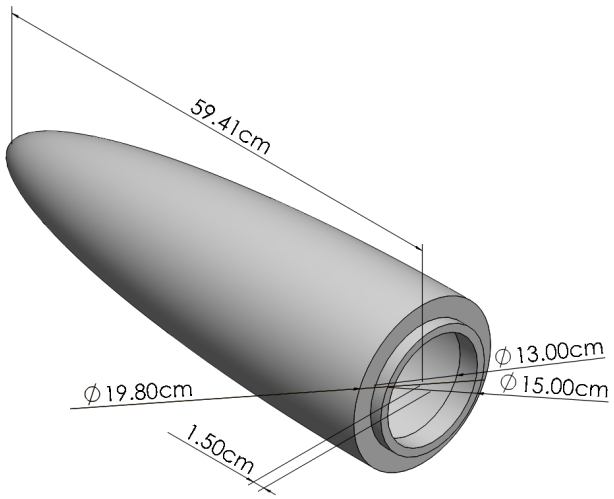

Figure 3: Nose cone

The nose cone is made of fiberglass and is hollow on the inside. It has a thickness of 1 cm. The hollow interior of the nose cone allows it to house the payload specified for the mission.

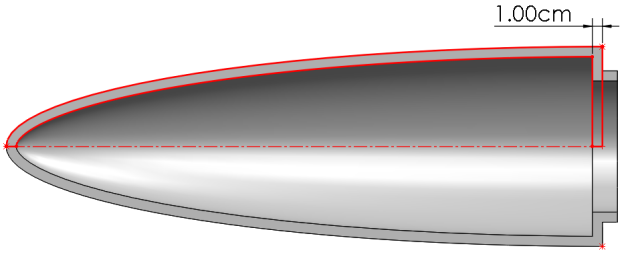

Figure 4: Nose cone cutaway view

As seen in Figure 4, the nose cone bears an elliptical profile, meaning that the curvature follows the form:

$$y = R\sqrt{1 - \left(\frac{x}{L}\right)^2} \tag{1}$$

In Equation 1, R represents the base radius, L represents the total length (excluding the shoulder), x represents the axial distance starting from the base, and y represents the local height.

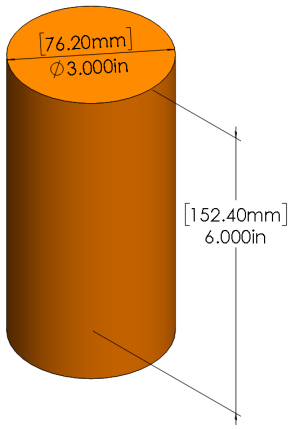

Figure 5: Payload

The dimensions of the payload were specified by the mission requirements. It has a cylindrical profile with a 3 in radius and a 6 in height. The payload weighs 2.2 lbs.

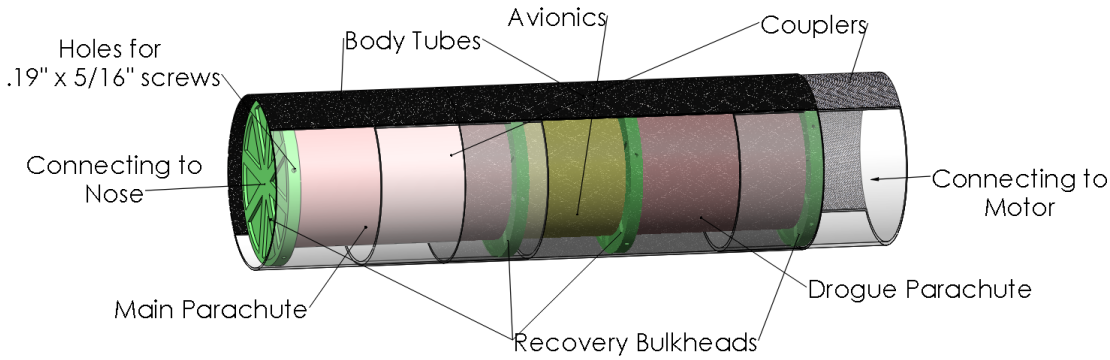

Figure 6: Section that houses avionics and parachutes

Figure 6 shows how the parachutes and avionics are stored. This rocket is designed to include a dual-deployment parachute system. The main parachute is larger and heavier than the drogue parachute. The main parachute is placed on top of the avionics bay and drogue parachute because it improves the stability of the rocket.

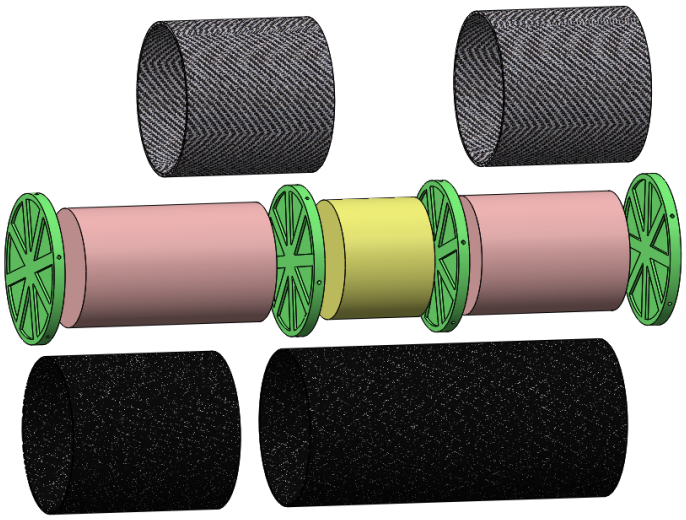

Figure 7: Exploded view of the rocket's upper section

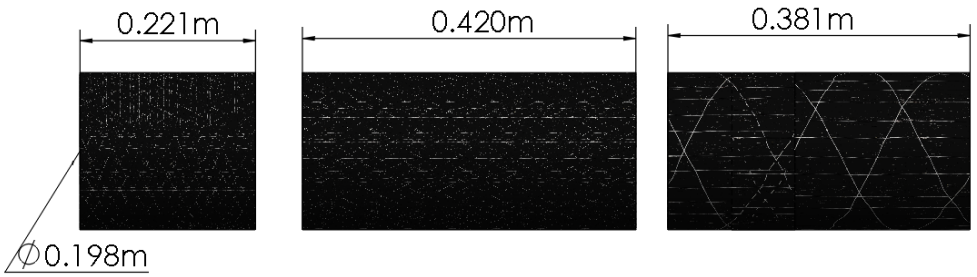

Figure 8: Body tubes

The upper section of the rocket has three body tubes that are 0.19803 m in diameter. Each body tube is made up of three layer of .0015" carbon fiber. The smallest body tube has a length of 0.221 m and is attached to the nose cone and the second body tube that is 0.420 m long. These two body tubes encompass the section showed in Figures 6 and 7. This segmentation was implemented instead of one long body tube to allow the parachutes to deploy. The 0.381 m body tube acts as a connection between the motor and the rest of the rocket. Surrounding the fuel grain is another body tube that is 1.63 m long and retains a diameter of 0.19803 m

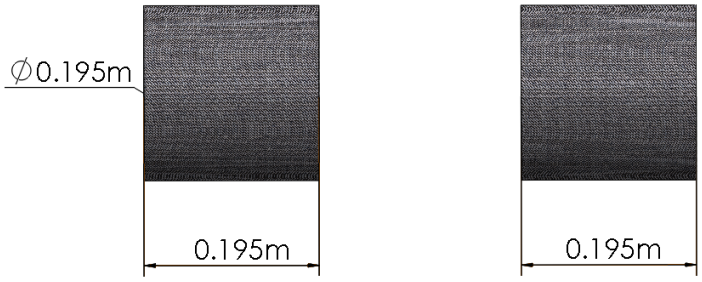

Figure 9: Couplers

The couplers are also made of carbon fiber. They have smaller diameters than the body tubes and fit inside the body tubes to help join them.

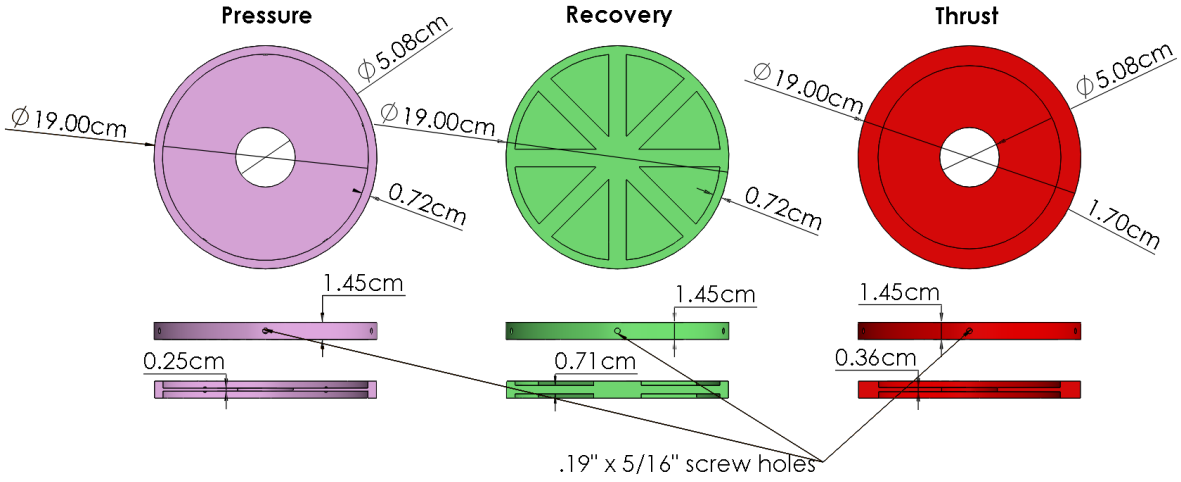

Figure 10: The bulkhead designs

This rocket contains three different bulkhead designs. Figure 10 shows that the three types are the pressure, recovery, and thrust bulkheads. Each bulkhead has the same height to accommodate the .19" diameter fasteners. The rocket contains one pressure bulkhead, one thrust bulkhead, and four recovery bulkheads. The pressure and thrust bulkheads are placed between the pressurant and oxidizer tanks. These bulkheads have a 5.08 cm diameter hole to allow valves and tubing to pass through. The recovery bulkheads is the heaviest and strongest of the bulkheads because it was designed to withstand the loads sustained from drogue deployment. All of the bulkheads are made of 6061-T6 aluminum. In these CAD models, fastening components including U-bolts were not modeled.

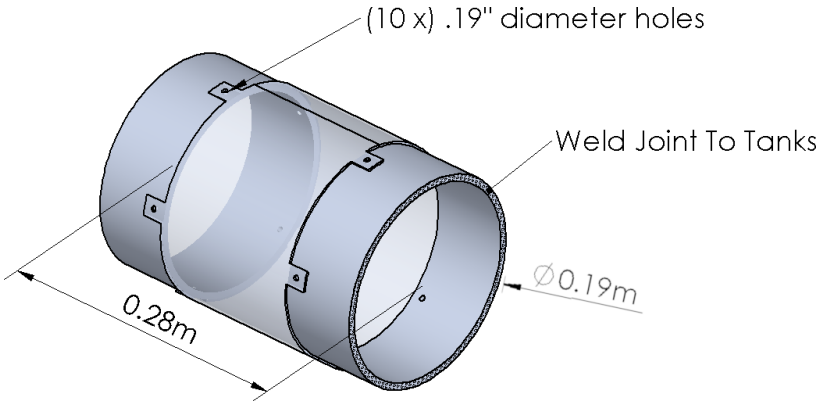

Figure 11: Tank skirts

The tank skirt, seen in Figure 11, is a structural component made of aluminum that helps connects motor components. The rocket has two tank skirts, one connects the pressurant and oxidizer tank, the other connects the oxidizer tank to the injector. The tank skirt is made from two hollow aluminum tubes that are welded to the tank components and two sheets of aluminum that are fastened to the tubes.

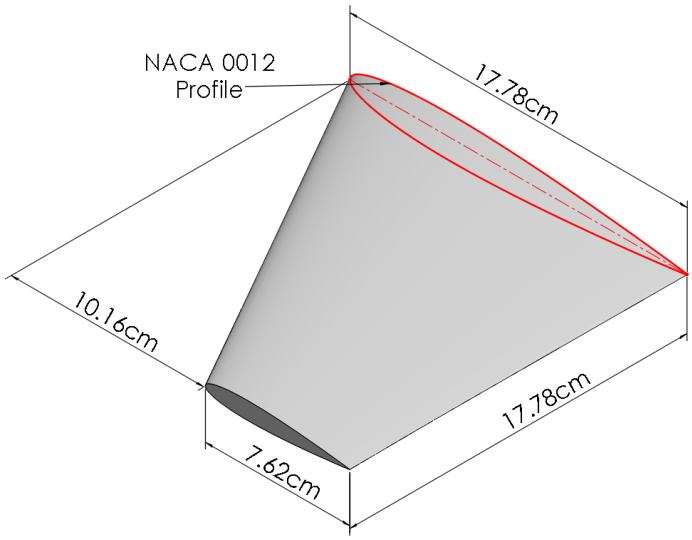

Figure 12: Fins

Figure 12 shows one of the rocket's fins. The rocket has 4 fins placed in a symmetrically around the base of the rocket. They are constructed using a plywood core and fiberglass. The fins attach to a fin can, which isn't modeled. The fin is trapezoidal and has a NACA 0012 airfoil profile. The airfoil chosen is symmetric and will not generate unnecessary forces on the rocket. The fin parameters were determined from the stability code. Section 4.3 goes into more detail on how the fin was dimensionalized to fit the static margin requirements.

Table 2: Materials of Major Components

Material	Components
Fiberglass	Nose Cone, Fins
Carbon Fiber	Body Tubes, Couplers
6061 Aluminum	Pressurant Tank, Ox Tank, Bulkheads
Mild Steel	Combustion Chamber

As Table 2 shows, this design utilized a lot of composite materials to reduce weight without sacrificing too much strength. Plenty of aluminum was also used. Section 5.1 goes more in depth with material selection.

2.2 Mass Estimate List

The mass estimate list (MEL) below was partitioned into 6 sections: main subsystem overview, structures, propulsion (inert), propellant, electronics, and recovery. Masses calculated were based on the max estimated value (MEV). Two steps were used to determine the MEV of a component. The method consisted of multiplying the entered current best estimate (CBE) by a percentage contingency value determined by entry type and adding the contingency value to the entered CBE. The possible entry types were Analysis, Historical, Measurement, or Guess, with contingency percentages of 8.0, 15.0, 5.0, 25.0, respectively.

Table 3: Mass Estimates for Major Subsystems

Subsystem	MEV (kg)	Percent Change from PDR
Structures	11.44	-4.54
Propulsion	9.94	-13.24
Propellant	19.71	2.85
Electronics	1.90	0.49
Recovery	5.28	1.70

Table 4: Mass Estimates for Structures

Component	MEV (kg)
Nosecone	4.80
Bulkheads	1.08
Bodytubes	1.15
Bolts and Fasteners	1.15
Fin	2.82
Rail Guides	0.26
Couplers	0.25

Table 5: Mass Estimates for Inert Propulsion

Component	MEV (kg)
Pressurant Tank	3.18
LOX Tank	1.79
Combustion Chamber	2.30
Injector	1.21
Nozzle	1.74

Table 6: Mass Estimates for Propellant

Component	MEV (kg)
LOX	10.94
Fuel	8.77

Table 7: Mass Estimates for Electronics

Component	MEV (kg)
Payload	1.05
Avionics Housing	0.57
Avionic Electronics	0.28

Table 8: Mass Estimates for Recovery

Component	MEV (kg)
CO2	0.06
Recovery Avionics	1.13
Main Chute	0.96
Drogue Chute	0.18
Shock Cords	1.84

3 Motor Design

The major components of the motor were designed in the following sequence with feedback at most steps and multiple iterations performed in the process. CEA analyses were performed on various propellant compositions for propellant trade studies and determining combustion chamber conditions. A pressure drop from the oxidizer tank to the combustion chamber was assigned and used to size the pressurant gas tank. From the CEA trade studies, performance parameters were obtained to predict apogee and to design the geometry of the nozzle. A second pressure drop from the Ox tank to the combustion chamber was assigned to design the injector. The propellant that yielded the best apogee with acceptable length-to-diameter ratio and static margin was selected and a final design iteration was done.

3.1 Overview

Major component material, weight, performance parameters, and dimensions of the motor are shown in the following figures and tables.

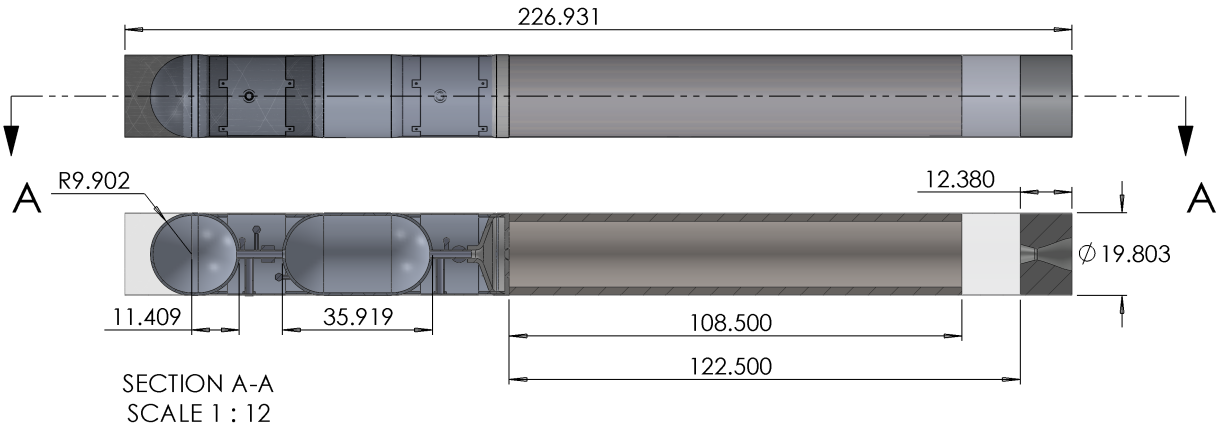

Figure 13: Dimension CAD drawing of the motor in centimeters

Table 9: Material selection for the major components of the motor

Component	Material
Pressurant Tank	Al 6061
Ox Tank	Al 6061
Injector	Stainless steel
Fuel Grain	HTPB/Paraffin
Combustion Chamber	Mild Steel
Nozzle	Graphite

Table 10: Structural mass of major motor components

Component	Mass (kg)
Propellant	14.3490
Combustion Chamber	2.1886
Oxidizer Tank	1.6558
Pressurant Tank	2.9457
Nozzle	1.660

Table 11: Operating conditions and performance parameters

Performance Parameter	Quantity and Unit
C-Chamber Pressure	800 Psi
Oxidizer Tank Pressure	850 Psi
Gas Tank Pressure	2550 Psi
OF	2.4
Isp	290.8250 s
C*	1780.8 m/s
C_F	1.6021
Jet Thrust	5202.5 N
Burn time	7.79 s
$\dot{m}_{ox}$	1.2872
$\dot{m}_f$	0.5363

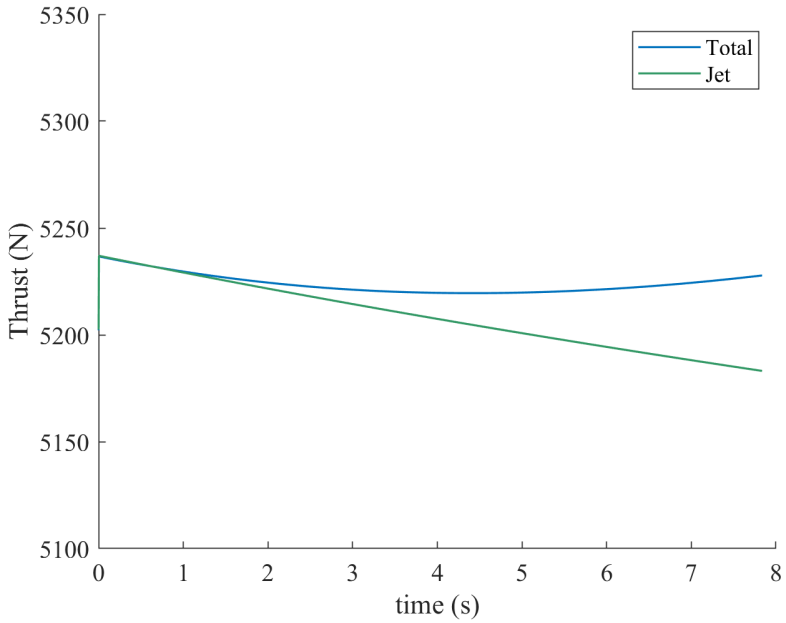

Figure 14: Motor Thrust Curve

3.2 Propellant and Combustion Chamber

The original intended motor design was to have a blow down process with nitrous oxide as the oxidizer due to its high vapor pressure at operating conditions and HTPB or Paraffin as the fuel grain. This design was changed due to the complexity in modeling the time variation of the combustion chamber properties. The hybrid rocket is instead designed as a pressure feed system with liquid oxygen (LOx) as the oxidizer and nitrogen (N_2) as the pressurant.

Propellant trade studies were done to determine the best fuel for our requirements. From Figures 15 - 16, it is clear that Paraffin has superior performance to HTPB. However, Paraffin is a wax and is hard to manufacture. Additionally, it can break away during combustion and cause instabilities. HTPB also has limitations of having a slow burn rate. As a result, the length of the propellant can become too long. Regression rate coefficients for both fuels are given in Table 12 taken from Pastrone [1]. For the reasons described above, a composite fuel grain made of Paraffin wax and HTPB was selected for the fuel grain.

Table 12: Regression rate coefficients for St. Roberts Law, Equation 8

Fuel	a	n
HTPB	$8.7 * 10^{-5}$	0.530
Paraffin	$9.1 * 10^{-5}$	0.690

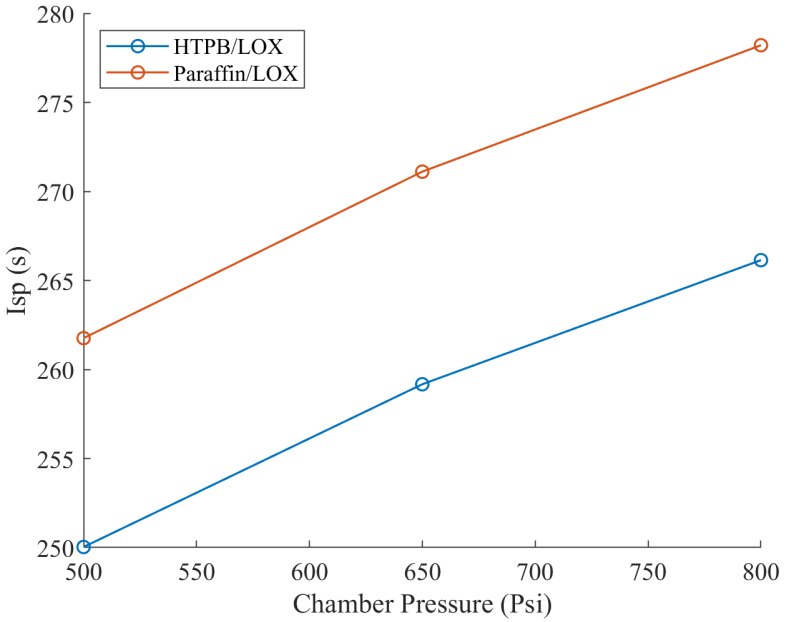

Figure 15: Performance of propellants with constant OF ratio obtained from CEA

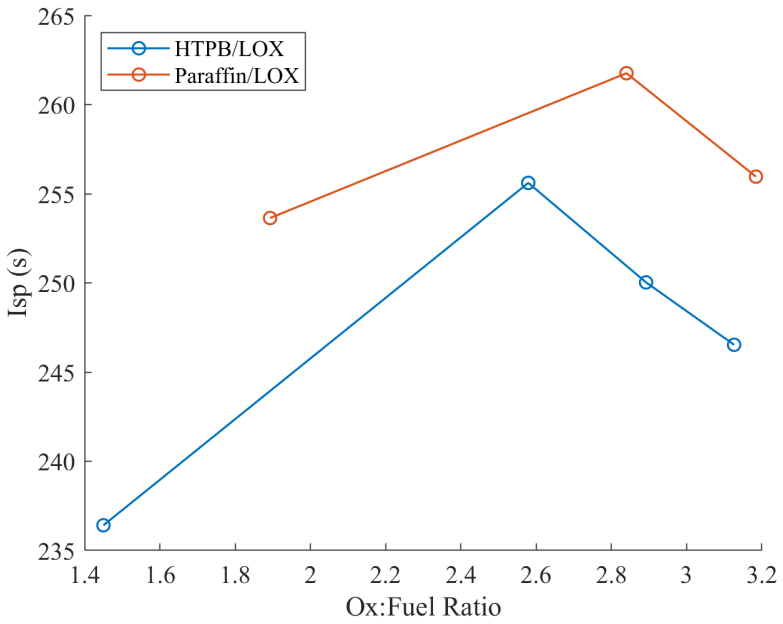

Figure 16: Performance of propellants with constant combustion chamber pressure obtained from CEA

In addition to Figures 15 - 16, other parameters were obtained from CEA such as nozzle area ratios (Ae/At), thrust coefficient (C_F), and characteristic velocity (C^*). These parameters were inputs to the trajectory code and used to determine apogee and other performance parameters (i.e. $\dot{m}$, T, etc.). The design was optimized and a fuel grain length was selected by iterating the rocket diameter and nozzle exit area with varying propellant weight compositions, OF ratios, and combustion chamber pressures from CEA. This process is detailed next.

The selection of the OF ratio was based on Figures 17 and 18. The parameter of interest to be optimized was I_{sp}. Thus, two cases were selected for further analysis: 50-50 HTPB-Paraffin combination with an OF ratio of 2.4 and 80-20 HTPB-Paraffin combination with an OF ratio of 2.6.

The total mass flow rate out of the nozzle is given by Equation 2.

$$\dot{m}_{tot} = \frac{P_c A_t}{C^*} \tag{2}$$

The fuel and oxidizer mass flow rates can be determined from the OF ratio using Equations 3 and 4.

$$\dot{m}_f = \frac{1}{OF+1}\dot{m}_{tot} \tag{3}$$

$$\dot{m}_{ox} = \frac{OF}{OF+1}\dot{m}_{tot} \tag{4}$$

The propellant mass is obtained from the total impulse constraint ($I_{tot} = 9200$ s) using Equation 5.

$$M_{prop} = \frac{I_{tot}}{I_{sp}} \tag{5}$$

Thrust is given by Equation 6.

$$T = P_c A_t C_F = C_F C^* \dot{m}_{tot} \tag{6}$$

With the calculated propellant mass and thrust, the fuel grain can be sized. By replacing $\dot{m}_{tot}$ in Equation 3 by M_{prop}, the fuel mass (m_f) can be determined. The length and thickness of the propellant must be

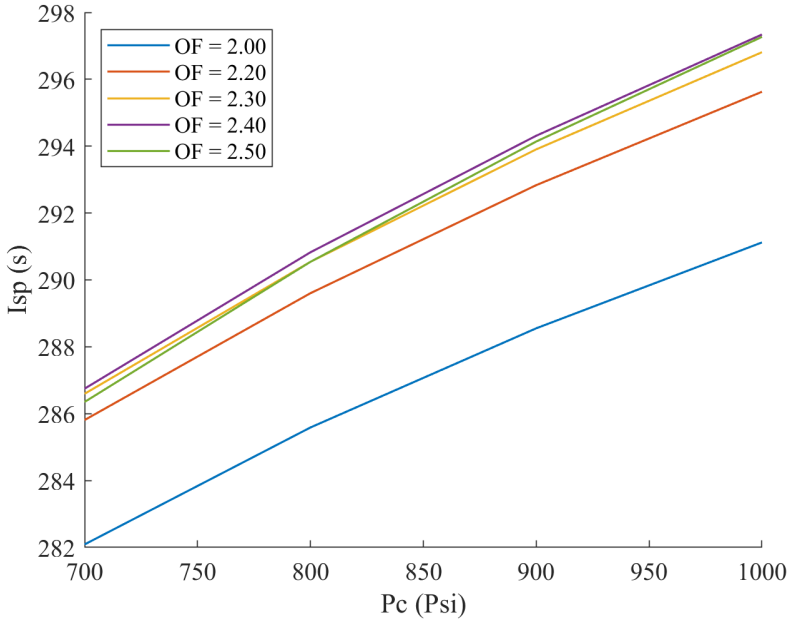

Figure 17: Constant OF ratio lines plotted for varying Isp and Pc - Fuel Composition 50% HTPB 50% Paraffin by weight

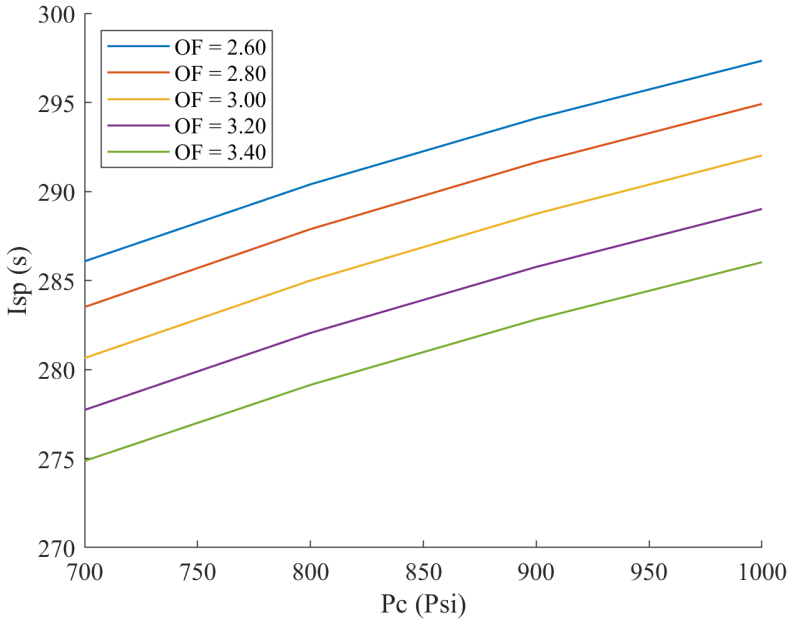

Figure 18: Constant OF ratio lines plotted for varying Isp and Pc - Fuel Composition 80% HTPB 20% Paraffin by weight

designed such that Equation 3 is satisfied.

The heat transfer rate to the combustion chamber walls is now considered. Modeling the fuel grain as a semi-infinite solid, Equation 7 can be used to determine the thickness of the unburnt fuel. The outer

diameter of the burned fuel is then determined by the inner diameter of the combustion chamber and the thickness of the unburnt fuel.

$$T(x,t) = T_s + (T_i - T_s)\,\mathrm{erf}\left(\frac{x}{2\sqrt{\alpha t}}\right) \tag{7}$$

where $T(x,t)$ is the temperature at time t and depth x from the surface and T_s is the applied surface temperature which in this case is assumed to be 1/2 the combustion chamber temperature. α is the thermal diffusivity of the fuel grain. Assuming T_i is 300 K, the depth x at the burn time must be calculated such that $T(x, t_{burn})$ is equal to 300 K. An adequate margin of safety was applied to ensure success. The model is not accurate since the diameter is not large enough to be considered a plate or semi-infinite. In reality $T(x, t_{burn})$ could have been set to 900 K since mild steel fails around 1100 K. From Figure 19 the unburnt fuel grain thickness is 0.816 cm.

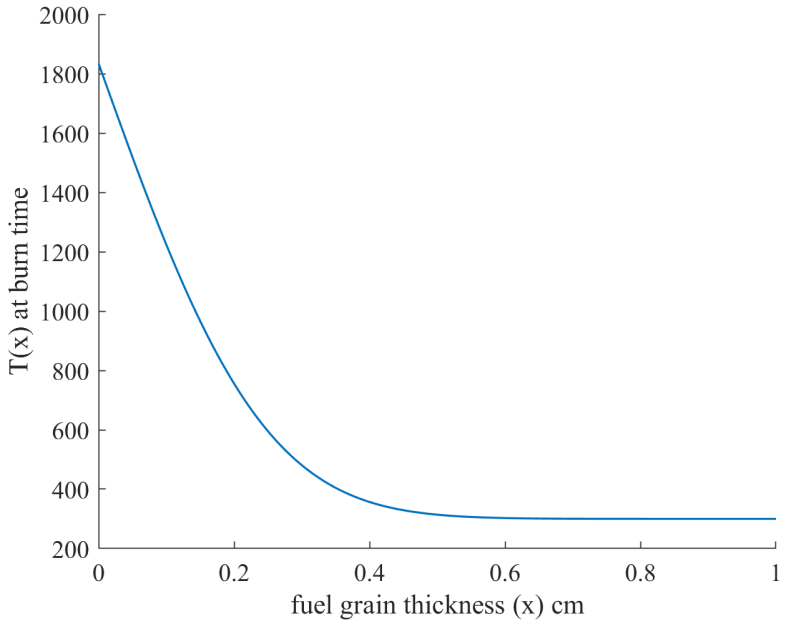

Figure 19: Temperature at a depth x at burn time for a 50-50 wt% fuel composition

Analysis for the inner diameter and the length of the fuel grain are now presented. For a hybrid, the fuel regression rate is given by St. Roberts Law, Equation 8.

$$\dot{r} = aG_{ox}^{n} \tag{8}$$

where a and n are the regression rate coefficients for the fuel grain and G_{ox} is the oxidizer mass flow rate flux. The fuel mass flow rate into the combustion chamber is given by Equation 9.

$$\dot{m}_f = \dot{r}\rho_f A_b \tag{9}$$

where ρ_f is the fuel density and A_b is the burn area. For a cylindrical fuel grain, Equation 9 becomes

$$\dot{m}_f = \dot{r}\rho_f \pi D L \tag{10}$$

Expressing $\dot{m}_f$ as a function of $\dot{m}_{ox}$ and solving for the fuel grain length, L_1

$$L_1 = \frac{\dot{m}_{ox}/OF}{\dot{r}\rho_f \pi \bar{D}} \tag{11}$$

$$\bar{D} = \frac{D_o + D_i}{2} \tag{12}$$

$$G_{ox} = \frac{\dot{m}_{ox}}{\bar{A}_c} \tag{13}$$

$$\bar{A}_c = \frac{\pi}{4}\bar{D}^2 \tag{14}$$

where $\bar{D}$ is the average of the outer and inner diameter of the fuel grain. Using the mass of the fuel to get a second expression for fuel grain length, L_2

$$L_2 = \frac{4m_f}{\pi\rho_f(D_o^2 - D_i^2)} \tag{15}$$

where D_o is the outer diameter of the burned fuel. Solving Equations 11 - 15 by varying D_i and minimizing the difference, $|L_1 - L_2|$, the fuel grain length can be obtained.

With the known propellant length, thrust, and propellant mass, the nozzle exit diameter and rocket diameter were iterated and the above parameters were calculated. Based on the apogee obtained, fuel grain length, static margins, and L/D ratio, a propellant weight composition, P_c, and nozzle exit diameter were chosen. The final propellant composition was the 50-50 wt% HTPB-Paraffin with a combustion chamber pressure of 800 Psi and a Jet Thrust of 5205.5 N. Figures 20 and 21 demonstrate this process. The final fuel grain geometry is given in Figure 22 and the final burn diameter of the fuel grain is 17.71 cm.

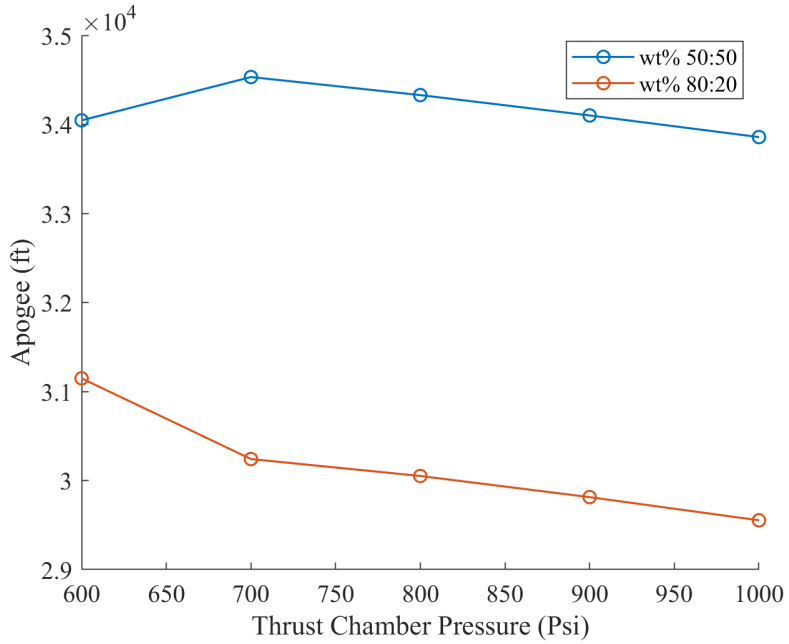

Figure 20: Performance of propellants with constant OF ratio obtained from CEA

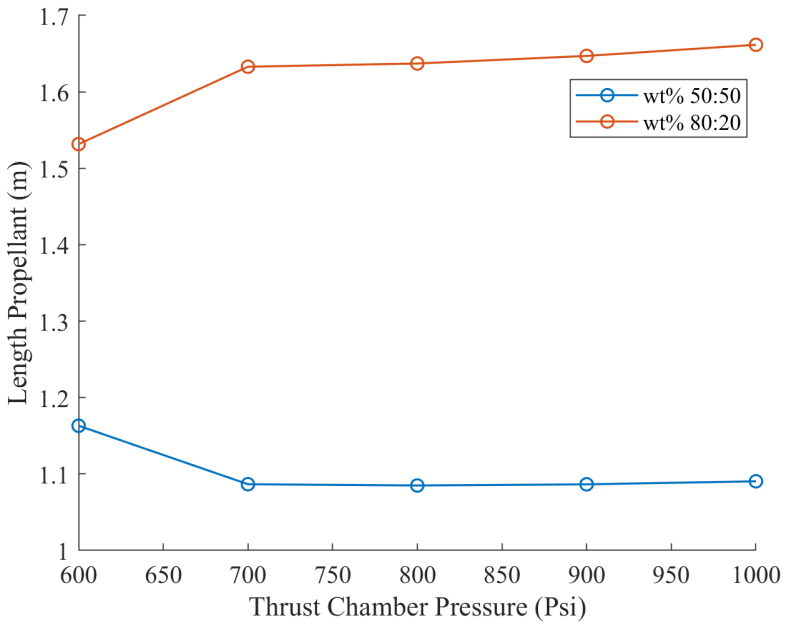

Figure 21: Performance of propellants with constant OF ratio obtained from CEA

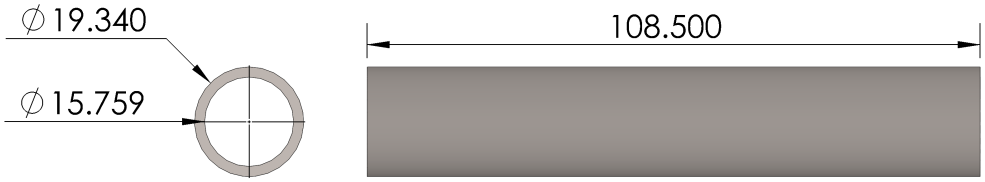

Figure 22: Fuel grain geometry in cm

After the fuel grain was sized, a 14 cm post combustion chamber was added to achieve a more efficient combustion of the gasses prior to entering the nozzle. The thickness of the combustion chamber was determined using Equation 16 which will be derived in Section 3.3.

$$t = \frac{P_c \cdot FOS}{2\sigma_y} \tag{16}$$

Figures 23 and 24 show how the mass flow rates, OF ratio, burn area and regression rate vary with time in the combustion chamber. The burn area can be seen to increase which is expected since there is a progressive burn. The OF ratio also increases. Although, the burn area is increasing, it can be seen that the fuel regression rate is decreasing. Overall, the fuel mass flow rate is decreasing.

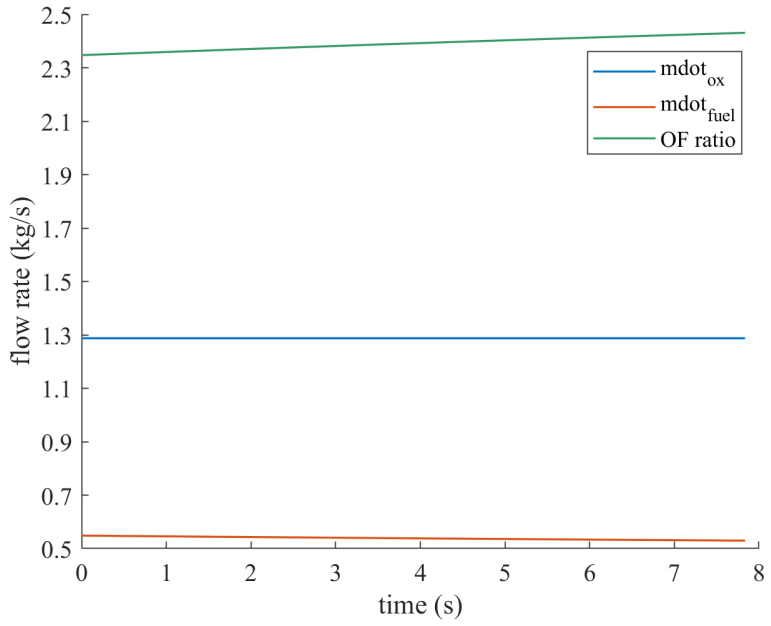

Figure 23

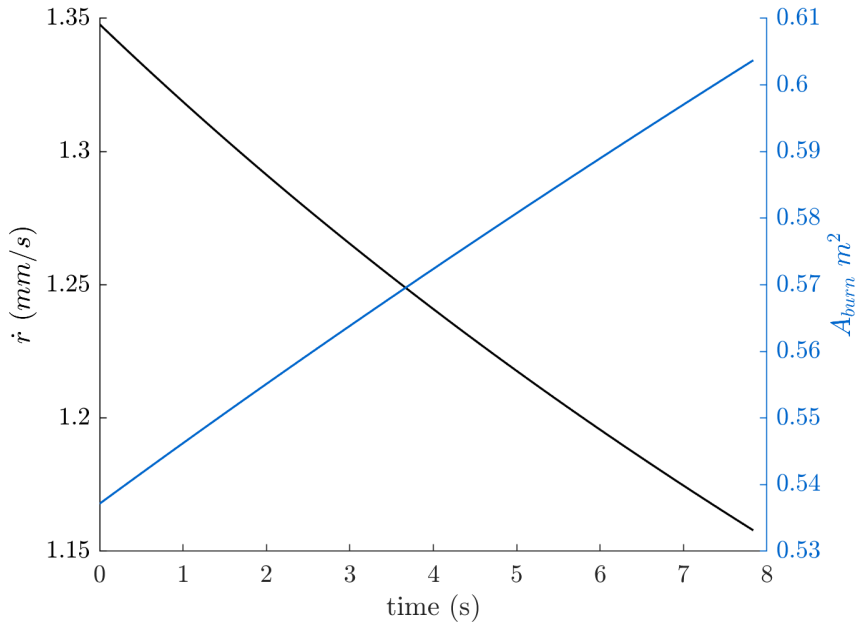

Figure 24: Burn area and fuel regression rate over burn time

3.3 Oxidizer Tank

The oxidizer tank was the simplest component of the motor to design. From the propellant mass and the OF ratio, replacing $\dot{m}_{tot}$ in Equation 4 by M_{prop}, the oxidizer mass can be determined. Using the density of LOx, the volume of the tank can be calculated. Setting the outer diameter of the tank equal to the rocket outer diameter and having spherical caps, the oxidizer tank is fully defined. The pressure of the oxidizer tank was set to 50 Psi above the desired combustion chamber pressure.

From the oxidizer tank pressure, $P_{ox} = 850\ Psi$, and the material selection, the thickness of the tank was determined based on a FOS of 1.5 and max stress. In a cylindrical or spherical tank, the maximum stress developed is the hoop stress (σ_θ).

$$\sigma_\theta = \frac{P_{ox} D}{2t} \tag{17}$$

$$FOS = \frac{\sigma_y}{\sigma_\theta} \tag{18}$$

Equations 17 and 18 can be solved for the required thickness.

$$t = \frac{P_{ox} D \cdot FOS}{2\sigma_y} \tag{19}$$

3.4 Pressurant Gas Tank

Two pressurizing gasses were considered for the pressurant gas tank, nitrogen and helium. The sizing of the tanks was based on the analysis presented in Sutton & Biblarz [2].

Table 13: Physical properties of gasses

Gas	Molecular Weight (kg/kmol)	Density (kg/m^3)	k = C_p/C_v
Nitrogen	4.0026	1.25	1.4
Helium	28.0134	0.1785	1.86

For an isentropic expansion of the pressurant gas, the required initial volume to achieve the final pressure P_{ox} in the oxidizer tank is given by Equation 20.

$$V_0 = \frac{V_{ox}}{(P_0/P_{ox})^{1/k} - 1} \tag{20}$$

The subscript 0 refers to the initial conditions of the pressurant tank and the subscript g refers to the final conditions of the pressurant gas tank. The mass required can then be obtained using ideal gas law.

$$m_0 = \frac{P_0}{RT_0} V_0 \tag{21}$$

Figure 25 shows that if helium and nitrogen are both pressurized to the same pressure, then less helium mass is required to achieve the same final pressure in the oxidizer tank. It also shows that as the pressure increases, less gas mass is required to achieve the desired pressure at the oxidizer tank. Figure 26 shows that the lower mass requirement of helium is offset by its need for a larger volume. The cost of helium is also about 13 times greater than that of nitrogen. For these reasons, it is cheaper to increase the pressure in the gas tank such that the mass of the gas requirement decreases. The cost benefit of cheaper nitrogen gas is still greater even when the wall thickness increases due to increasing initial pressure. The initial pressure, P_0, was selected to be three times that of the oxidizer pressure since there was no benefit when pressure was greater than this point. The final designed pressure was $P_0 = 2550$ Psi, and the thickness was calculated similar to that of the oxidizer tank.

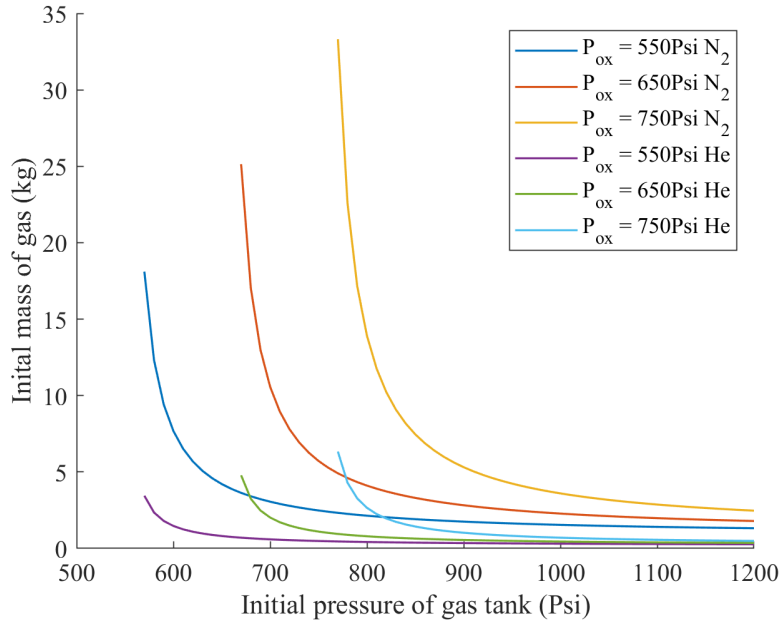

Figure 25: Effects of P_0 on the mass required m_0 to achieve a final pressure P_{ox} in the oxidizer tank

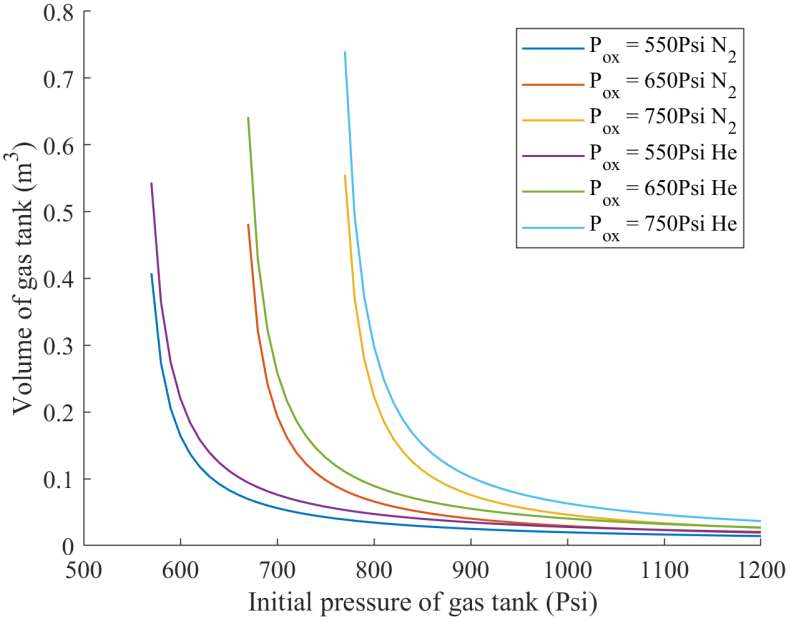

Figure 26: Effects of P_0 on the volume required V_0 to achieve a final pressure P_{ox} in the oxidizer tank

3.5 Nozzle

The nozzle for the rocket is a converging conical, diverging bell nozzle. A simplified dimensioned drawing of the nozzle is given in Figure 27. A more detailed drawing is given in Appendix D.9. The nozzle will be made out of graphite for its high temperature capabilities. Its melting temperature is about 3870 K, and its heat capacity is 8.517 J/mol-K. From CEA analysis, the adiabatic flame temperature at the inlet, throat, and exit are 2668 K, 3482 K, and 2405 K, respectively. Since all three temperatures are within the working temperature of graphite, nozzle cooling is not necessary. The downsides of graphite is that it is expensive and its brittleness can pose a challenge for manufacturing. The outer diameter of the nozzle component is 19.40 cm. Its total length is 12.38 cm. To find the required nozzle exit area and throat area ratio, A_e/A_t, CEA analysis was performed with the selected propellant combination and combustion chamber pressure of 800 Psi. The nozzle A_e/A_t was computed as 8.3607 perfectly expanded at sea level. The nozzle outlet diameter was iterated through different possibilities in the trajectory MATLAB script, with the final outlet diameter being 7.920 cm. Thus, the throat diameter was 2.740 cm.

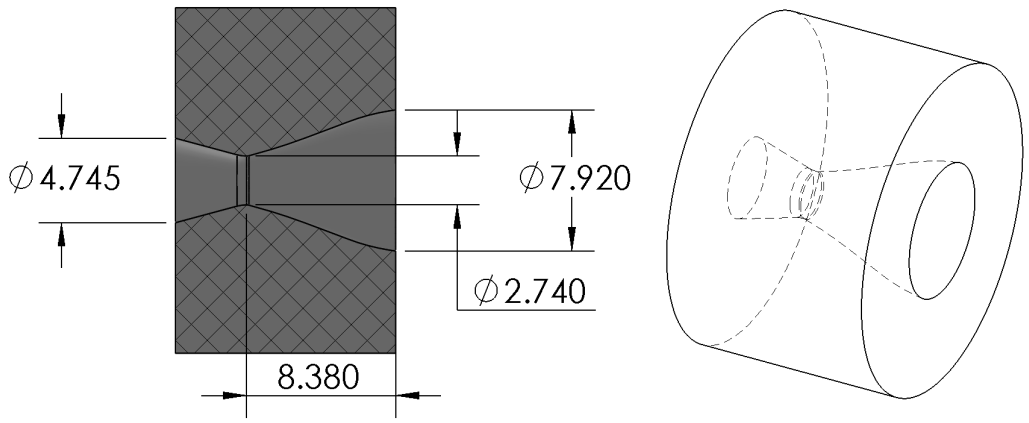

Figure 27: Dimensioned nozzle drawing in cm

The bell nozzle parabolic approximation procedures suggested by G. V. R. Rao were used to design the bell contour. The bell shape dimension rules are given in Appendix A. Point N is defined as the starting point of the bell curve and point E is defined as at the nozzle exit. Assuming the diverging angle for a conical section was 17.5°, the length of the supposed diverging conical section, $L_{con,div}$, was calculated as

$$L_{con,div} = \frac{R_t(\sqrt{A_e/A_t} - 1) + R_t/2(\sec(\theta) - 1)}{\tan(\theta)} \tag{22}$$

Thus, $L_{con,div}$ was 8.244 cm from point N to point E. Including the circle arcs that shape the throat of the nozzle, the total length of the diverging section is 8.380 cm. Using 100% of $L_{con,div}$ to define the parabolic profile of the nozzle on the parabolic angles reference graph given in Appendix A, the initial parabolic angle, θ_n and the final parabolic angle, θ_e was estimated to be 20° and 7°, respectively. With these parameters, the parabolic curve of the bell nozzle radius, y can be found as a function of axial position, x and unknowns, P, Q, S, and T

$$y = Px + Q + (Sx + T)^{1/2} \tag{23}$$

where the four boundary conditions to solve for the unknowns are

1) $x_N = y_N = 0$
2) $x_E = L_n - 0.382R_t\sin(\theta_n)$
   $y_E = R_t\sqrt{\frac{A_e}{A_t}} - R_t - 0.382R_t(1 - \cos(\theta_n))$
3) $y(x)$ must be tangent to θ_n at point N
4) $y(x)$ must be tangent to θ_e at point E

where x_N is the axial position of bell nozzle and y_N is the radial position of the bell nozzle curve. Solving for the unknowns P, Q, S, and T, the parabolic curve of the bell nozzle was defined as

$$y = 0.4356x - 1.2123 + (-0.1736x + 1.4697)^{1/2}$$

The bell contour was plotted in MATLAB and is given in Figure 28.

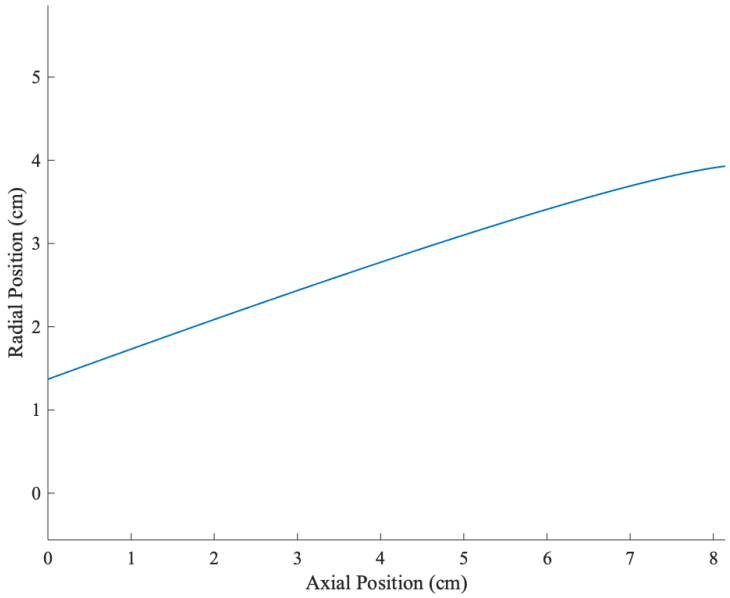

Figure 28: Bell contour

The converging conical section has a set inlet area to throat area ratio, A_i/A_t of 3 with a 15° half angle. Knowing the throat diameter, the inlet diameter, D_i was calculated as follows

$$D_i = \sqrt{\frac{D_t^2}{A_t/A_i}} \tag{24}$$

Thus, the inlet diameter was 4.745 cm. With the 15° half angle, the converging section length of 3.466 cm.

3.6 Injector

The LOx injector was designed with self-impinging geometry with the holes at a 30° angle from the centerline. A simplified dimensioned drawing of the injector is shown in Figure 29. A more detailed drawing is given

Table 14: Nozzle Properties Summary

Property	Quantity and Unit
Material	Graphite
A_e/A_t	8.3607
Expansion Altitude	Sea Level
Diverging Length	8.380 cm
θ_e	20 degrees
θ_n	7 degrees

in Appendix D.8. The injector is made out of 304 stainless steel for its ability to withstand cryogenic temperatures. It has higher tensile strengths at cryogenic temperatures than at ambient temperatures. [3] The injector is two separate parts that will be welded together: the injector plate and the injector housing. The design of the injector began with the total mass flow rate of oxidizer required for the hybrid rocket. From the custom iterative script to find the ideal rocket parameters, the oxidizer mass flow rate was calculated to be 1.2872 kg/s. This is flow from the oxidizer into the injector inlet that is 2 cm in diameter. The flow velocity into the injector is calculated from the mass flow rate, $\dot{m}_{ox}$

$$v = \frac{\dot{m}_{ox}}{\rho_{ox} A_{inlet}} \tag{25}$$

Thus, the inlet velocity is 1.6 m/s. The required feed area, A_{feed} of the injector into the combustion chamber was calculate using mass flow rate conservation. The flow rate out of the nozzle, $\dot{m}_{tot}$ had to equal the flow rate of the oxidizer, $\dot{m}_{ox}$ and the fuel grain, $\dot{m}_f$

$$\dot{m}_{tot} = \dot{m}_{ox} + \dot{m}_f \tag{26}$$

where

$$\dot{m}_{tot} = \frac{P_c A_t}{C^*} \tag{27}$$

$$\dot{m}_{ox} = C_d A_{feed} \sqrt{2\rho_{ox}(P_{ox} - P_c)} \tag{28}$$

$$\dot{m}_f = 2\pi \bar{R} L \rho_f \dot{r} \tag{29}$$

$$\dot{r} = a G_{ox}^n \tag{30}$$

$$G_{ox} = \frac{\dot{m}_{ox}}{\pi \bar{R}^2} \tag{31}$$

where P_c is the pressure of the combustion chamber at 800 Psi, C^* is the reference velocity of 1780.8 m/s found from CEA analysis, C_d is the discharge coefficient set to 0.8, $\bar{R}$ is the average radius of the fuel grain during the burn, L is the length of the fuel grain at 1.085 m, $\dot{r}$ is the fuel regression rate, G_{ox} is the oxidizer mass flux. The pressure drop across the injector was defined as 50 Psi.

Iterating through injector hole diameters with a set number of holes at 36, the optimized hole diameter was 0.14 cm giving a total injector feed area of $0.574\,\text{cm}^2$. The exit velocity through each hole is is 19.7 m/s. The injector was designed to have three rows of 12 holes that are evenly spaced circumferentially 60° apart.

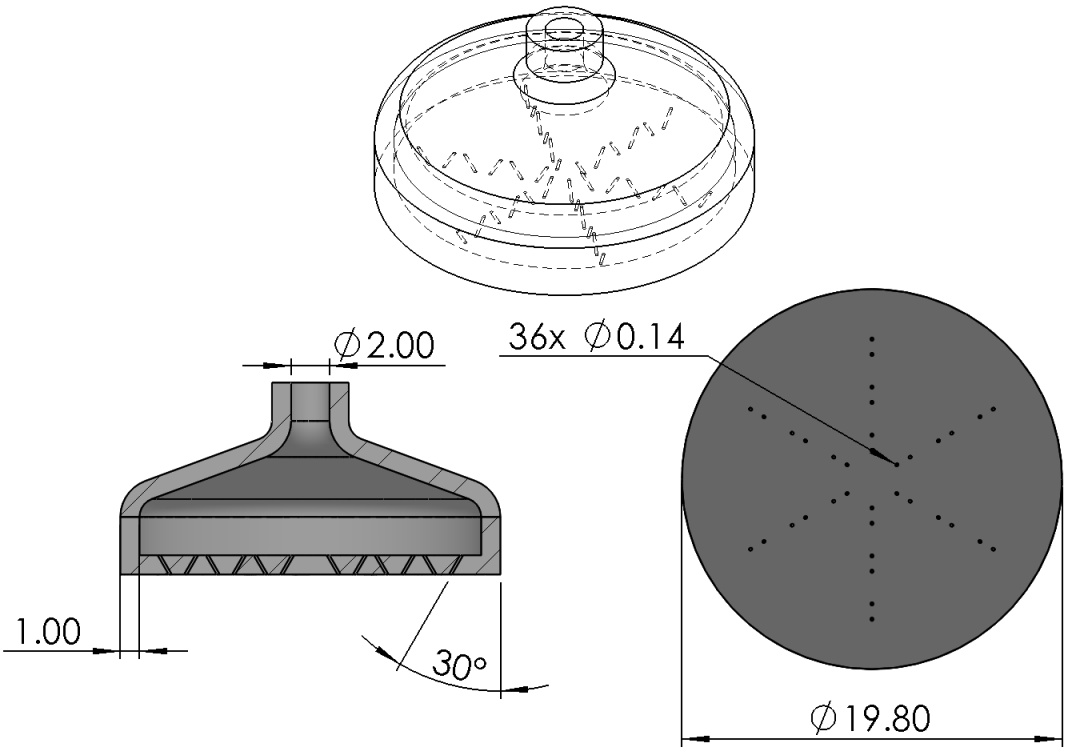

Figure 29: Dimensioned injector drawing in cm

Table 15: Injector Properties Summary

Property	Quantity and Unit
Material	Stainless Steel
$\dot{m}_{ox}$	1.2872 kg/s
Velocity at Injector Inlet	1.6 m/s
Velocity at Injector hole	19.7 m/s
P_{ox}	850 Psi
$\Delta P_{injector}$	50 Psi
Number of holes	36
C_d	0.8
Hole Diameter	1.4 mm
Injector Angle	30°
Afeed	57.4 mm^2

3.7 Plumbing & Instrumentation

The Plumbing & Instrumentation Diagram (P&ID) of the hybrid rocket is given in Figure 30. The CAD of the plumbing inside the rocket with relative positions is given in Figure 31. The rocket pressurant is nitrogen and the oxidizer is liquid oxygen. The filling process starts from the respective dewar tanks with a manual needle valve. The pressure gauge is used to read the pressure inside the dewars. An electronically controlled normally closed solenoid valve will be used to start and stop the tank filling. The pressurant tank

will be filled to 2550 Psi and the oxidizer tank will be filled to 850 Psi. The pressure relief is used to release nitrogen or LOx into the atmosphere if there is a pressure buildup due to ambient temperature conditions. The check valve is to ensure the filling process is only from the dewars to the rocket. Reverse flow is not desired. There are a quick releases on the outer diameter of the rocket that will allow the fill lines to break off once the rocket is launched rather than needing a person go up to a pressurized rocket to disconnect the fill lines. Inside the rocket, both the pressurant and oxidizer lines have a pressure transducers to send out pressure readings. Pressure relief valves are also in the rocket. A latched door will be on the rocket wall to allow proper pressure relief into the atmosphere. The pressurant to oxidizer tank fill is controlled by a pressure regulator that will maintain a constant 850 Psi inside the oxidizer tank. The oxidizer flow will be controlled by a pneumatic valve for a constant 1.287 kg/s mass flow rate into the injector. It is important to note that all plumbing components for the LOx are rated for cryogenic temperatures.

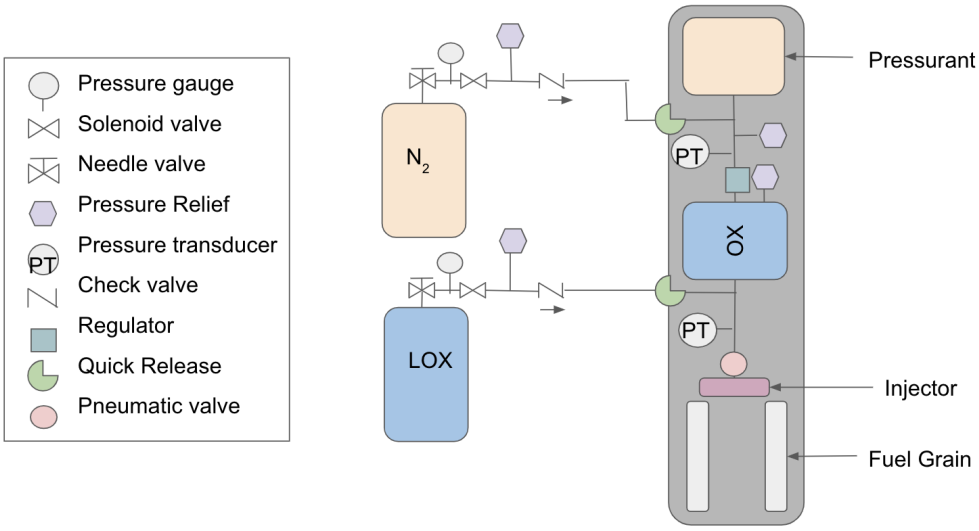

Figure 30: Plumbing & instrumentation diagram

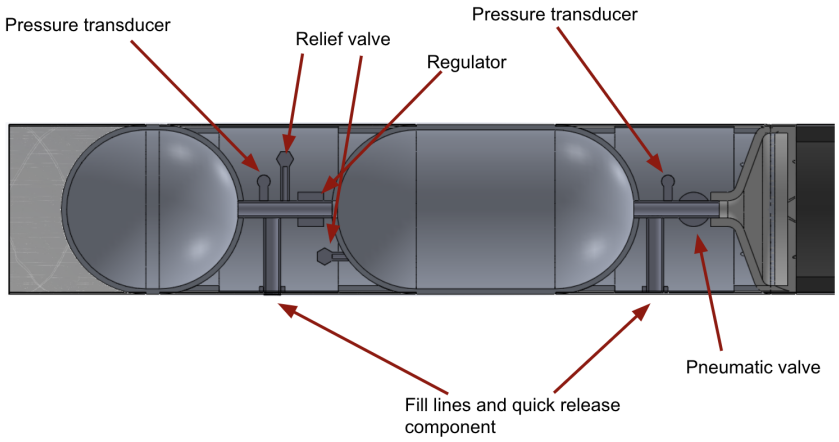

Figure 31: Plumbing inside the rocket

4 Trajectory & Stability

4.1 Trajectory

To derive the equations of motion for the trajectory of the rocket, the forces acting on the rocket were analyzed as shown in the free body-diagram in Figure 32. The x-axis is defined along the axis of the rocket and the y-axis perpendicular to it. Our first step is to determine the acceleration from the sum of forces and then determine velocity and height using numerical integration.

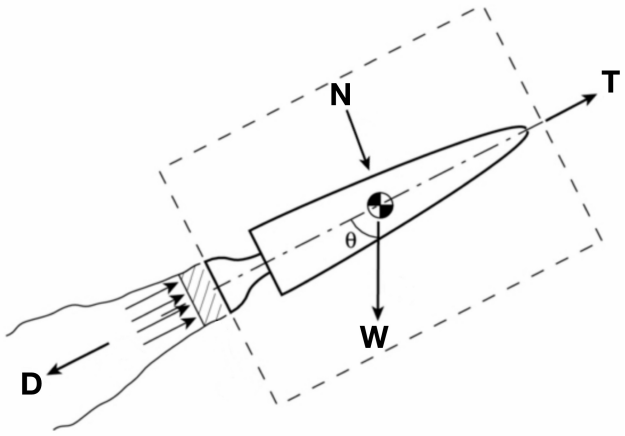

Figure 32: Free body-diagram of the rocket

To determine acceleration, Newton's second law, Equation 32, was applied shown in Equation 33. Note that the normal force acting on the rocket was neglected for this case as it does not change the apogee or flight path significantly.

$$\Sigma F = ma \tag{32}$$

$$\Sigma F_x = T - D - Mgcos(\theta) = Ma_x \tag{33}$$

To solve for velocity, Equation 33 was solved for a_x and integrated as shown in Equation 34.

$$u(t) = \int a dt \tag{34}$$

$$u(t) = \int \left(\frac{T(t) - D(t)}{M(t)} - g(t)\cos(\theta) \right) dt \tag{35}$$

$$h(t) = \int u_y(t) dt = \int u(t)\cos(\theta) dt \tag{36}$$

Equations 34 - 36 were then discretized and time stepped using Euler's method to obtain a numerical solution using MATLAB.

$$a_x(t + dt) = \left(\frac{T(t) - D(t) - M(t)g\cos(\theta)}{M(t)} \right) dt \tag{37}$$

$$u(t + dt) = u(t) + a(t)dt \tag{38}$$

$$h(t + dt) = h(t) + u_y(t)dt \tag{39}$$

Equations 37 - 39 were modified based on the trajectory stage of the rocket. The first stage is up to burnout and was determined based on the mass of the rocket. At burnout t = t_{burn}, the rocket mass $M(t_{burn}) = M_o - M_{prop}$ and thrust goes to zero. M_o is the initial mass of the rocket at launch. The second stage is after burnout but still climbing. The only forces acting on the rocket are gravity and drag and the stage ends when $u_y(t) = 0$. In the descend stage of the rocket, forces in the horizontal direction were neglected and in the absence of wind, it is assumed the rocket falls vertically after apogee since at this point our drouge parachute deploys.

Our attention is now turned to defining the variables in 37. Thrust as a function of time is defined as follows

$$T(t) = T_{jet} + (P_e - P_a(t))A_e \tag{40}$$

A pressure model taken from NASA Glenn was adopted to compute the atmospheric pressure (see Appendix C). Drag as a function of time can be calculated using Equation 41.

$$D(t) = \frac{1}{2}\rho(t)u(t)^2 S_{ref} C_D(t) \tag{41}$$

$$S_{ref} = \frac{\pi D^2}{4} \tag{42}$$

$$\dot{m}_{tot} = \frac{T(t)}{gI_{sp}} \tag{43}$$

$$M(t) = M_o - \dot{m}_{tot} dt \tag{44}$$

Other variables considered in the trajectory are the changes in atmospheric conditions due to altitude and decreasing gravitational effects. Using Equation 45 the change in air density were taken into account where $a = 1.2$ and $b = 2.9 * 10^5$.

$$\rho(t) = a \cdot exp(-bh(t)^{1.15}) \tag{45}$$

Utilizing Equation 46 gravitational forces were also considered with respect to altitude.

$$g = g_e \left(\frac{R_e}{R_e + h(t)} \right)^2 \tag{46}$$

Dynamic pressure was also calculated using Equation 47.

$$Q = \frac{1}{2}\rho u(t)^2 \tag{47}$$

A wind model was used to extrapolate the wind speed at a certain height using the Log Law, Equation 48, where V is the velocity at height Z. V_{ref} is the known velocity (15mph) at height Z_{ref} (15 ft). Z_0 is the roughness length in the current wind direction, for this case, Z_0 was chosen to be 0.0024 m [4].

$$V = V_{ref} \frac{ln(Z(t)/Z_0)}{ln(Z_{ref}/Z_0)} \tag{48}$$

Once the trajectory code was finalized, Figures 33 - 35 were printed to illustrate the overall trajectory of the rocket. Figure 33 displays the altitude reached by the rocket with respect to time. The motor burnout occurred at 7.79 seconds after which the rocket reached an apogee of 34,327 ft. Figures 34 and 35 illustrate the velocity and acceleration of the rocket respectively over time. It can be observed that the maximum velocity and acceleration occur at burnout. Main parachute deployment occurs at 3 minutes and 35 seconds and can be observed in Figure 33. This is closely followed by both the velocity and acceleration plots as velocity decreases and there is a spike in the acceleration at this time. Dynamic pressure was also plotted in Figure 36. It can be seen that both dynamic pressure and Mach number reached their maximum values at burnout. This is due to the short burn time of the motor such that the air density does not change

significantly with height during this stage. This makes velocity squared the dominating variable when computing Max-Q. Lastly, Figures 37 and 38 show the wind speed vs altitude and the rocket's horizontal velocity with time. Using the rocket's horizontal velocity, it was calculated the rocket will drift for 2.9 miles. These observations are summarized in Table 16.

Table 16: Trajectory main characteristics

Parameter	Result
Apogee	34327 ft
Maximum Velocity	1408.98 mph
Maximum Acceleration	89.16 ft/s^2
Mach Number	1.9
Maximum Dynamic Pressure	34.52 psi
Off Rail Speed	106.7 ft/s
Landing Velocity	45.18 ft/s
Drift	2.9 miles
Burnout Time	7.79 s
Static Margin Loaded	2.8177
Static Margin Empty	3.2386

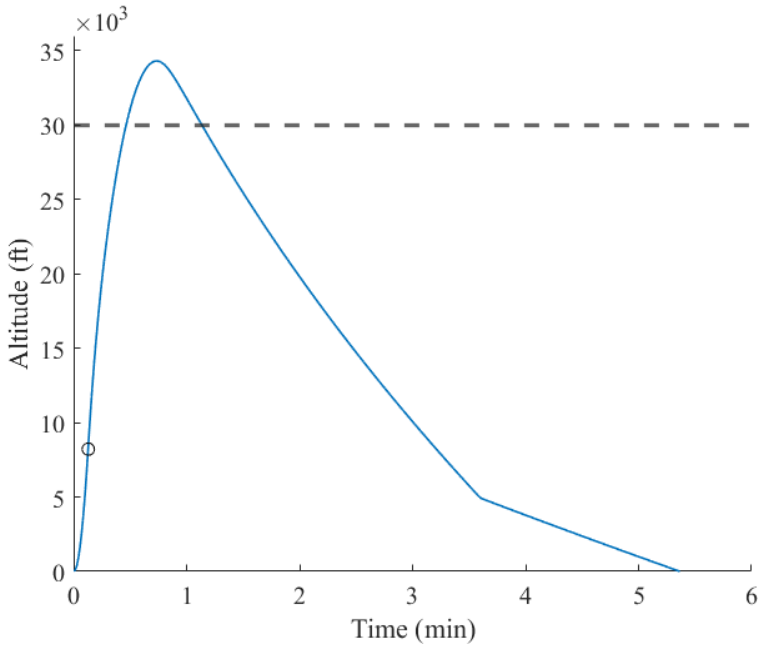

Figure 33: Altitude vs time plot

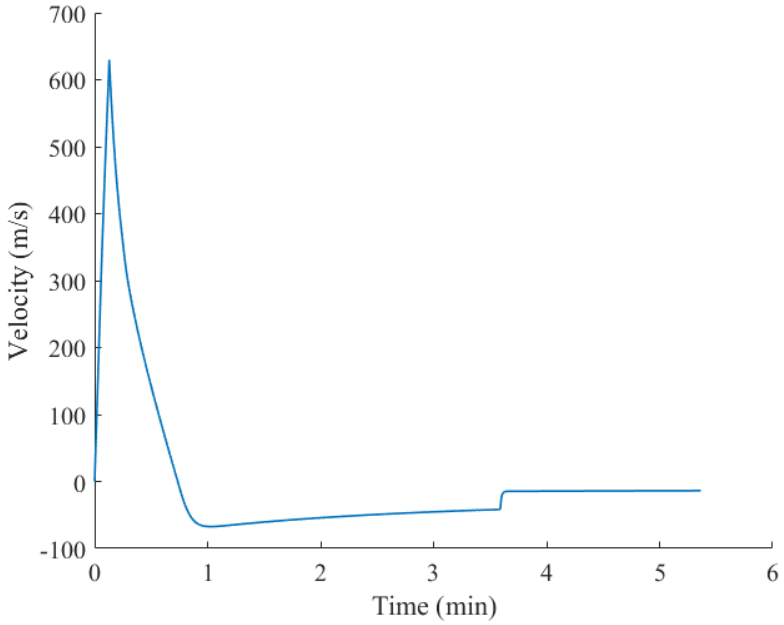

Figure 34: Velocity vs Time Plot

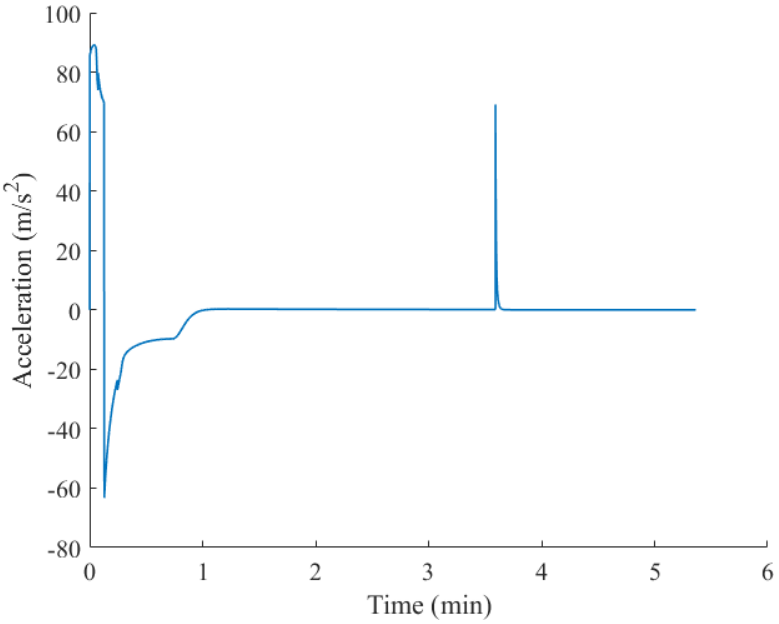

Figure 35: Acceleration vs time plot

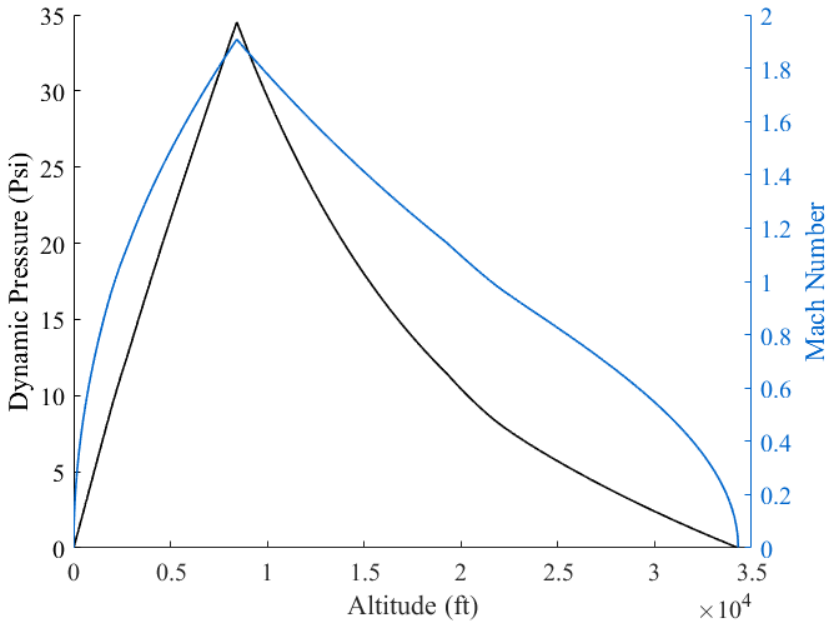

Figure 36: Dynamic pressure and mach number vs altitude plot

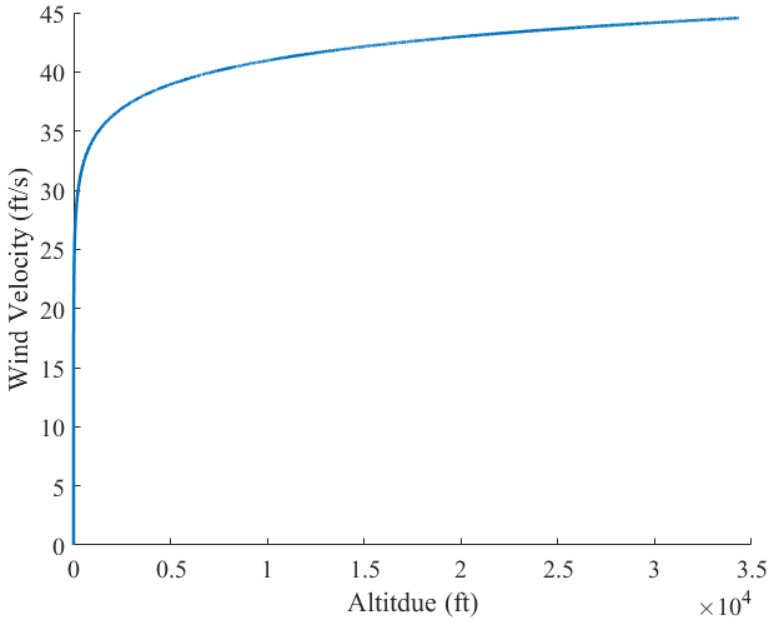

Figure 37: Wind velocity vs altitude plot

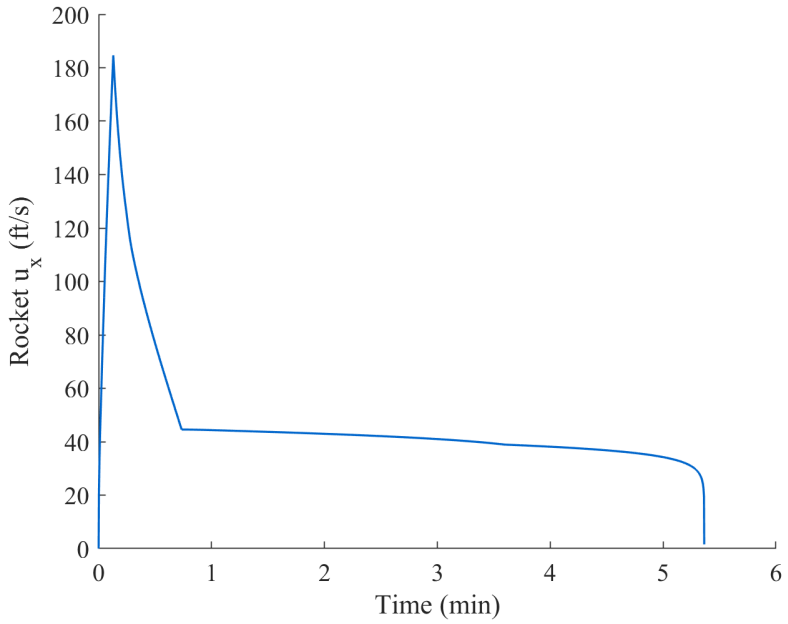

Figure 38: Rocket's horizontal velocity vs time plot

4.2 Drag Model

Drag is defined to be the aerodynamic force acting on the body as a result of contact between the solid body and its surrounding fluid. It is known that drag acts in the direction opposite to the thrust vector and can be expressed as a function of a non-dimensionalized drag coefficient, some geometric reference area, fluid density, and the velocity at which the body travels.

The drag forces acting on the rocket throughout its course of flight were approximated using an analytical model based on empirical data obtained from experiments performed on various existent rocket prototypes. The analytical model was extracted from data and equations delineated by "Drag Coefficient Prediction". The theoretical basis for a majority of the equations incorporated into this model is the United States Air Force Stability and Control Data Compendium, otherwise known as the USAF DATCOM. The application of this drag model was based on the assumption that induced drag can be neglected. The extent of drag effects accounted for by the model was limited to zero lift, or strictly parasite drag, implying the rocket was consistently clocked at a zero angle of attack.

While the rocket was expected to exhibit the largest fluctuations in its angle of attack immediately after ignition as the body leaves the launch rail, it was reasoned that the rocket would establish stability for the remainder of its flight. It was appropriate to assume that the angle of attack of the rocket for the majority of its flight trajectory would be low enough such that the zero-lift drag model could be used to approximate the total drag coefficient. Using this analytical model, one of the main contributors to parasite drag at subsonic speeds was identified to be skin friction drag resulting from the interactions of viscous forces along the surface of the rocket.

A drag force resulting from static pressure acting normal to the rocket surface known as pressure drag was examined in the forms of base drag and wave drag. It was expected that base drag, result of the blunt end of the rocket body, be the dominant contributor to total drag after burnout. Wave drag due to compression and shock waves, was determined to be significant as the rocket accelerates into the transonic and supersonic regimes. The fourth contributor to total drag was determined to be interference drag, a consequence of two bodies being fixed within close proximity to each other.

To calculate the total skin friction drag coefficient, kinematic viscosity change with altitude was taken into account as shown in Equation 49:

$$\nu = 0.000157 \cdot e^{az+b} \tag{49}$$

where a and b are constants dependent on the height of the rocket at the point of interest. The conditions for determining these constants are shown in Equations 50 - 52.

For the altitude condition of z $\leq$ 15,000 ft:

$$a = 0.00002503,\ b = 0 \tag{50}$$

For the altitude condition of 15,000 ft < z $\leq$ 30,000 ft:

$$a = 0.00002760,\ b = -0.03417 \tag{51}$$

For the altitude conditions of z > 30,000 ft:

$$a = 0.00004664,\ b = -0.6882 \tag{52}$$

It should be noted that the analytical drag model was originally derived in imperial units.

The total skin friction coefficient was defined to be a sum of the skin friction contributions from the rocket's body, fins, protuberances, excrescences, and the effects of their mutual interference. The mutual interference factor, K_F, was approximated by the model to be a constant for the fins and protuberances given in Equation 53.

$$K_F = 1.04 \tag{53}$$

The total skin friction coefficient can be expressed as follows in Equation 54.

$$C_{d,F} = C_{d,f}(body) + K_F C_{d,f}(fins) + K_F C_{d,pro} + C_{d,e} \tag{54}$$

It was determined that the design of the rocket would not require the need for launch lugs. It was also assumed that the rocket's surface was smooth without features of protuberances or excrescences. The skin friction drag of the rocket was strictly attributed to the viscous shearing forces experienced by the body and the fins. The rocket body skin friction coefficient was calculated as a function of its geometry and its interactions with the viscous forces of the fluid along the surface. To approximate the body skin friction coefficient,Equation 55 was utilized.

$$C_{d,f}(body) = C_f(final)\left[1 + \frac{60}{(L_R/D)^3} + 0.0025(L_R/D)\right]\frac{4S_B}{\pi D^2} \tag{55}$$

Similarly, the skin friction coefficient of the fins was calculated as a function of the fin geometry and its viscous shearing interactions along the surface as seen in Equation 56.

$$C_{d,f}(fins) = C_{f,\lambda}\left[1 + 60\left(\frac{t}{C_R}\right)^4 + 0.8(1 + 5X_{tc}^2)\left(\frac{t}{C_R}\right)\right]\frac{4NS_f}{\pi D^2} \tag{56}$$

The total wetted area of each fin, S_f, was determined using Equation 57.

$$S_f = \frac{S}{2}(C_R + C_T) \tag{57}$$

The fins were designed to be symmetrical using the NACA 0012 airfoil. The maximum thickness of each fin, t, and the location of maximum thickness as a percent of the chord, X_{tc}, were calculated as outlined in Equations 58 and 59.

$$t = 0.12 \cdot C_R \tag{58}$$

$$X_{tc} = 0.3 \tag{59}$$

The base drag coefficient of the rocket was determined differently depending on the Mach number, M, of the vehicle at the point of interest in its trajectory. It was noted that base drag tended to decrease as the rocket skin friction drag increased during the coast phase. The general equation for the base drag coefficient of a vehicle at subsonic speeds is related to the geometry of the rocket's body as well as its corresponding skin friction and interference effects as shown in Equation 60.

$$C_{d,B}(M \leq 0.6) = K_b\left(\frac{(D_b/D)^n}{\sqrt{C_{d,F}}}\right) \tag{60}$$

The constant of proportionality, K_b, and the exponent, n, were calculated according to the geometric configuration of the rocket using Equations 61 and 62.

$$K_b = 0.0274\tan^{-1}\left[\frac{L_b}{D} + 0.0116\right] \tag{61}$$

$$n = 3.6542\left(\frac{L_b}{D}\right)^{-0.2733} \tag{62}$$

The base drag coefficient of the vehicle at speeds above Mach 0.6 was approximated with the set of corresponding analytical equations expressed in Equation 63.

$$C_{d,B}(M > 0.6) = C_{d,B}(M \leq 0.6) \cdot f_b \tag{63}$$

The parameter f_b was derived from empirical data gathered from experiments conducted on various existent sounding rocket configurations. It is dependent on the Mach number associated with the vehicle at the point of interest along its trajectory. The conditions were defined by the model as such.

For a Mach number satisfying the conditional statement $0.6 \leq \mathrm{M} \leq 1$:

$$f_b = 1 + 215.8(M - 0.6)^6 \tag{64}$$

For a Mach number satisfying the conditional statement $1 < \mathrm{M} \leq 2$:

$$f_b = 2.0881(M-1)^3 - 3.7938(M-1)^2 + 1.4618(M-1) + 1.883917 \tag{65}$$

For a Mach number satisfying the conditional statement $\mathrm{M} > 2$:

$$f_b = 0.297(M-2)^3 - 0.7937(M-2)^2 + 0.1115(M-2) + 1.64006 \tag{66}$$

According to the drag model, contributions to wave drag under transonic and supersonic conditions were contingent on the length of the rocket and the Mach numbers defining the transonic regime. For this calculation, the transonic drag divergence Mach number M_D, and the final Mach number of transonic region, M_F, needed to be defined. The geometry of the rocket was evaluated by computing the length ratios of the nose cone to the rocket and the rocket to the body diameter, shown as constants in Equations 67 and 68 respectively.

$$\frac{L_N}{L_R} = 0.169 \tag{67}$$

$$\frac{L_R}{D} = 17.68 \tag{68}$$

The theoretical transonic Mach numbers M_D and M_F were subsequently evaluated by Equations 69 and 70.

$$M_D = -0.0156\left(\frac{L_R}{D}\right)^2 + 0.136\left(\frac{L_R}{D}\right) + 0.6817 \tag{69}$$

$$M_F = 2.4\left(\frac{L_R}{D}\right)^{-1.05} + 1.0275 \tag{70}$$

The maximum predicted rise in drag as the vehicle reaches transonic speeds was assessed as follows:

$$\Delta C_{D,max} = c\left(\frac{L_R}{D}\right)^g \tag{71}$$

where the coefficients c and g were determined by Equations 72 and 73.

$$c = 50.676\left(\frac{L_N}{L_R}\right)^2 - 51.734\left(\frac{L_N}{L_R}\right) + 15.642 \tag{72}$$

$$g = -2.2538\left(\frac{L_N}{L_R}\right)^2 + 1.3108\left(\frac{L_N}{L_R}\right) - 1.7344 \tag{73}$$

The final predicted transonic coefficient of drag rise for the vehicle at any given Mach number was calculated as function of the projected maximum rise in transonic drag. The relationship is expressed in Equation 74. It was noted that Equation 74 was only valid if the conditional statement $M_D \leq M \leq M_F$ was satisfied.

$$\Delta C_{d,T} = \Delta C_{D,max} \cdot F \tag{74}$$

Parameter F was determined as a function of transonic divergence Mach number M_D and final transonic Mach number M_F, shown in Equations 75 and 76.

$$x = \frac{(M - M_D)}{(M_F - M_D)} \tag{75}$$

$$F = -8.3474x^5 + 24.543x^4 - 24.946^3 + 8.6321x^2 + 1.1195x \tag{76}$$

When the vehicle has reached supersonic speeds, the supersonic wave drag coefficient can be simplified as follows:

$$\Delta C_{d,S} = \Delta C_{D,max} \tag{77}$$

if the conditional statement $M \geq M_F$ was true. The results of this approximation were known to have compared well and verified with test data.

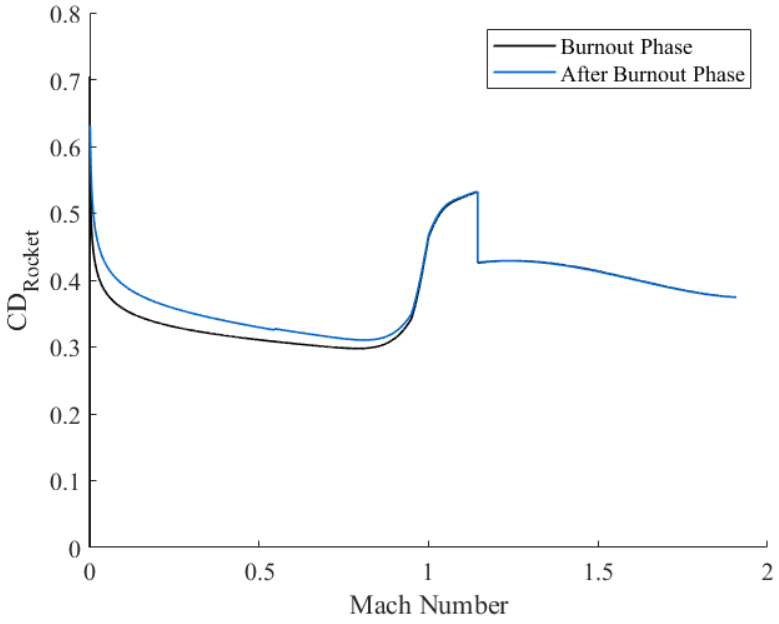

Figure 39: Drag coefficient of the rocket vs Mach number plot

The total drag coefficient computed for any Mach number associated with any point of interest along the trajectory of the rocket was evaluated as a sum of the component drag coefficients derived for skin friction drag, base drag, and wave drag. It was noted that the consideration of interference drag had been incorporated into the calculations of skin friction and base drag. The total drag coefficient equation can be expressed as Equation 78.

$$C_D = C_{d,F} + C_{d,B} + \Delta C_{d,T} + \Delta C_{d,S} \tag{78}$$

The total drag coefficient estimated using this model was plotted as a function of the Mach number. It was noticed that the model had initially underestimated the region of transonic increase at about $M = 0.8$, where it was expected to yield a drag coefficient between the values of 0.5 and 0.6. Reviewing the model, it was determined that the analytical method was derived from empirical data best fitted for rocket configurations with a nose cone to overall length ratio between 0.2 and 0.6. With a nose cone to rocket length ratio of 0.169, the drag predictions based on this model were expected to deviate slightly from the range of targeted prediction. To account for this slight deviation, it was deemed appropriate to establish a correction factor based on the target nose cone to rocket length ratio. The calculation of this scale factor and its application to obtain the corrected drag coefficient can be expressed as such in Equations 79 and 80, respectively. The corrected vehicle drag coefficient is plotted as a function of the Mach number in Figure 39.

$$SF = \frac{0.2}{(L_N/L_R)} \tag{79}$$

$$C_{D,corrected} = SF \cdot C_D \tag{80}$$

Displayed in Figure 39, as the Mach number approaches a near-zero value, it was noted that a sharp increase in the total drag coefficient would be observed due to the small magnitude of the associated Reynolds number. At extremely low Reynolds numbers, the flow was known to become turbulent and separate from the rocket surface, leading to this steep jump in the total drag coefficient. As expected, the transonic rise in drag predicted by the model was shown to increase the drag coefficient to a maximum value between the range of 0.5 and 0.6, near a Mach number of 0.8. Throughout this transonic phase of flight, wave drag was expected to dominate the contributions to the total drag acting on the vehicle. According to Figure 39, the vehicle drag coefficients after burnout were estimated to be slightly higher than those during burnout within the same range of Mach numbers. This difference was attributed to the increase in base drag as a result of the vehicle transition from non-zero to zero thrust flight. Thrust was known to have a nontrivial impact on drag experienced by vehicles with blunt aft bodies. Such was the phenomenon observed for the range of Mach numbers below 0.8.

While the corrected model demonstrated reasonable agreement with drag theory and experimental data collected for sounding rockets with similar geometric configurations, assumptions for zero lift were made to simplify the calculations carried out using the model. It was highlighted that in actual flight, the drag acting on the rocket was expected to be higher than the profile shown in Figure 39. The angles of attack experienced by the rocket after it has left the launch rail were expected to oscillate at angles low enough to be considered close to zero. In real flight, these angles are not expected to be exactly zero. The addition of induced drag contributions due to oscillations at non-zero angles of attack will need to be taken into consideration to simulate a more accurate drag profile. It was recognized that the limitations of this model would lead to discrepancies in the drag coefficients analyzed using CFD and in real flight tests.

4.3 Stability

An important parameter in determining a rockets stability is the center of pressure. This is the point at which the surface integral of the pressure field over the entire body of the rocket effectively acts at as a single force. In order to obtain a stable configuration, the center of pressure should be located aft of the center of gravity. To calculate the center of pressure, the Barrowman's Equations were utilized [6]. Figure 40 displays relevant physical dimensions of the rocket used to estimate the center of pressure.

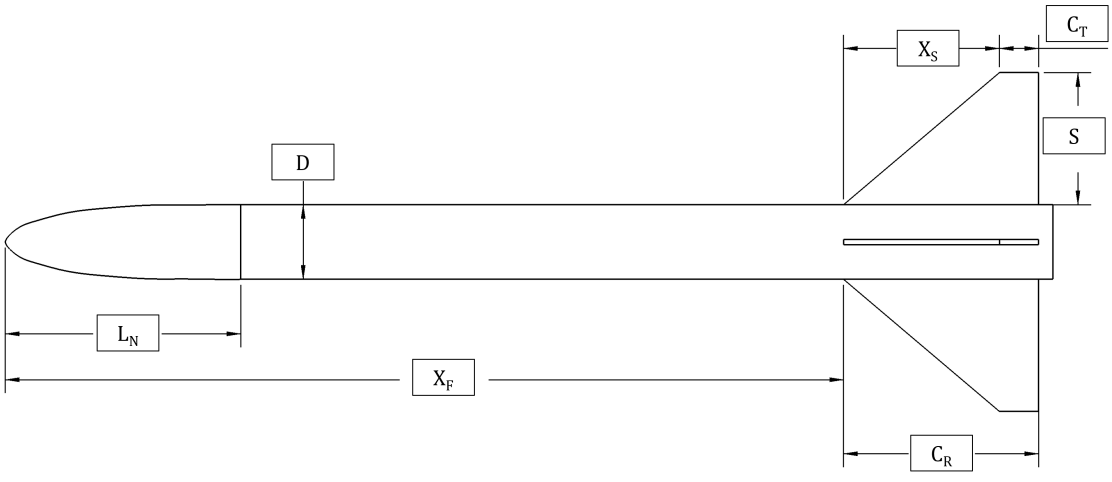

Figure 40: Relevant dimensions for stability analysis

D: Diameter at base of nosecone
L_N: Length of nosecone
X_F: Distance from nose tip to fin root-chord leading edge
C_R: Fin root-chord
C_T: Fin tip-chord
L_F: Span length at chord of fins
X_S: Distance between fin root leading edge and fin tip leading edge parallel to body
S: Fin semi-span
N: Total number of fins

The nosecone was analyzed first. The normal force coefficient used for the nosecone is shown in Equation 81 taken from lab 2.

$$C_{N\alpha,n} = 2.0 \tag{81}$$

The center of pressure for the nosecone was calculated using Equation 82. Since an elliptical nose was used, α is equal to 0.333.

$$X_N = \alpha \cdot L_N \tag{82}$$

Once the center of pressure of the nosecone was obtained, we found the fin and body interference factor using Equation 83.

$$K_{fb} = 1 + \frac{D}{2S + D} \tag{83}$$

To obtain the span length at the chord of the fins, Equation 84 was used.

$$L_F = \sqrt{S^2 + \left(X_S + \frac{C_T - C_R}{2}\right)^2} \tag{84}$$

Once the length at the chord of the fins was obtained, it was used to calculate the normal force coefficient on the fins as shown in Equation 85 where β is determined by the number of fins on the rocket. Since the rocket was designed with four fins, the value of β is equal to 16.

$$C_{N\alpha,f} = \frac{\beta \left(S/D\right)^2}{1 + \sqrt{1 + \left(2L_F/(C_R + C_T)\right)^2}} \tag{85}$$

To calculate the normal force on the fins in presence of the body, the normal force coefficient on the fins was multiplied by the interference factor as shown on Equation 86.

$$C_{N\alpha,fb} = K_{fb} \cdot C_{N\alpha,f} \tag{86}$$

The center of pressure of the fins was calculated using Equation 87.

$$X_f = X_F + \frac{X_S(C_R + 2C_T)}{3(C_R + C_T)} + \frac{1}{6}\left(C_R + C_T - \frac{C_R \cdot C_T}{C_R + C_T}\right) \tag{87}$$

At large angles of attack the the normal force coefficient on the body becomes relevant and was calculated using Equation 88 where α is the angle of attack.

$$C_{N\alpha,body} = \frac{4}{\pi}\frac{L_{body}}{D}\alpha \tag{88}$$

Once the normal force coefficient of the body was obtained, the center of pressure for the body of the rocket was computed using Equation 89.

$$X_{body} = L_N + \frac{L_{body}}{2} \tag{89}$$

The total normal force coefficient on the rocket was then computed using Equation 90. Upon determining the total normal force coefficient, the total normal force of the rocket was calculated using Equation 96.

$$C_{N,T} = C_{N\alpha,n} + C_{N\alpha,fb} + C_{N\alpha,body} \tag{90}$$

After all parameters were gathered, the center of pressure of the entire rocket was obtained using Equation 91

$$X_{CP} = \frac{C_{N\alpha,n}X_n + C_{N\alpha,fb}X_f + C_{N\alpha,body}X_{body}}{C_{N\alpha,T}} \tag{91}$$

In order to find the center of gravity of the entire rocket, moments were taken about the tip of the nosecone for every component and divided it by the total mass as shown in Equation 92.

$$X_{CG} = \frac{\Sigma Moments}{\Sigma Mass} \tag{92}$$

Ultimately we were able to calculate the static margin of the rocket using Equation 93.

$$SM = \frac{X_{cp} - X_{cg}}{D} \tag{93}$$

Once the static margin was computed, fins were designed to stabilize the rocket's flight and achieve the static margin desired. It was also desirable to have symmetrical shape for the fins to avoid producing a net lift force in any direction and to avoid excess drag. As a result, a NACA 0012 airfoil was used. Table 17 displays the final fin parameters and Table 18 displays loadings at maximum dynamic pressure.

Table 17: Fin dimensions for the rocket

Number of fins	C_R	X_S	S	C_T	Thickness
4	7 in	4 in	7 in	3 in	0.84 in

Table 18: Loadings at Max Q

Component	Coefficient	Value	Normal Force (kN)
Fin	$C_{N\alpha,fb}$	3.4924	0.71
Body	$C_{N\alpha,body}$	1.2950	5.26
Nosecone	$C_{N\alpha,n}$	2.0	8.12
Rocket	$C_{N\alpha,T}$	6.7875	27.55

4.4 Dynamic Stability

In determining the pitch angle and dynamic stability, a similar approach was taken as for static stability. For dynamic stability analysis a third equation is introduced. Looking at the free body-diagram, Figure 32, Newton's second law was applied but this time the normal force acting on the rocket was considered as well as the moment it causes. For this case, the x-axis and y-axis are horizontal and vertical respectively.

$$F_x = N\cos(\theta) + (T - D)\sin(\theta) = ma_x \tag{94}$$

$$F_y = -N\sin(\theta) - W + (T - D)\cos(\theta) = ma_y \tag{95}$$

The normal force is a function of time and was calculated using Equation 96. It is coupled with equations 94 and 95 because it depends on velocity and velocity is determined from the accelerations.

$$N(t) = \frac{1}{2}\rho u(t)^2 C_{N\alpha,T}\alpha S_{ref} \tag{96}$$

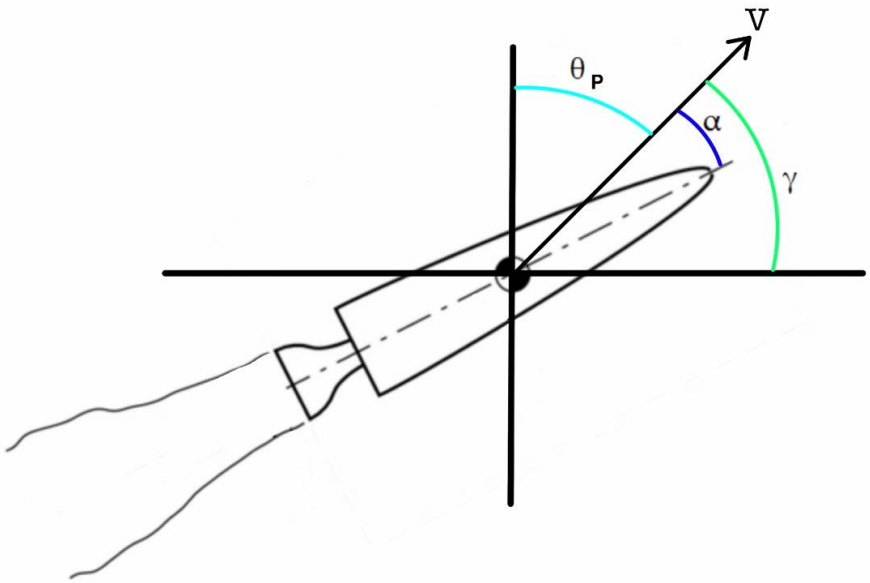

Figure 41: Relevant angles

From Figure 41, the pitch angle θ_p is found by double integrating the angular acceleration as shown in Equation 97.

$$\theta_P = \int \left(\int \ddot{\theta}_P(t)dt \right) dt \tag{97}$$

The flight path angle γ is the angle between the horizontal and the rocket's velocity vector shown in Figure 41. γ is determined by taking the inverse tangent of the ratio of the rocket's velocity components, shown in Equation 98.

$$\gamma = \tan^{-1}\left(\frac{u_y}{u_x}\right) \tag{98}$$

The angle of attack was obtained by subtracting 90° from the sum of the pitch angle and the flight path angle as shown in Equation 99.

$$\alpha = \theta_P + \gamma - 90 \tag{99}$$

In order to obtain the pitch angle, the angular acceleration, represented by α, was first computed using Equation 100. The sum of moments was taken at the center of gravity and the only force causing a moment is the normal force. The distance between the normal force and the CoG can be determined from the static margin shown in Equation 101. The mass moments of inertia was taken to be the average of when the rocket is emptied and loaded.

$$\Sigma M = I\alpha = I\dot{w} = I\ddot{\theta} \tag{100}$$

$$\Sigma M_{CoG} = N(SM \cdot D) \tag{101}$$

$$\ddot{\theta} = \frac{N(t)(SM \cdot D)}{I_{avg}} \tag{102}$$

Equation 102 was then discretized and time stepped using Euler's method to obtain a numerical solution using MATLAB.

$$w(t+dt) = w(t) + \ddot{\theta}_P(t)dt \tag{103}$$

$$\theta_P(t+dt) = \theta_P + w(t+dt)dt \tag{104}$$

After the pitch angle was calculated, it was plotted using MATLAB. See Figure 42 for finals results. As seem from Figure 42, the rocket experienced a 13.5° overshoot and had a settling time of about 20 seconds.

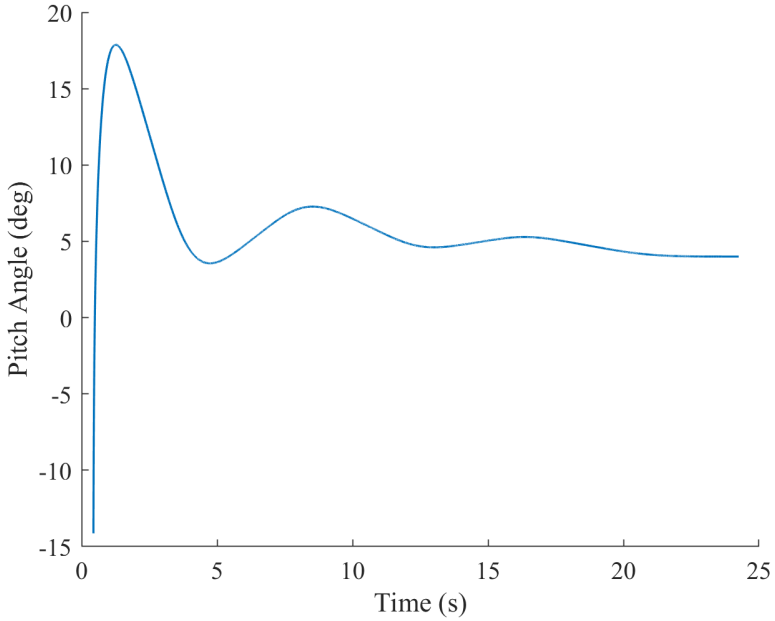

Figure 42: Dynamic stability: pitch angle vs time plot

4.5 Recovery

The main goal of the recovery system is to safely recover the rocket and payload utilizing a dual-deployment parachute system. The dual-deployment system is based on Hagstrom et al. "Project Prometheues at UCLA" and consists of a drogue parachute which is released at apogee and a main parachute which is released at 5000 ft above the ground.

When selecting the size of the parachutes, student team rockets of similar size were examined to determine the initial guess of both parachutes. Once the initial guess was obtained, the diameter of the main parachute was varied until the desired landing velocity was obtained. The main parachute was taken from Rocketman parachute website and the drogue was taken from Fruity Chutes website [8] [9]. Table 19 displays physical parameters for both parachutes.

Table 19: Parachutes Physical Properties

	Area (m^2)	Cd	Weight (kg)
Drogue	0.289	1.5	0.062
Main	3.56	0.97	0.23

In order to execute a successful recovery, two altimeters are used and programmed to deploy the drogue parachute at apogee and the main parachute at 5000 ft. These altimeters are connected to a perfboard which is then connect to two batteries as illustrated in Figure 43. The recovery deployment method and the lengths of the shock chords are based on "Project Prometheues at UCLA" [7]. The recovery system then is placed inside the avionics section shown in Figure 2. To execute this method, two Peregrine ejection systems release 24 grams of CO_2 to deploy the drogue parachute and 51.8 grams of black powder are used to release the main the parachute. The amount of CO_2 and black powder was determined using an online calculator. Figure 44 displays the overall size of both the parachutes and the shock chord lengths.

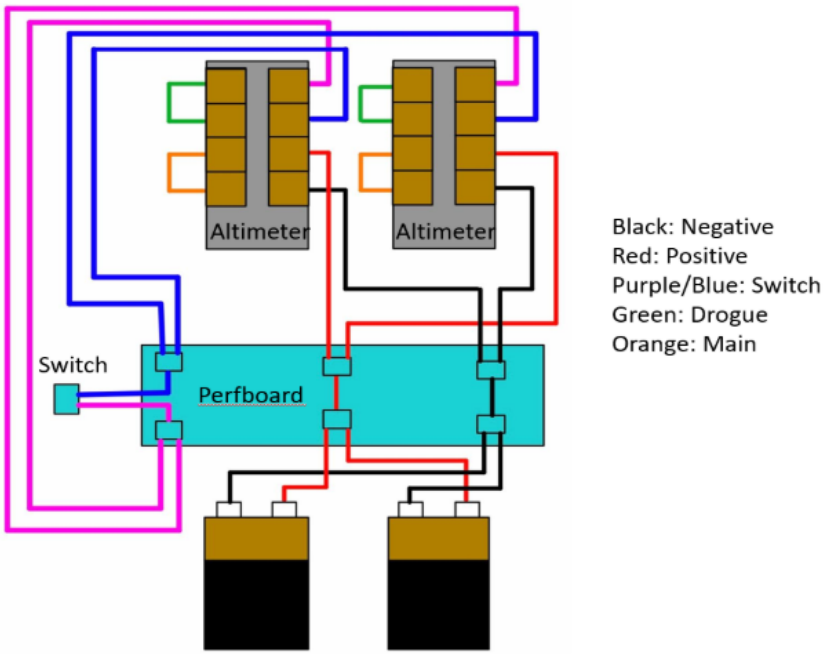

Figure 43: Recovery system diagram

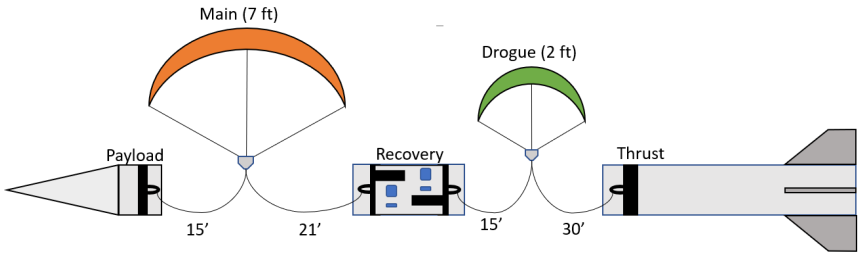

Figure 44: Parachute sizing diagram

Both parachute are carefully folded and placed inside the rocket following standard procedures as instructed in the Fruity Chutes website. Once the rocket is lunched, the recovery system will release the drogue parachute upon reaching apogee as illustrated in Figure 45. The main purpose of the drogue parachute is to slow down the rocket to a velocity of 137.1 ft/s.

The drogue parachute enables the main parachute to successfully deploy without failing at a height of 5000 ft as shown in Figure 46. The height of deployment for the main parachute was chosen arbitrary to

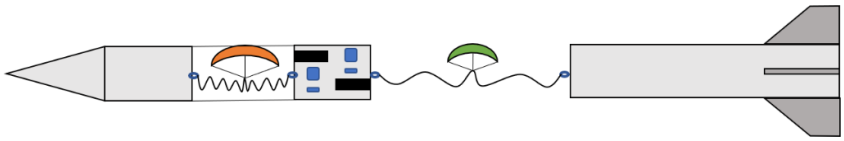

Figure 45: Drogue parachute deployment

minimize drift. Once the main parachute is deployed, it will slow down the rocket to a velocity of 45.81 ft/s with a drift of 2.9 miles. Table 20 summarizes the recovery parachute deployment.

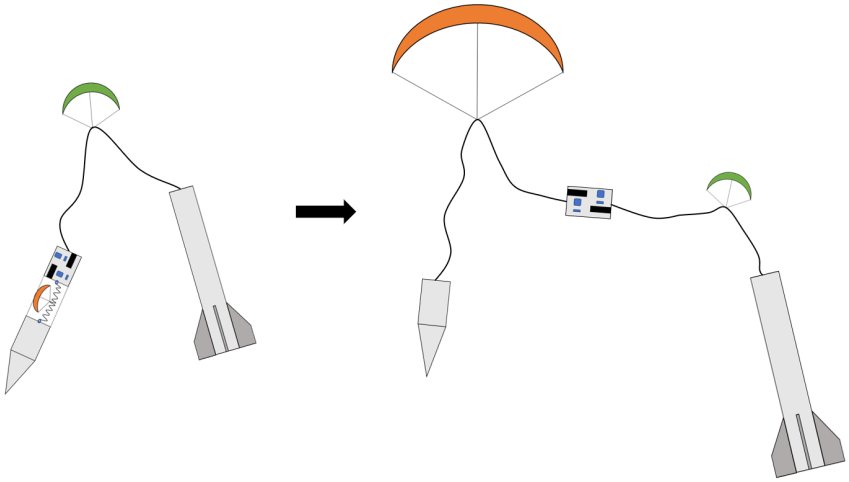

Figure 46: Main parachute deployment

Table 20: Parchute's deployment summary

	Deployment height	Slow Down Velocity (ft/s)
Drogue Parachute	Apogee	137.1
Main Parachute	5000 ft	45.81

5 Structural Analysis

5.1 Material Selection

The material selection process was done using a series of trade studies for the major components in the rocket. Below outlines such studies and their results.

5.1.1 Nosecone

An RF transparent material easily molded into the desired shape, a fiberglass-epoxy composite was chosen for the nosecone material. Structural analysis was not considered as no significant loading conditions were expected on the nosecone in comparison to the material strength.

5.1.2 Bulkheads

Aluminum 6061-T6 was chosen as the material for all bulkheads. Possible materials examined were laminate plywood and Al 6061-T6. Initial mass and dimension calculations were performed assuming a uniform flat plate geometry. The boundary and loading conditions assessed are shown visually in Figure 47 and 48. The center load was assumed over a radius of 1.125". Loading was applied as a maximum instantaneous force of 2000 lbf in addition to the force applied to the appropriate bulkhead from supporting the mass above it at Max Q. The edge conditions were modelled as clamped for epoxied bulkheads and simply supported for bolted bulkheads. Avionics and pressure recovery bulkhead analysis was calculated with center loading conditions and clamped edge conditions. All other bulkheads were modelled with uniform loading with simply supported edge conditions. The initial analysis showed plywood as the preferred material due to thickness requirements influenced by bearing and shear tear-out. Upon further bulkhead geometric optimization aluminum was shown as the lighter and stronger material option for all bulkheads.

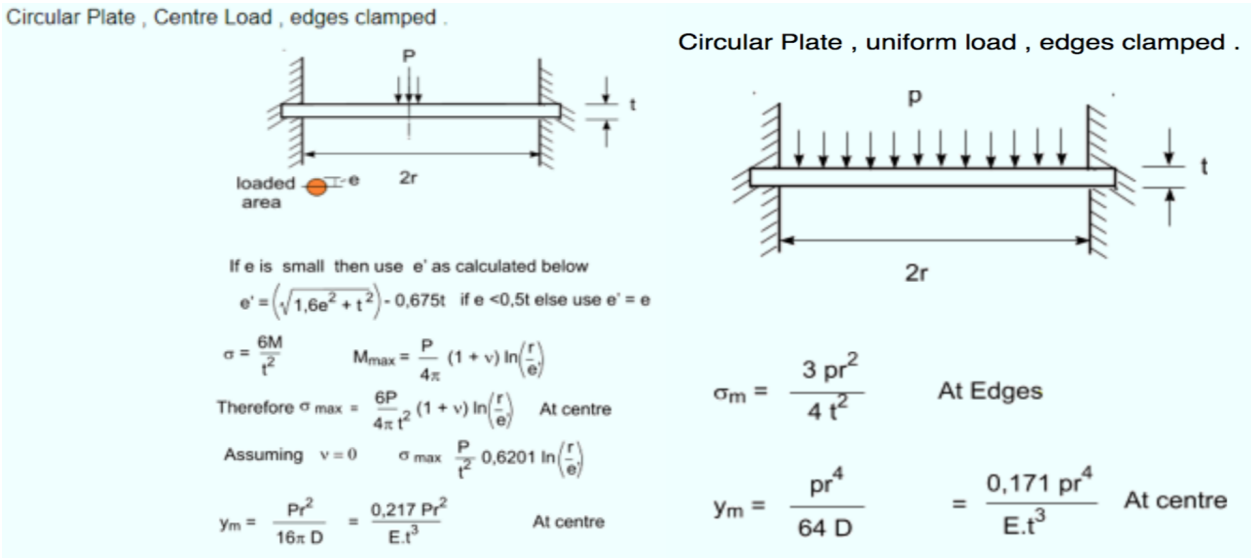

Figure 47: Boundary and Loading Conditions of Bulkhead Analysis

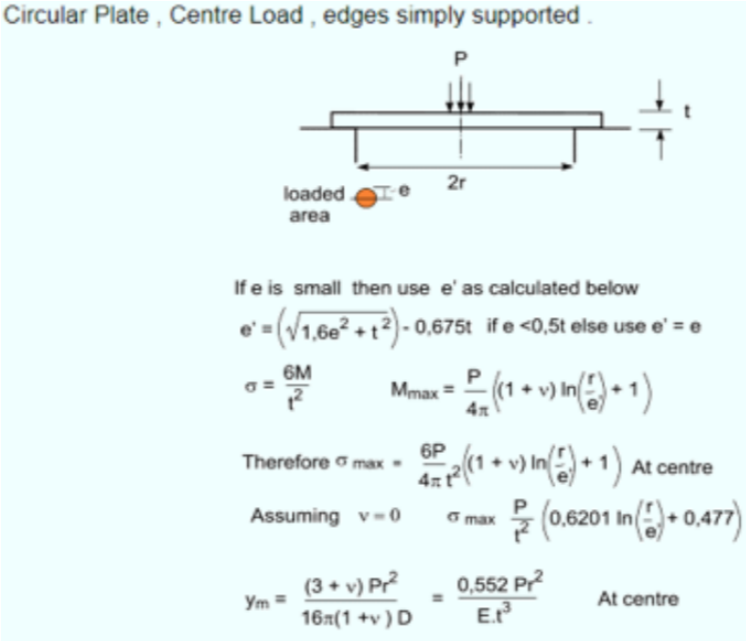

Figure 48: Boundary and Loading Conditions of Bulkhead Analysis

5.1.3 Body Tubes & Couplers

Unidirectional prepreg carbon fiber was chosen as the body tube and coupler build material. An initial trade study was done comparing euler buckling of unidirectional carbon fiber and rolled Al 6061-T6; results showed the thickness required for either material was too small to be of any practical use. Further shear tear out analysis was performed and showed the ideal material was unidirectional carbon fiber with 3 layers (0.045" thick). Euler buckling and shear tear-out are both illustrated in Figure 49 This analysis was done using max strain theory in tension for buckling in a max loading case of 2000 lbf and shear tear-out with #10 SS 5/16" screws.

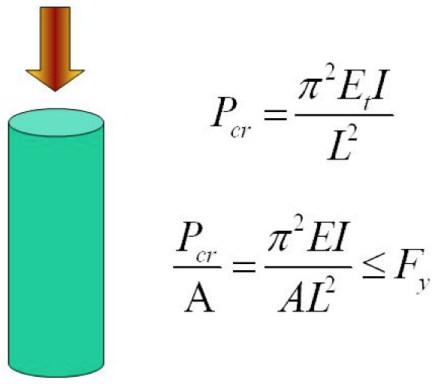

Figure 49: Euler Buckling of Body Tubes

5.1.4 Tank Skirts

Tank skirt materials were chosen to accommodate the manufacturing techniques required for assembly. The welded portion of the tank skirts must match the material of the component being welded onto. The Al 6061-

T6 oxidizer tank and pressurant tank skirts material were therefore Al 6061-T6. The mild steel combustion chamber tank skirt was mild steel. Having the best strength to weight ratio of possible materials, the 4 tank skirt connecting shells were assigned Al 6061-T6.

5.1.5 Pressurant Tank

Al 6061-T6 was chosen as the pressurant tank build material as the cost of a commercial fiberglass tank was significantly higher than that of welded aluminum. It was also difficult to find a commercial tank of the size and rating required. Using FEA the chosen aluminum tank design proved to have a FOS higher than 1.5 under maximum loading conditions while staying within maximum mass and size requirements.

5.1.6 Oxidizer Tank

Al 6061-T6 was chosen as the oxidizer tank build material as it was light and reasonably thick for the MEOP. Using FEA the chosen aluminum tank design proved to have a FOS higher than 1.5 under maximum loading conditions while staying within maximum mass and size requirements.

5.1.7 Injector

Resistant to thermal contraction and with an increasing tensile strength at low temperatures, 304 stainless steel was chosen for the injector build material. The injector was to be subjected to intense temperature gradients as the oxidizer was cryogenic and its proximity to the combustion chamber. Stainless steel provided properties fit to resist warping in these extreme conditions.

5.1.8 Combustion Chamber

With high temperature threshold, mild steel was chosen as the material for the combustion chamber. This material choice removed the possible need for extraneous cooling methods. Note that unburned fuel also acts as an ablative, lessening the temperature requirements on the material.

5.1.9 Fasteners Hardware

Screws

Screws for all bulkheads were chosen to be # 10 SS 5/16". This was possible as all bulkhead designs had the same edge geometry that accommodated the shear tear-out, bearing failure, and bolt shear of this size fastener. This fastener diameter balanced the strength of the fastener itself in bolt shear and the edge thickness for shear tear-out of the bulkhead (directly translating into the mass of the bulkheads). The length of the screw was based on the minimum thread engagement length multiplied by a FOS of 1.5. Equations 105, 106, and 107 show the bearing failure, shear tear-out, and bolt shear equations used. Here P_{max} is the maximum allowable applied load, τ_{allow} is the shear strength of the material multiplied by a FOS of 1.5, e is the distance from the edge of the fastener to the material edge, t is the material thickness, σ_B is the bearing strength of the material, and A is the cross sectional area of the fastener. Figure 50 provides a visual representation of these relations. Four fasteners were chosen at 90 degree angles on the bulkheads: 3 to create a stable plane, and a fourth for redundancy.

$$P_{allow} = \sigma_B \cdot A \tag{105}$$

$$P_{allow} = 2\tau_{allow} \cdot e \cdot t \tag{106}$$

$$P_{max} = \tau_{allow} \cdot A \tag{107}$$

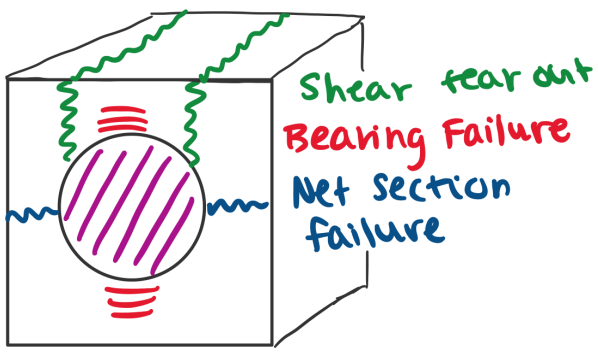

Figure 50: Fastener Failure Modes

Shear Pins U-Bolt

Recovery hardware analysis was done in two parts. Shear pins were sized according to accommodate the expected bay pressurization pressure at deployment. This was approximately 1300 lbf (including a FOS of 1.5). Bolt shear analysis was used to calculate the number and size of shear pins needed. The shear strength of the shear pin material and the load applied by deployment CO2 was used to solve for the cross sectional area required of the screw in Equation 107. This led to selecting 4 8/32 Nylon 6/6 shear pins.

The recovery U-Bolt was simply sized according to the maximum load felt by the rocket at main deploy, which is calculated in the Structural Analysis section. The U-Bolt selected was rated to 2400 lbf with a manufacturer's FOS of 2.

5.2 Structural Components

5.2.1 Maximum Loading Condition: Max Q

The loading condition on the rocket during Max Q (or max dynamic pressure) was calculated using values collected from the trajectory code and from simple extrapolation of the given information (ex. AOA for 50 ft/s horizontal gust), shown below in Table 21.

Table 21: Rocket Properties at Max Q

Property	Value
Acceleration	88.38 m/s^2
Velocity	734.04 m/s
AOA	2.38 °
Drag at Nosecone Tip	398.55 N
Normal Force on Fins	310.34 N
Normal Force on Body	1840.60 N
Location of CP (from nosecone)	2.58 m
Location of CG (from nosecone)	1.99 m
Horizontal Wind Velocity	15.24 m/s

To complete the analysis each load transferring component had its upstream mass calculated. This was added to the drag force felt by the rocket to produce a maximum axial force felt by the component. To compute bending moments the distance of each component from the Cp was also calculated and recorded.

These masses and distances are shown in Table 22.

Table 22: Component Properties at Max Q

Property	Upstream Mass (kg)	Distance to Cp (m)
Main/PL	9.80	1.97
AV 2	10.20	1.70
AV 1	11.90	1.57
Drogue/Press Upper	40.20	1.36
Press Lower	0.91	1.08
Thrust	35.20	0.98
Ox Tank	158.78	0.97
CC	123.58	0.64
Fins	0	0.72

These values were then converted into axial and bending loads using Newton's Second Law. Specifically, axial forces were calculated using Equation 108, bending forces using Equation 109, and shear forces using Equation 110. Where Mu is the mass upstream of the component, D is the drag force at Max Q, N is the normal force on the component (shear), XPG is the distance to the Cp from the component's CoG, I is the mass moment of inertia, a_{lat} is the axial acceleration of the rocket at Max Q and a_{ang} is the angular acceleration. A visual representation of these loading conditions is seen in Figure 51 and Figure 52.

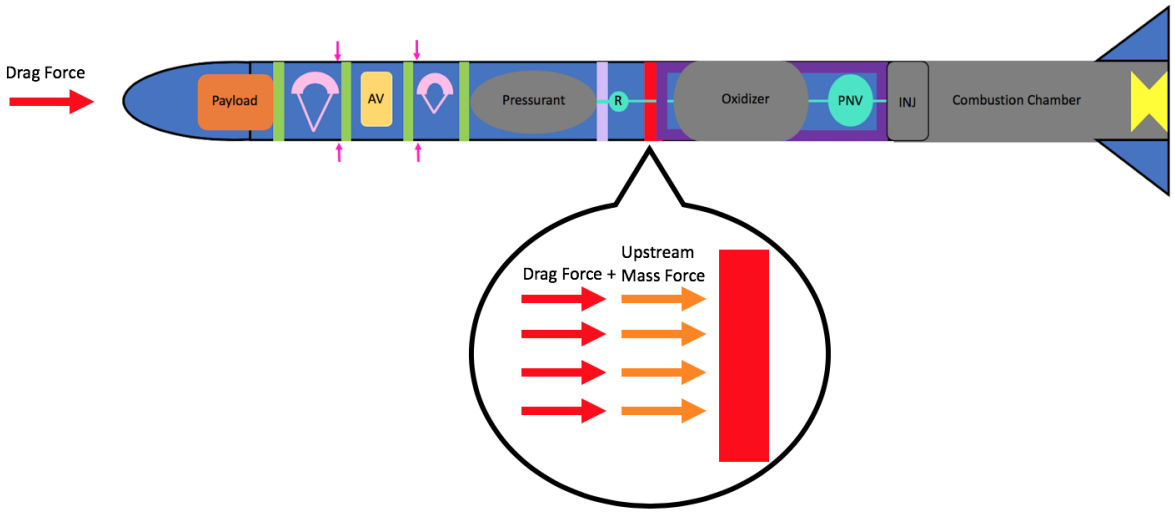

Figure 51: Axial Loading at Max Q

$$F = Mu \cdot a_{lat} + D \tag{108}$$

$$M = N \cdot XPG + I \cdot a_{ang} \tag{109}$$

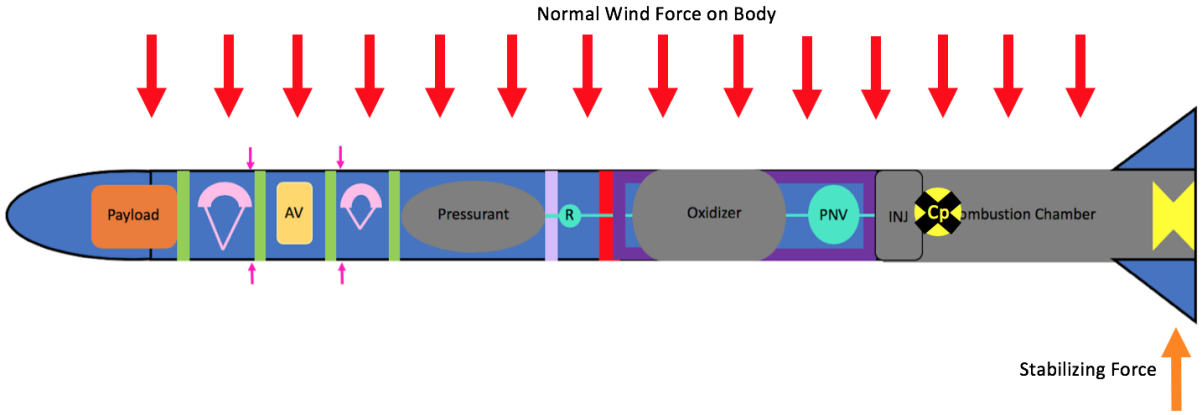

Figure 52: Bending Loads at Max Q

$$F_S = Mu(a_{lat} - a_{ang}) \tag{110}$$

The resulting forces acting on the rocket were as expected. Full plots of the axial, bending, and shear results are shown below in Figure 53, Figure 54, and Figure 55 respectively. A maximum axial force of 9881.23 N occurred at the tank/combustion chamber, which follows as the drag force is constant across the rocket but the tank/combustion chamber had the largest upstream mass. The maximum moment of 3623.41 Nm occurred at the main parachute/payload bulkhead, which follows the observation that the payload bulkhead is the structural component furthest from the Cp, resulting in a larger moment. The shear diagram showed a constant shear for the entire body as it was assumed that the wind gust normal force was uniformly distributed across the body. The sharp spike in shear of 11977.64 N at the fins resulted from the fin's reactant force on the rocket.

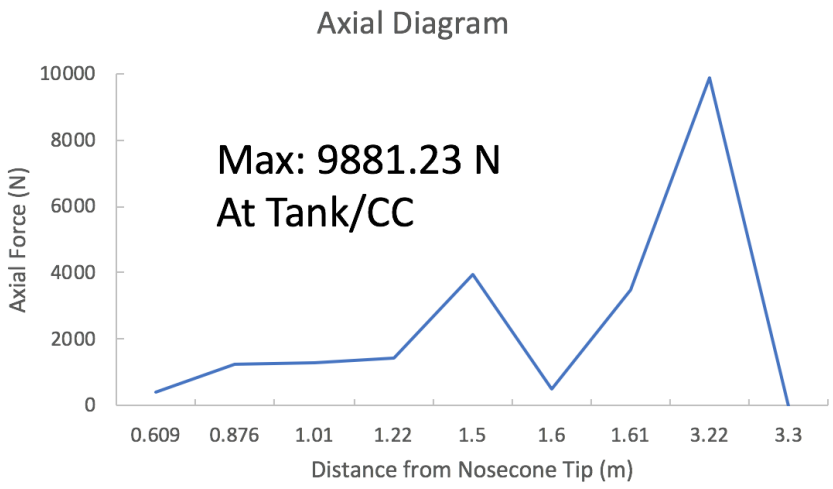

Figure 53: Max Q Axial Forces

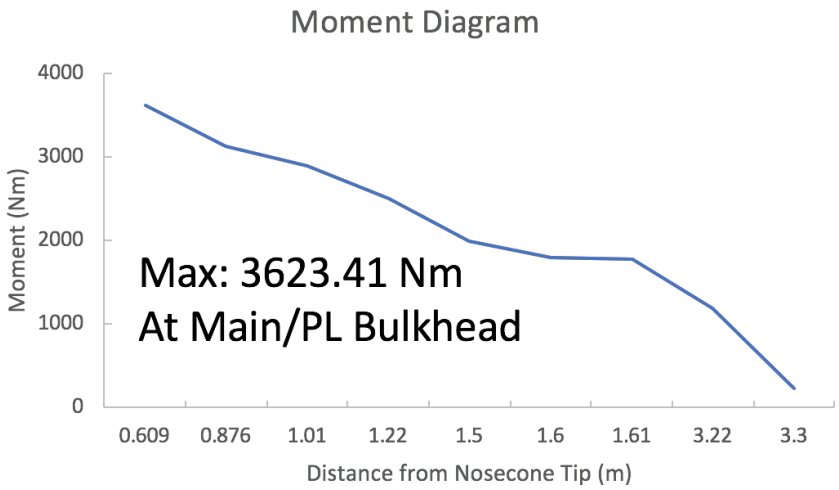

Figure 54: Max Q Bending Forces

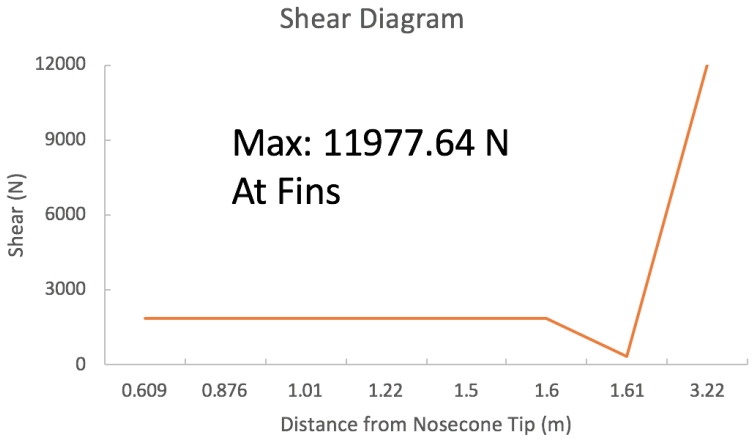

Figure 55: Max Q Shear Forces

5.2.2 Maximum Loading Condition: Drogue Deploy

The loading condition on the rocket during drogue deployment was calculated using values collected from the trajectory code and from simple extrapolation of the given information shown below in Table 23. It was assumed the parachute deployed at a 90 degree angle to the rocket's body.

To complete the analysis each load transferring component had its upstream mass calculated. To compute bending moments the distance of each component from the Cp was also calculated and recorded. These masses and distances are shown in Table 24.

These values were then converted into axial and bending loads using Newton's Second Law. Specifically, axial forces were calculated using Equation 111, bending forces using Equation 109, and shear forces using Equation 110, but neglecting drag force. A visual representation of these loading conditions is seen in Figure 56.

Table 23: Rocket Properties at Drogue Deploy

Property	Value
Acceleration	9.81 m/s^2
Velocity	23.61 m/s
AOA	0.00 °
Drag at Nosecone Tip	37.82 N
Normal Force on Body	3.49 N
Loaction of CP (from nosecone)	2.6373 m
Location of CG (from nosecone)	1.9905 m
Horizontal Wind Velocity	0.00 m/s

Table 24: Component Properties at Drogue Deploy

Property	Upstream Mass (kg)	Distance to Cp (m)
Main/PL	9.80	1.97
AV 2	45.01	1.70
AV 1	80.21	1.57
Drogue/Press Upper	35.20	1.36
Press Lower	0.91	1.08
Thrust	40.20	0.98
Ox Tank	11.90	0.97
CC	10.20	0.64
Fins	0.00	0.72

$$F = Mu \cdot a_{lat} \tag{111}$$

The resulting forces acting on the rocket were as expected. Full plots of the axial, bending, and shear results are shown below in Figures 57, Figure 58, and Figure 59 respectively. A maximum axial force of 2533.24 N occurred at the Tank/CC, which follows as the tank/combustion chamber had the largest upstream mass (itself). We see another spike at the second avionics bulkhead, which tracks with the location of the break in the rocket after drogue deploy. The maximum moment of 2602.40 Nm occurred at the main tank/combustion chamber, which follows the observation that the tank/combustion chamber is the structural component furthest from the Cp after deployment, resulting in a larger moment. The shear diagram showed a constant shear for the entire body as it was assumed that the normal force calculated in the trajectory code was uniformly distributed across the body. The sharp spike in shear of 25.44 N at the fins resulted from the fin's reactant force on the rocket.

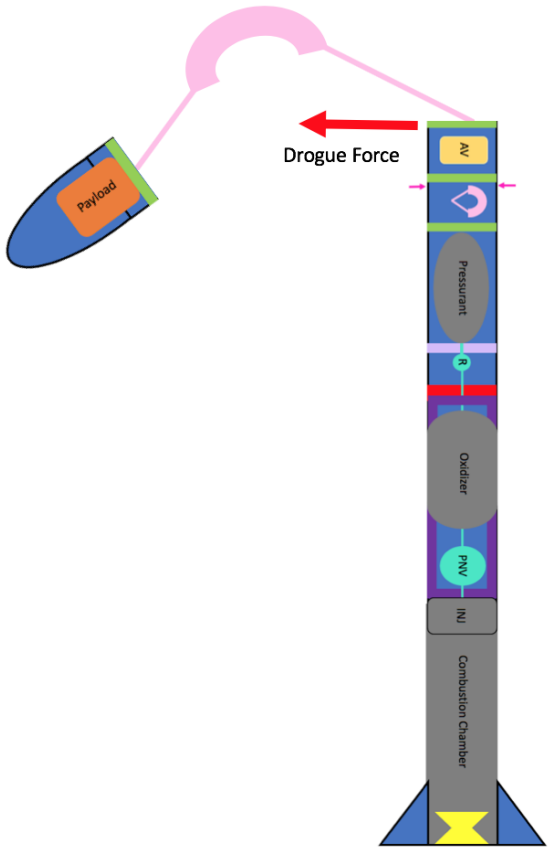

Figure 56: Loading at Drogue Deploy

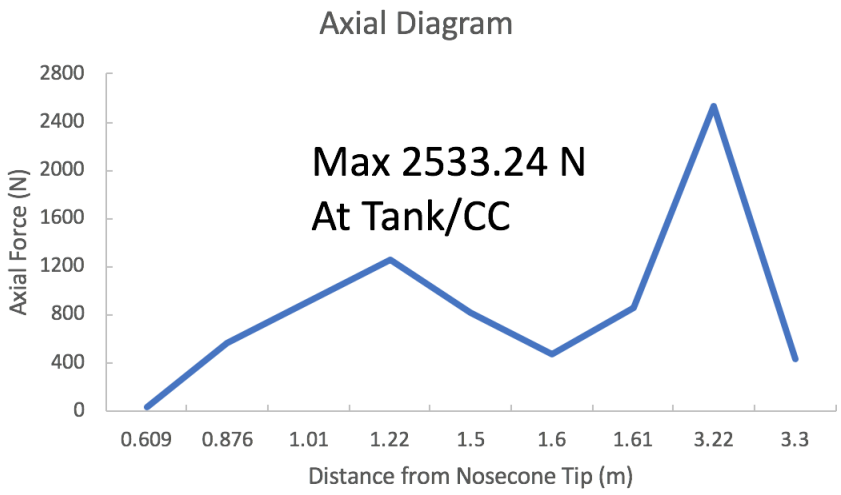

Figure 57: Drogue Axial Forces

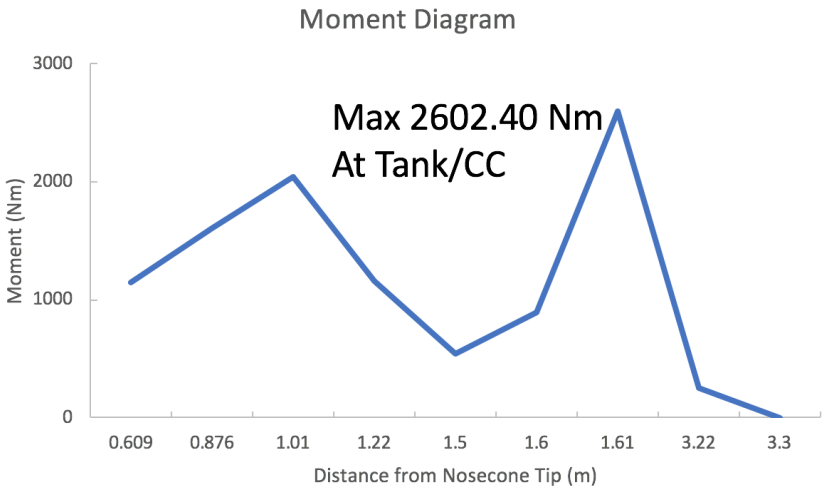

Figure 58: Drogue Bending Forces

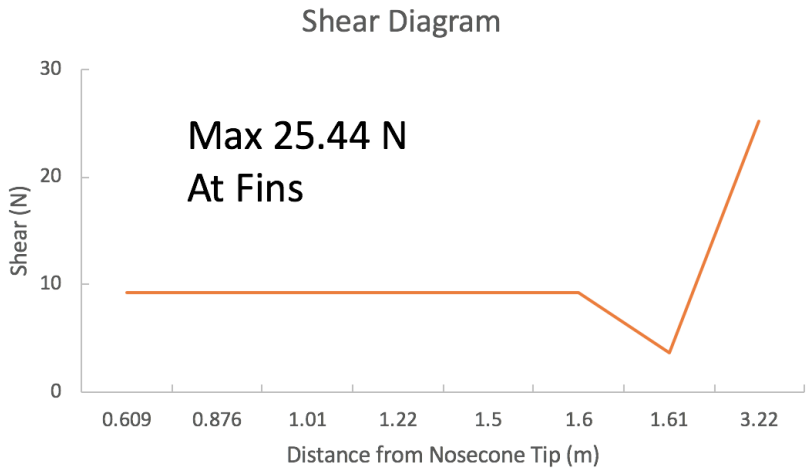

Figure 59: Drogue Shear Forces

5.2.3 Maximum Loading Condition: Main Deploy

The loading condition on the rocket during main deployment was calculated using values collected from the trajectory code and from simple extrapolation of the given information shown below in Table 25. It was assumed the parachute deployed axially in relation to the rocket's body.

Table 25: Rocket Properties at Main Deploy

Property	Value
Acceleration	69.08 m/s^2
Velocity	41.90 m/s
AOA	0.00°
Drag at Nosecone Tip	3176.00 N
Normal Force on Body	3.49 N
Location of CP (from nosecone)	2.64 m
Location of CG (from nosecone)	1.99 m
Horizontal Wind Velocity	0.00 m/s

To complete the analysis each load transferring component had its downstream mass calculated. As stated in the recovery analysis document, deployment will occur axially, since rocket will already be falling in this direction under the drogue. This generates purely axial loads in the structure. These masses are shown in Table 26.

Table 26: Component Properties at Main Deploy

Property	Downstream Mass (kg)	Distance to Cp (m)
Main/PL	9.80	1.97
AV 2	9.80	1.70
AV 1	21.60	1.57
Drogue/Press Upper	35.20	1.36
Press Lower	0.91	1.08
Thrust	40.20	0.98
Ox Tank	11.90	0.97
CC	10.20	0.64
Fins	0.00	0.72

These values were then converted into axial loads using Newton's Second Law. Specifically, axial forces were calculated using Equation 111, neglecting drag force. A visual representation of these loading conditions is seen in Figure 60.

The resulting forces acting on the rocket were as expected. Axial results are shown below in Figure 61. A maximum axial force of 12987.87 N occurred at the first avionics bulkhead, which follows as it had the largest downstream stream mass. Shear and moment, under the assumption of vertical deployment, are zero on main deploy.

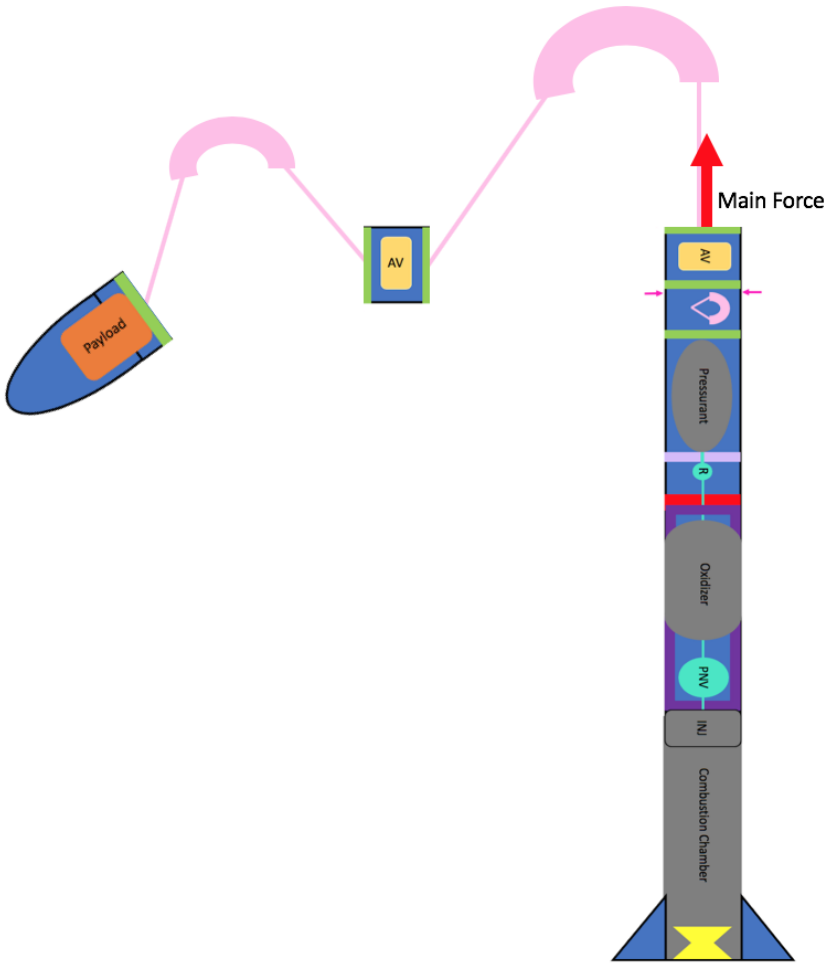

Figure 60: Loading at Main Deploy

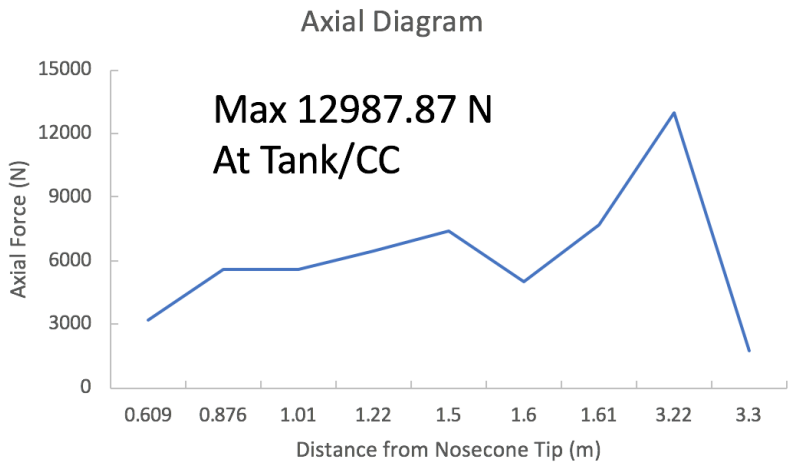

Figure 61: Main Axial Forces

5.2.4 Minimum FOS of Major Components

It may be noted that the FOS determined by the structural FEA was significantly higher than those displayed in Table 27. This may be attributed to the insufficient analysis done by the SolidWorks FEA software on fasteners and their joints. As such the FOS to be reported was the lower of the two values, and no further mass optimization was performed (as it would drop hand calculated FOS below 1.5).

Table 27

Component	FOS
Body Tubes/Couplers	1.81
Tank Skirts	1.65
Thrust Bulkhead	1.57
Pressurant Bulkhead	1.51
Pressurant/Drogue Bulkhead	1.57
Avionics 1 Bulkhead	1.52
Avionics 2 Bulkhead	1.50
Main/Payload Bulkhead	1.51

5.3 Finite Element Analysis

5.3.1 Pressurant Tank and Oxidizer Tank FEA

The tank designs were analyzed using SolidWorks FEA to determine whether the tanks will fail when subjected to both internal and external applied loads. The first tank to be analyze was the pressurant tank where the nitrogen gas is stored at high pressure. Using the equations from Section 3.3, it was calculated that a thickness of 0.0083 m was required for the pressurant tank to have a minimum factor of safety of 1.5.

For the FEA analysis, the tank was exposed to internal load of 2550 Psi. Figures 62 and 63 show the results obtained from SolidWorks case study. It can be observed that the maximum stress experienced by the tank was $1.215 * 10^8 N/m^2$ which is less than the yield strength of $2.75 * 10^8 N/m^2$. From Figure 63, the minimum factor of safety is 2.091. This is higher than the factor of safety used to design the thickness of the tank, which over estimated the thickness required.

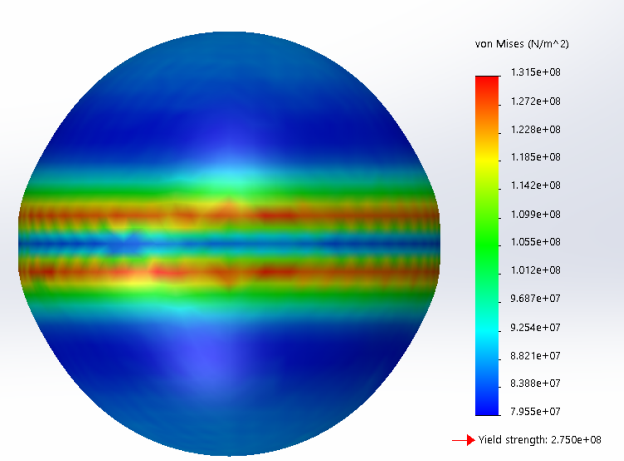

Figure 62: Stress plot for the pressurant tank

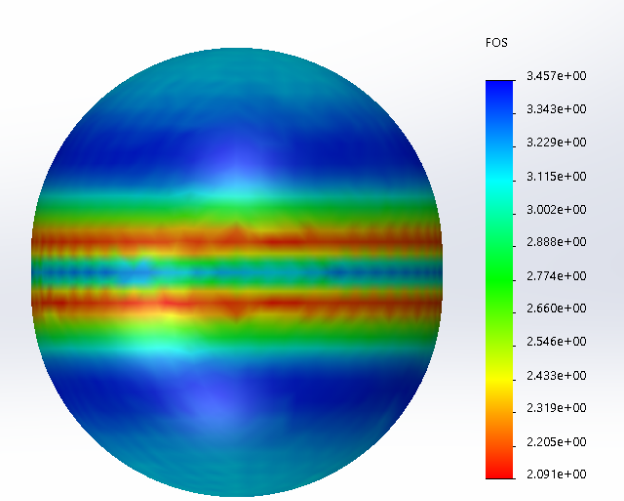

Figure 63: Factor of safety plot for the pressurant tank

In a similar way, the oxidizer tank was analyzed using SolidWorks. Using the same equations from Section 3.3, it was calculated that a thickness of 0.0028 m was required for the oxidizer tank to have a minimum factor of safety of 1.5.

For the FEA analysis, the oxidizer tank was exposed to a internal load of 799.07 Psi and a external axial force of 9,881 N. The oxidizer tank was also subjected to a bending load of 3,545.71 N-m. From Figure 64, it can be seem that the maximum stress experienced by the tank was $1.784 * 10^8 N/m^2$ which is less than yield strength of $2.75 * 10^8 N/m^s$. From Figure 65, it can be seen that the factor of safety is 1.542 which is less than 1.5. Both tanks will not fail under these conditions when exposed during the rocket's flight. Table 28 summarizes both the parameters for the pressurant tank and the oxidizer tank.

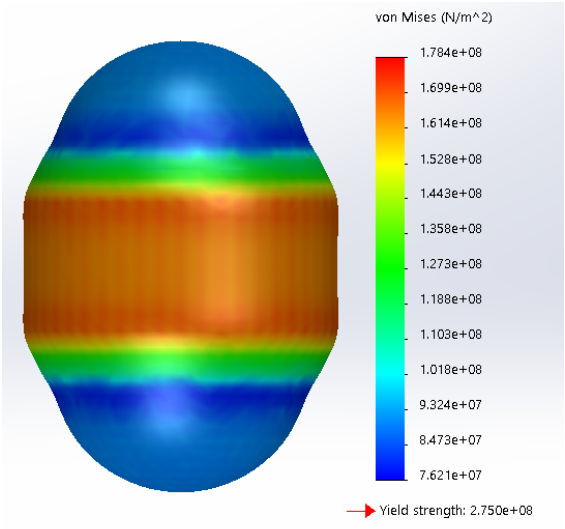

Figure 64: Stress plot for oxidizer tank

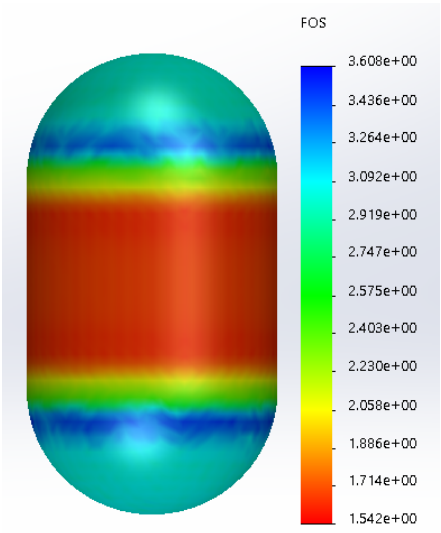

Figure 65: Factor of safety plot for the oxidizer tank

Table 28: Tank dimensions for the pressurant and oxidizer tank

	OD (m)	Length (m)	Thickness (m)	Wet Mass (kg)	Dry Mass(kg)	Material
Pressurant Tank	0.1957	0.21361	0.0083	0.8859	2.9457	Al 6061-T6
Oxidizer Tank	0.1957	0.3602	0.0028	10.1287	1.6558	Al 6061-T6

5.3.2 Bulkhead FEA

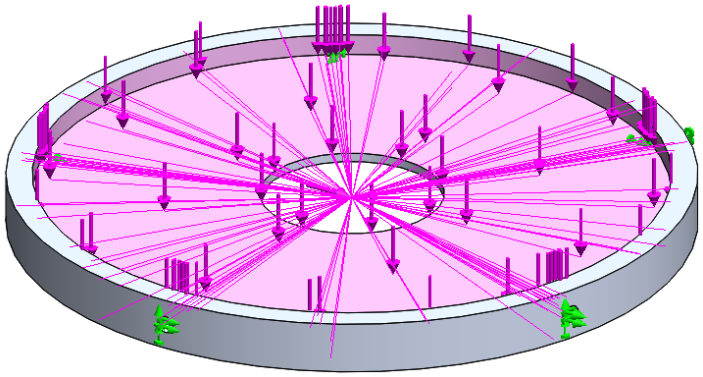

Figure 66: Bulkhead FEA setup

For each bulkhead, there were two loads and one boundary condition placed. This can be seen in Figure 66. The purple lines represent the loads and the green lines represent the boundary conditions. One load is the pressure force felt during max Q, and the second force is the bending moment experienced. The latter of the forces was approximated as a force acting on the entire part. The boundary conditions are fixed supports inside each of the 5 screw holes of the bulkhead. Material properties such as the Modulus of Elasticity and Poisson's Ratio were given through the material assignment in SolidWorks. For all of the bulkheads, the material used was 6061-T6 aluminum.

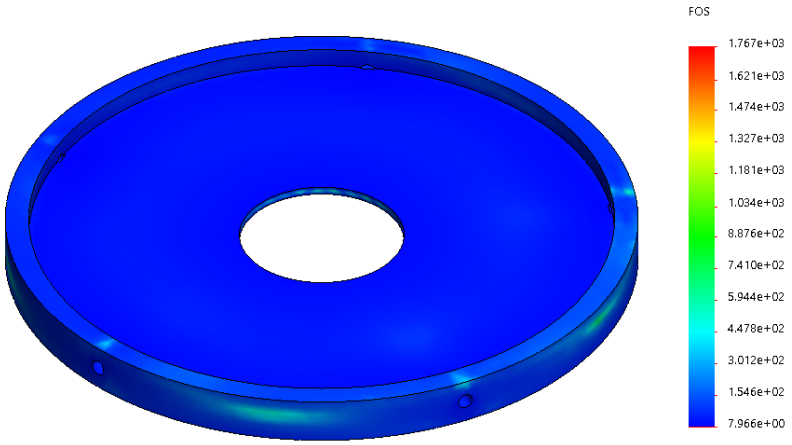

Figure 67: Pressure Bulkhead FEA Results

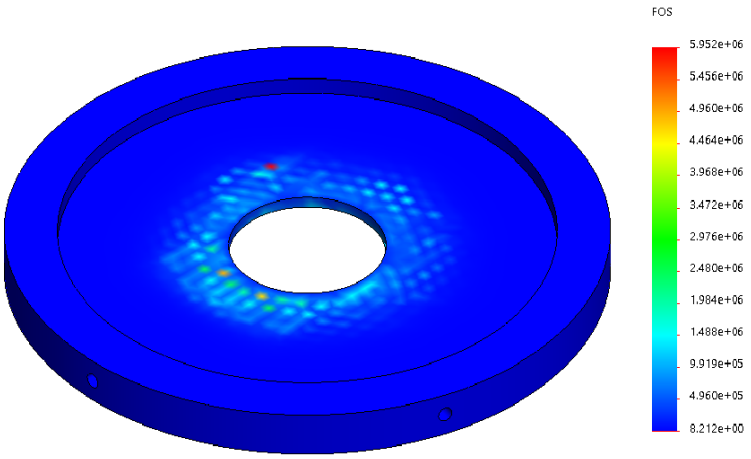

Figure 68: Thrust Bulkhead FEA Results

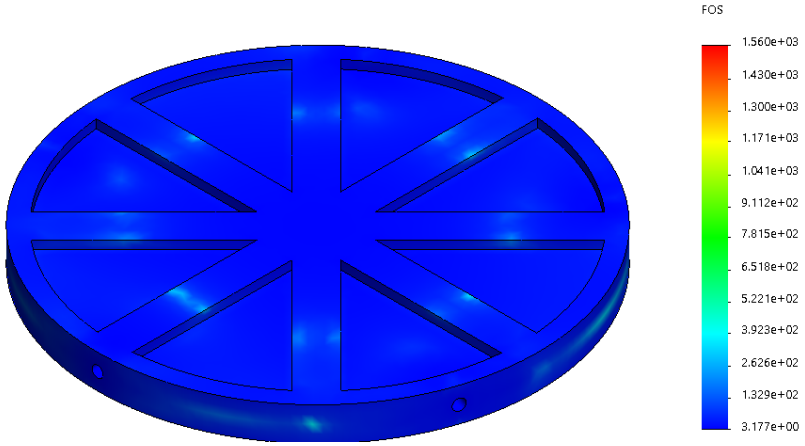

Figure 69: Recovery Bulkhead FEA Results

Table 29: Minimum factor of safety results from FEA

	Thrust	Pressure	Recovery
Minimum FoS	8.21	7.96	3.18

The results summarized in Table 29 show that the factors of safety for the bulkheads are rather large. It is worth noting that these results are only for the bulkhead parts themselves, and the FEA analysis conducted did not model fasteners that support the bulkheads, which are more likely to fail before the bulkheads due to their small relative size.

This rocket contains 4 recovery bulkheads, and Figure 69 shows the bulkhead with the lowest factor of safety. This is the bulkhead that is between the drogue parachute and the pressurant tank.

The geometry for the recovery bulkheads was designed in part by a SolidWorks Design Study. This takes a parametrized model and varies each dimension to return an optimized output.

Variable View | Table View | Results View

Run | Optimization | Total active scenarios: 1620

Variables

InnerCircleThickness	Range with Step	Min:	1in	Max:	3in	Step:	0.5in
OuterRingThickness	Range with Step	Min:	0.25in	Max:	0.75in	Step:	0.25in
StiffenerThickness	Range with Step	Min:	0.5in	Max:	1in	Step:	0.25in
NumStiffeners	Range with Step	Min:	3.000000	Max:	8.000000	Step:	1.000000
BulkheadThickness	Range with Step	Min:	1in	Max:	2.25in	Step:	0.25in
Click here to add Variables							

Figure 70: Design Study Parameters

5.3.3 Tank Skirt FEA

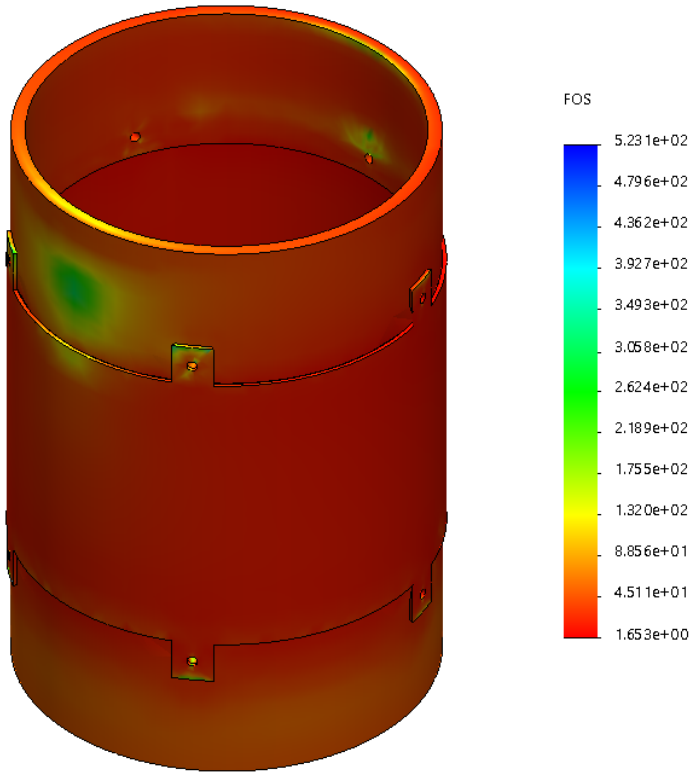

Figure 71: Tank Skirt FEA

FEA was done on the tank skirts and the minimum factor of safety was determined to be 1.653. This analysis neglects the fastener failure. It is loaded with an axial and body force to represent axial loading experienced during max Q and the bending moment respectively. The boundary conditions have the part being fixed on its top and bottom face to simulate being welded onto tanks.

6 Computational Fluid Dynamics

Computational Fluid Dynamics (CFD) is a valuable tool which can be used to predict the performance of an engine, and/or the aerodynamic characteristics of a body (i.e. lift, drag, and pressure). This provides a cost effective alternative to building and testing the body of interest. Limitations of CFD are that simulations can be time consuming, not entirely accurate, and require heavy computing power. For our project, CFD was done on the rocket body and fins and on the nozzle. For the rocket we predicted drag and drag coefficient and for the nozzle thrust and exit velocity. The nozzle simulation was verified with NASA's CEA software.

6.1 Rocket Body - External

For the rocket body, an asymmetric simulation was done with out the fins to predict the drag on the body. The Spalart-Allmaras model and a density based solver were used. The chosen inlet velocity was 200 m/s with sea level atmospheric conditions at the outlets. CFD for a single fin was also performed and its drag (x4) was added to the total drag on the body to get an adjusted C_D shown in Table 32. It is also seen in Table 32 that 65.26% of the drag is base drag due to the vacuum formed at the base of the rocket. This can be reduced with a boat tail.

Table 30: Mesh characteristics

Property	Value
Number of Elements	54,950
Global Element Size	6 in
Element Size Near Body	0.5 in
Orthogonality Average	0.98335
Inflation Layers	12
Y+	1
First Layer Thickness	6.950E-05

Table 31: Boundary Conditions Imposed, Operating Conditions 101,325 Pa

Geometry	Condition
Left Wall (blue)	Inlet, 200 m/s
Right Wall (red)	Outlet, 0 gauge pressure
Top Wall (green)	Farfield, 200 m/s, 0 gauge pressure
Bottom Wall (yellow)	Axis
Rocket Body (pink)	Wall, No slip

Table 32: Drag force and coefficients

Property	Value
Total Drag on Body	413.08 N
Pressure Drag on Body	269.54 N
Drag on Fin	8.433 N
Adjusted C_D	0.594

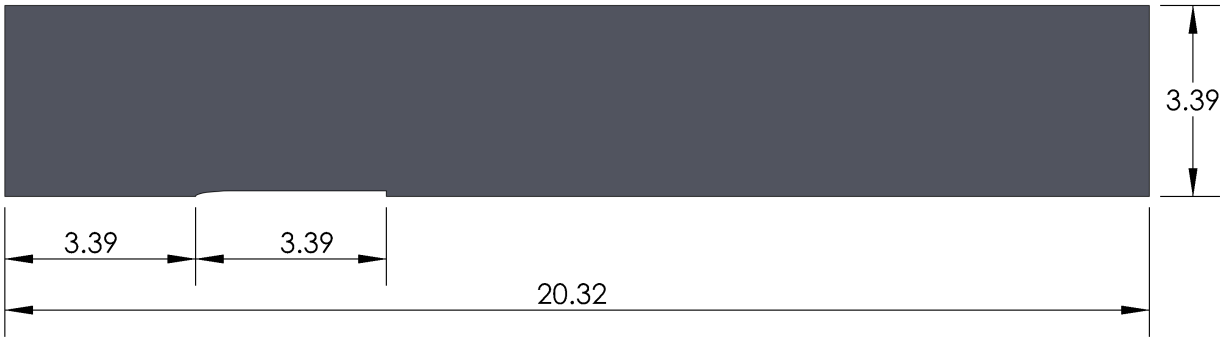

Figure 72: Dimensioned ANSYS domain in meters

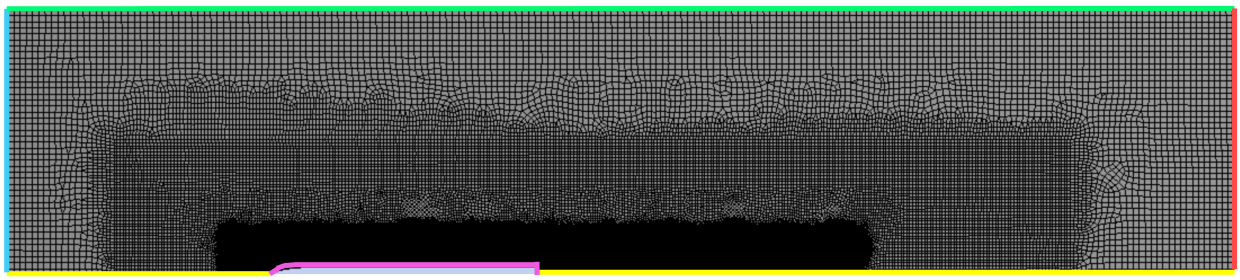

Figure 73: Mesh generated by ANSYS

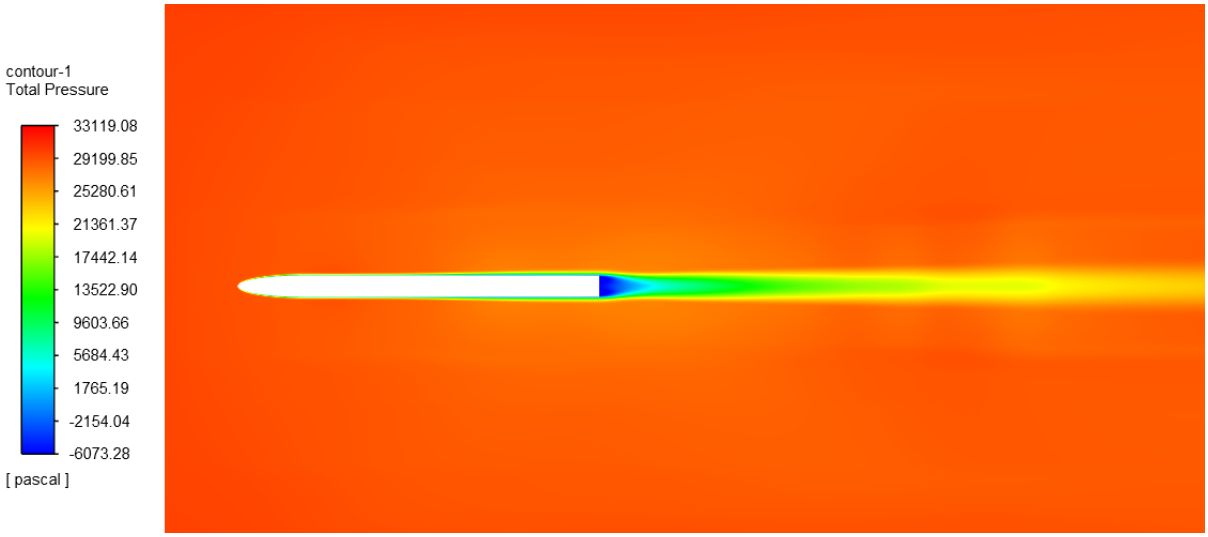

Figure 74: Total pressure contour for the body of the rocket

6.2 Fin - External

An external CFD analysis was performed for the airflow over one of the fins attached to the rocket body to predict the pressure field around a fin and to determine drag. The domain was created by taking a cavity of one quarter of the rocket end with the fin at a 45° from the horizontal domain plane. The dimensioned domain is given in Figure 75. The Spalart-Allmaras model and a density based solver were used. The inlet velocity is 200 m/s at a 0° angle of attack with sea level atmospheric conditions at the outlets.

The mesh was generated by ANSYS is shown in Figure 76. An internal view is given in Figure 77 to show the mesh on the fin. The fin mesh characteristics are given in Table 33. The boundary conditions imposed are tabulated in Table 34.

Table 33: Fin mesh characteristics

Property	Value
Number of Elements	489155
Global Element Size	1.45 in
Element Size Near Body	0.70 in

Table 34: Boundary Conditions Imposed, Operating Conditions 101,325 Pa

Geometry	Condition
Left Wall (red)	Inlet, 200 m/s
Right Wall (blue)	Outlet, 0 gauge pressure
Top Wall (orange)	Farfield, 200 m/s, 0 gauge pressure
Bottom Wall(yellow)	Axis
Fin Wall (purple)	Wall, No slip
Rocket Body Wall (green)	Wall, No slip

The 3D fin CFD analysis predicted the drag on a single fin to be 8.433 N. A slice of the pressure contour over the fin is given in Figure 78. From the figure, the pressure contour is symmetrical about the fin chord. This is expected since the angle of attack is 0°. This also results in the highest static pressure of 23208 Pa occurring at the leading edge where the stagnation point is located. As the airflow travels over the diverging contour of the fin, the pressure decreases sharply to -4714 Pa symmetrically. The pressure increases once the airflow travels over the converging taper of the fin.

The vertical and horizontal velocity streamlines with respect to the fin chord plane over the fin are shown in Figure 79 and Figure 80, respectively. From the velocity streamlines, it can be seen that the airfoil slows down as it approaches the leading edge of the fin, increases as it travels over the the fin, then slow down again as it approaches the trailing edge of the fin.

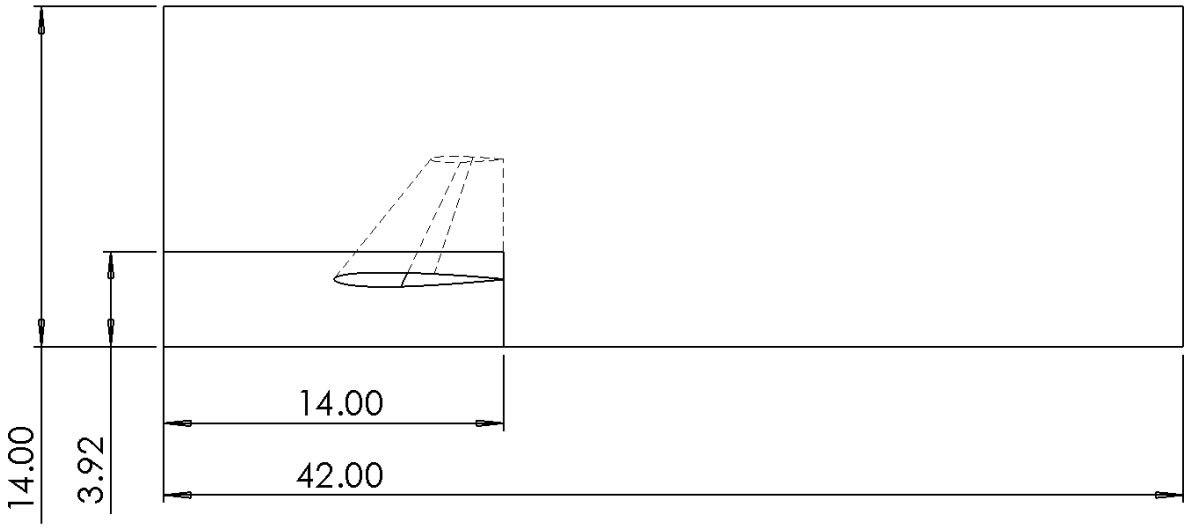

Figure 75: Dimensioned fin domain in inches

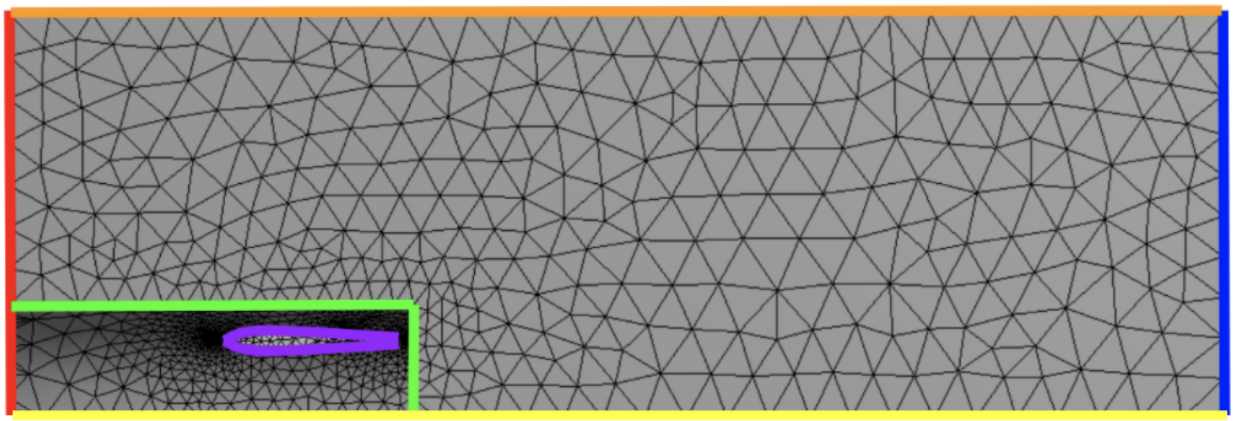

Figure 76: Fin mesh generated by ANSYS

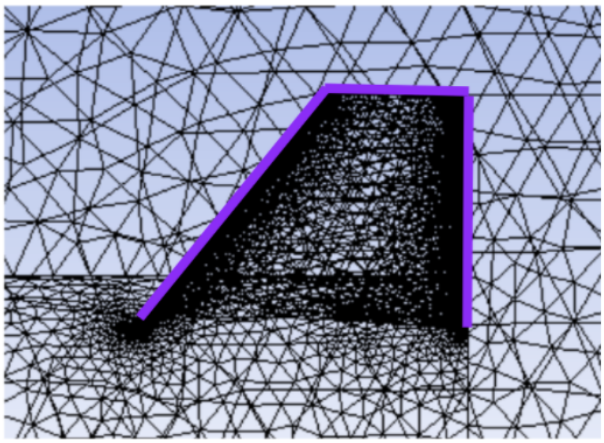

Figure 77: Fin mesh generated by ANSYS - internal view

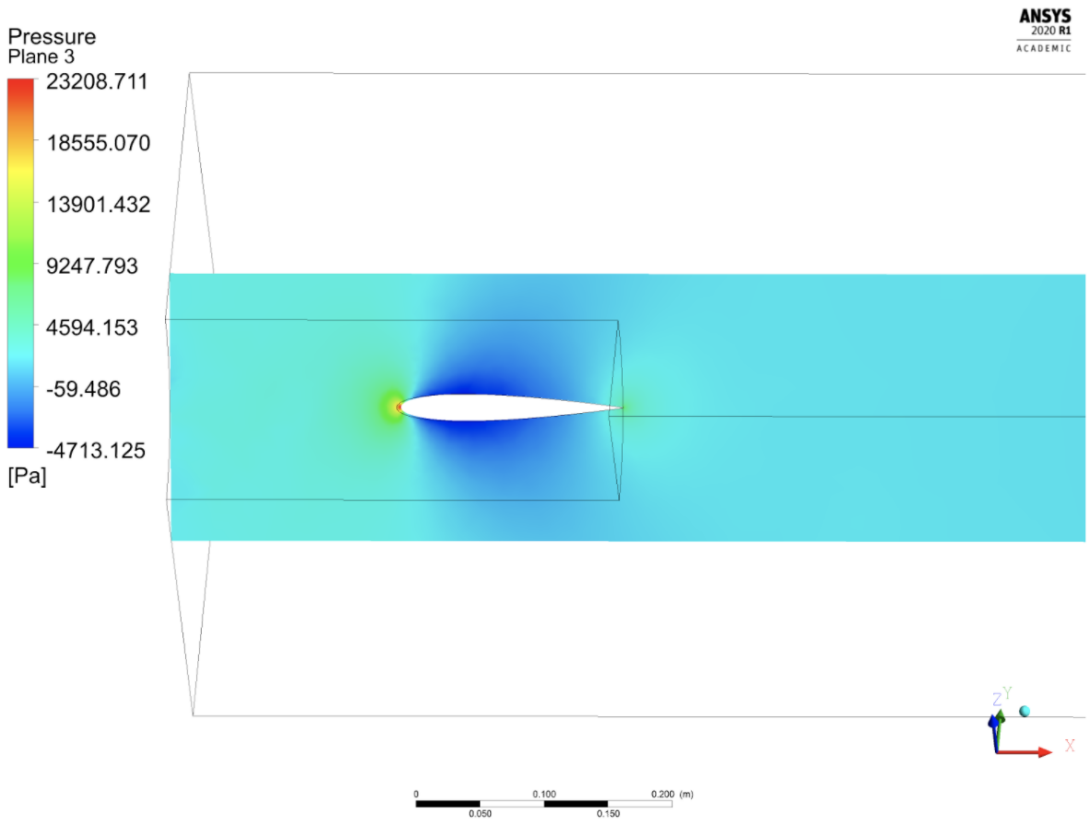

Figure 78: Fin pressure contour slice

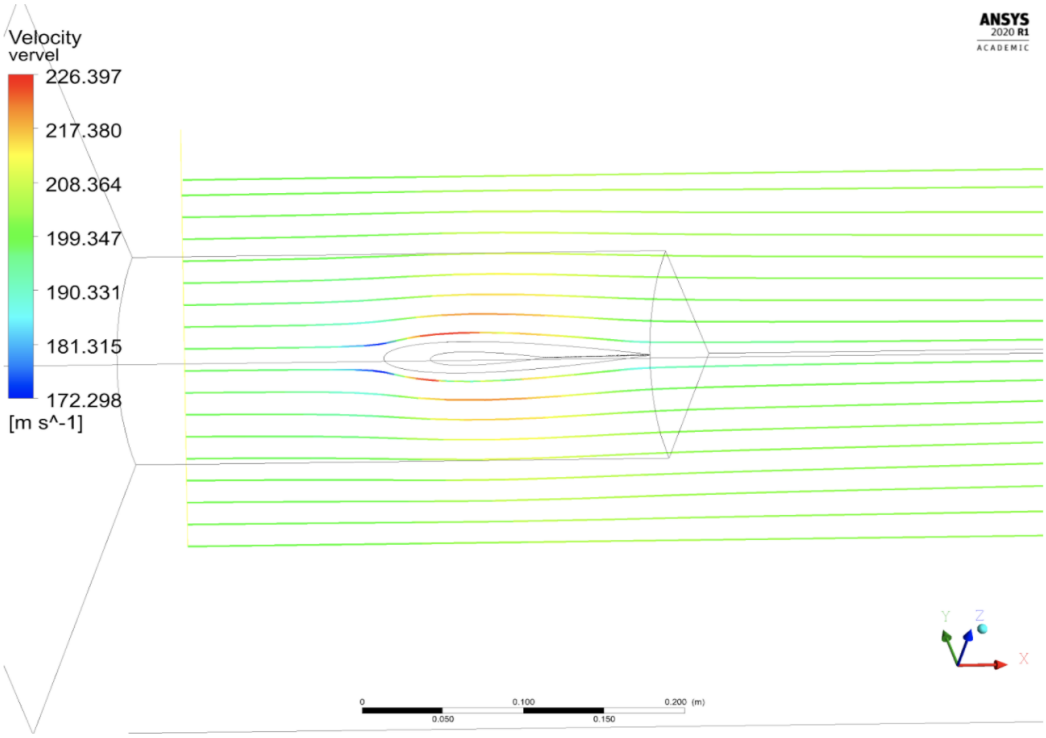

Figure 79: Fin vertical velocity streamlines

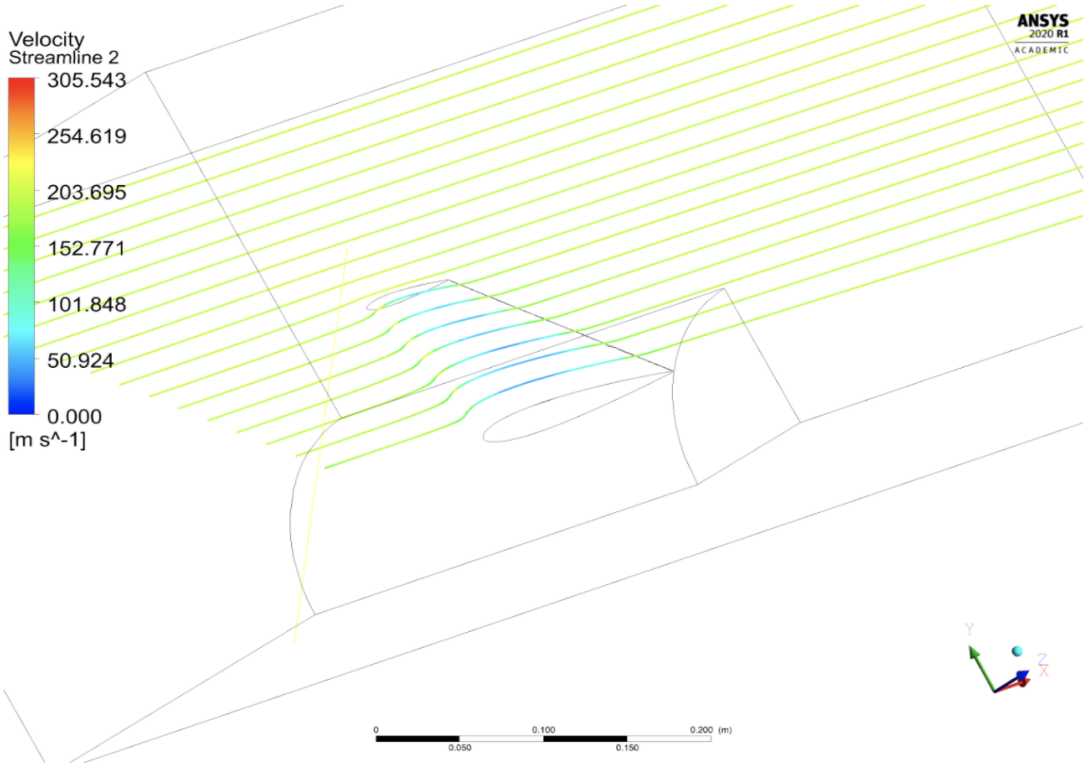

Figure 80: Fin horizontal velocity streamlines

6.3 Nozzle - Internal Flow

The nozzle performance predicted by CEA was validated using an axis-symmetric simulation on ANSYS. The Spalart-Allmaras model and a density based solver were used. The simulation was done at sea level conditions at which our nozzle is perfectly expanded and inlet conditions were those of the combustion chamber predicted by CEA. See apendix B for the CEA output file. Tables 35 - 37 show important settings and characteristics of the simulation.

Table 35: Mesh characteristics

Property	Value
Number of Elements	43092
Global Element Size	0.3 in
Element Size Near Body	0.07 in
Orthogonality Average	0.99489
Inflation Layers	12 (Smooth Transition)

Table 36: Boundary Conditions Imposed reference Figure 82, Operating Conditions 0 Pa

Geometry	Condition
Blue Wall	Inlet, P = 5,515,800 Pa, T = 3668.21 K
Green Wall	Outlet, P = 101,325, T = 298 K
Red Wall	Walls Nozzle Outer, No Slip, T = 298 K
Pink Wall	Walls Nozzle Inner, No Slip, T = 900 K
Yellow Wall	Axis

Table 37: Combustion gasses properties

Parameter	Quantity and Unit
Density	Ideal Gas
C_P	19610 J/kg-K
Thermal Conductivity	0.34179 W/m-K
Viscosity μ	0.00011142 kg/m-s
Molecular weight	23.774 kg/kmol

Table 38: CFD predicted performance

Parameter	Quantity and Unit
$\dot{m}_{tot}$	1.746 kg/s
P_e	132151.88 Pa
$u_e(axial)$	2948.33 m/s
A_e	0.0049278 m^2
Thrust	5300 N

Figure 81: Domain used for CFD simulation, units (mm)

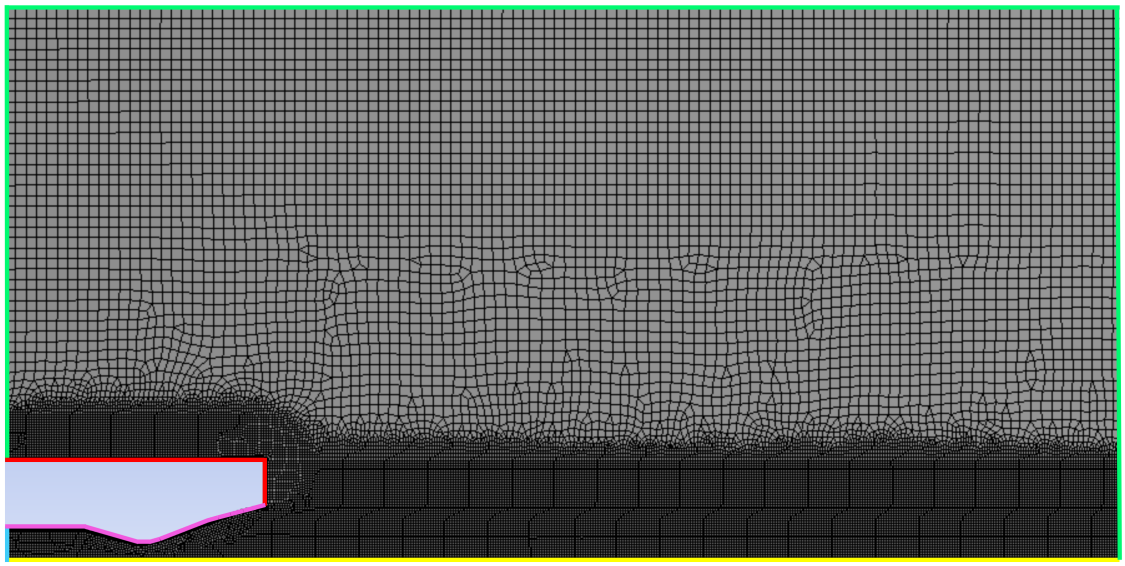

Figure 82: Mesh generated for simulation, color coded for boundary conditions

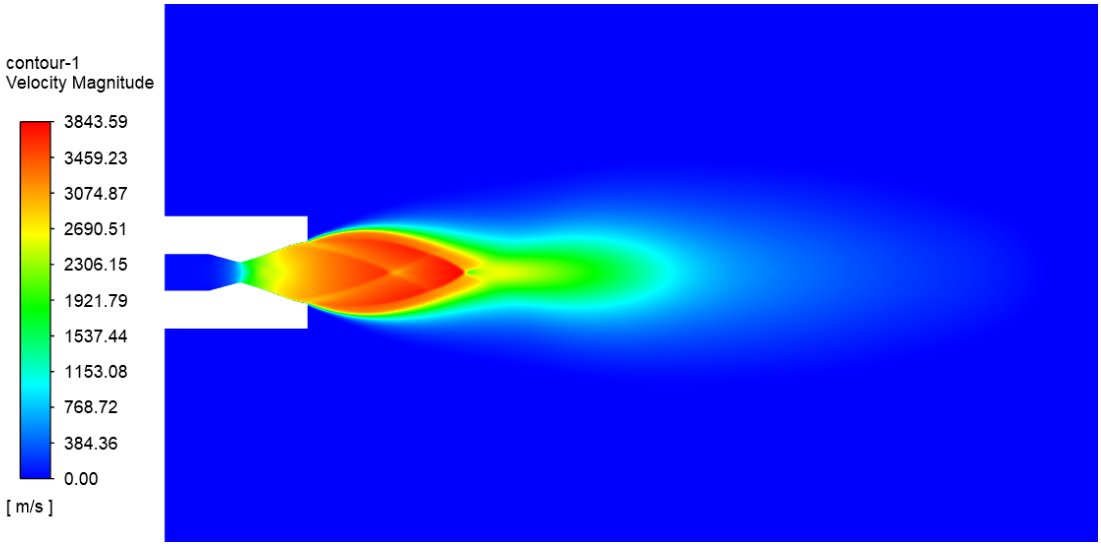

Figure 83: Velocity magnitude plot of nozzle solution

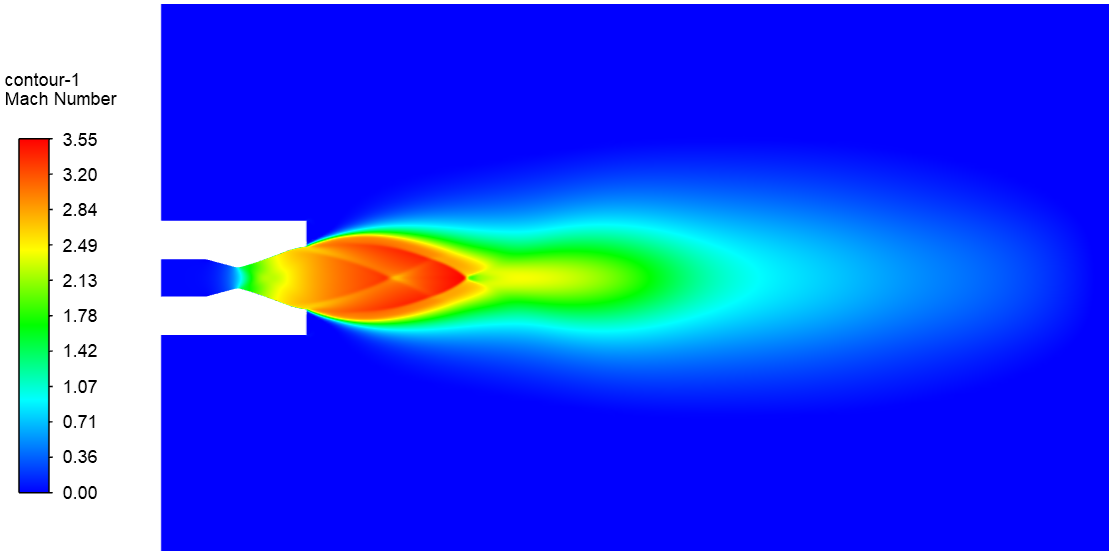

Figure 84: Mach number contour of nozzle solution

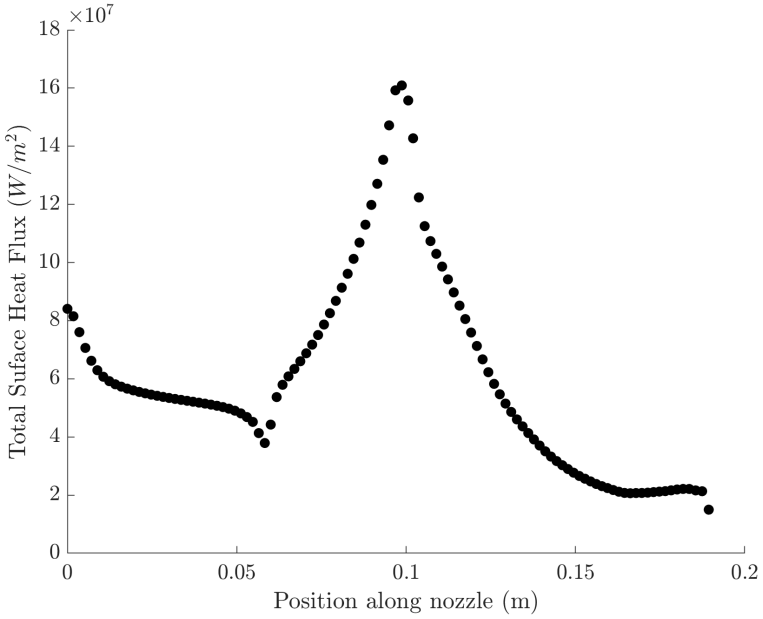

Figure 85: Heat flux plot along the walls of the nozzle

From Table 38, the thrust obtained using ANSYS is 5300 N. Using the properties in Appendix B the thrust predicted by CEA can be determined using Equation 6. This gives a thrust of 5205.5 N. CFD predicts about 100 N higher which is a percent difference of 1.78%. From Table 38, we can also see that the nozzle is not fully expanded at sea level. $P_e > P_a$ and so it is slightly under-expanded. The area weighted average mach number at the exit predicted by CFD is 2.734 and by CEA 2.981 corresponding to an 8.286% difference. Lastly, the mass flow rate predicted by CEA is 1.8235 kg/s and 1.746 kg/s by CFD for a percent difference of 4.25%. These results are summarized in Table 39.

Table 39: Comparison between CEA and CFD

Parameter	CFD	CEA
Thrust	5300	5205.5
Mach exit	2.734	2.981
$\dot{m}_{tot}$	1.746	1.8235

Figure 85 shows the heat flux across the nozzle walls. The peak heat flux occurs around 0.1 m or 100 cm. This corresponds to the nozzle throat shown in Figure 81. This makes sense because the heat transfer coefficient is proportional to the ratio $\dot{m}^{0.8}/D^{1.8}$ and because the mass flow rate is constant we can see that the max and min heat flux occur at the locations where the diameter is minimum (throat) and maximum (exit).

7 Production and Budget

7.1 Raw Materials and Fabrication Plan

Table 40: Table of raw materials required to manufacture each major rocket component

Component	Materials	Vendor
Nose Cone	6.0 oz. Fiberglass Fabric	Fibreglast
	System 2000 Epoxy Resin	Fibreglast
	System 2120 Epoxy Hardener	Fibreglast
Body Tubes	4.0 oz. Unidirectional Carbon Fabric	Fibreglast
	System 2000 Epoxy Resin	Fibreglast
	System 2120 Epoxy Hardener	Fibreglast
Oxidizer Tank	Aluminum 6061-T6 Sheet	Online Metals
	Aluminum 6061-T6511 Extruded Round Bar	Online Metals
Pressurant Tank	Aluminum 6061-T6511 Extruded Round Bar	Online Metals
Injector	Stainless Steel 304 Round Bar	McMaster-Carr
Combustion Chamber	Low-Carbon Steel Sheet	McMaster-Carr
	Low-Carbon Steel Rod	McMaster-Carr
Nozzle	Conductive Graphite Rod	McMaster-Carr
Fins	CDX Grade Plywood Sheets	McMaster-Carr
	6.0 oz. Fiberglass Fabric	Fibreglast
	System 2000 Epoxy Resin	Fibreglast
	System 2120 Epoxy Hardener	Fibreglast
Fuel Grain	Paraffin Wax Bar	McMaster-Carr
	R45M HTPB Resin	Aerocon Systems
	Papi 94 Curative	Aerocon Systems
Bulkheads	Aluminum 6061 Rod	McMaster-Carr

7.1.1 Nose Cone

The nose cone of the rocket will be fabricated using 14 rolls of 6-ounce fiberglass fabric measuring 1 yard in length, 38" in width, and 0.01" in thickness. A 1:1 scale projected view of an elliptical female mold is first constructed out of ABS plastic using a 3D printer. The resultant nose cone mold is intended to be 7.8" in outer diameter and 23.88" along its length. The inside of the mold will be completely coated in wax and left to dry on the work table for approximately 15 minutes before the surface is buffed to remove excess wax. This process is to be repeated at least 3 times to ensure the inner surfaces of the mold have been

thoroughly coated. When the wax-covered surfaces have dried, FibRelease is applied onto the inner surfaces of the mold and allowed to dry for another 15 minutes. This process will also be repeated at least 3 times to ensure there is sufficient FibRelease on the mold to enable gentle separation of the finished nose cone from the mold. Thin rectangles measuring the length of the nose cone are traced on wax paper and outlined with a sharpie. The rectangular outlines are intended to cover the surface area of the inside of the mold. It is noted that a sufficient amount of space should be left in between each sketch to reduce the chances of mistakes while cutting. A rectangle measuring the length of the seams and a width of about 0.5" is to be sketched in addition to the thin rectangular strips.

When the preparations are completed, there will be enough cutouts for an estimated 14 layers of the fiberglass lay-up. Without the consideration of added thickness due to the epoxy mixture, the number of cutouts are ensured to achieve the intended nose cone thickness of 0.39". A layer of 3M Super 77 adhesive spray will be applied onto the wax imprints from a substantial distance away to warrant that only a thin layer is used. Laying the wax paper over a fiberglass sheet, creases and air pockets can be prevented from forming by lightly pressing down on the sheet. Using an X-Acto knife, the sketches will be cut out and placed on a flat work surface with the fiberglass facing upward. The System 2000 epoxy resin is mixed with the System 2120 epoxy hardener at a weight ratio of 100:27. Once the resin and hardener have been mixed together, there will only be 2 hours to work. The epoxy mixture is spread over the fiberglass at a 45° angle using putty knives. The wax paper cutouts will be detached from the fiberglass and set inside the female mold, lightly pressing down to remove air bubbles. Approximately 0.25" of excess fiberglass on either side of the molds will be leftover for the sealing of seams in a later step.

When the molds are ready to be joined, they will be placed together such that the region of overlapping fiberglass is contained inside the mold. The overhang can be pressed down upon delicately with fingers to make sure the overlap sticks together. If there is a gap at the tip of the nose cone profile, epoxy is added such that it sets at the tip. The rectangular seam will be laid along the corresponding seam within the mold. Fastening the molds together, the nose cone will stand such that the tip is in contact with the work surface. This allows the epoxy mixture to settle and fill the gap at the tip. It is expected that fewer than 14 layers of fiberglass will be needed. When the lay-up is completed, the nose cone and mold will be left to cure for at least 24 hours. The molds are unfastened after 24 hours and the nose cone carefully separated from it. Using sand paper, rough edges along the tip and the seam can be smoothed out. Any excess, unwanted fiberglass will be trimmed away with a Dremel. The aft end of the nose cone will be sanded along the edge, gradually reducing the diameter to create a coupler for later fitting into the body tubes.

7.1.2 Body Tubes

The body tubes of the rocket will be manufactured from 42 rolls of 4-ounce unidirectional carbon fabric measuring 1 yard in length, 1 foot in width, and 0.006" in thickness. The 4 body tubes will be fabricated independently, one at a time. The 4 body tubes are projected to measure 8.66", 16.54", 14.96", and 73.62" lengthwise, respectively. An aluminum 6061 tube will be used as the mandrel in the carbon fiber lay-up process.

The perforated high-temperature release film, nylon peel ply, breather, and high-temperature vacuum bagging films are measured and cut to the dimensions of the corresponding body tube. Several extra inches in both length and width of the films, peel ply, and breather will be left intentionally to be cut away later if necessary. An ample amount of carbon fiber fabric will be measured and cut to cover the surface area of the body tube. It is estimated that a maximum of 7 layers of pre-impregnated carbon fiber are needed. It is expected that the carbon fiber will ultimately be wrapped around the mandrel fewer than 7 times, achieving a thickness of 0.04". The industrial standard of a 0.5" overlap is taken into consideration for each ply.

Using sealant tape, the perforated high-temperature release film will be attached to the aluminum mandrel. The epoxy resin and epoxy hardener are mixed at a weight ratio of 100:27 by hand. Once the resin and hardener are determined to be well-blended, there will only be 2 hours left to work. Gently, a layer of the epoxy mixture will be brushed onto the carbon fabric. The impregnated carbon fiber is wrapped around the

mandrel, leaving approximately 0.5" of overlay. When the body tube has reached an outer diameter of 7.8". the nylon peel ply will be wrapped and secured with sealant tape around the laminate layers. Around the peel ply, the vacuum bagging film will likewise be wrapped and fastened with sealant tape, followed by the breather. More sealant tape will be used along the perimeter of the bagging film such that it makes contact with the aluminum mandrel. A PTFE tube will be inserted into the bagging, after which the bag is closed, taking care to avoid air pockets around the sealant tape. The vacuum pump is switched on to verify there are no gaps for air to escape within the vacuum.

The bagged assembly will be placed inside an industrial oven and cured at a temperature between 120°F and 130°F for about 12 to 14 hours. When the curing process has been finished, the oven will be switched off and the assembly allowed to cool to room temperature. The carbon fiber body tube should be carefully removed from the mandrel. Protrusions are trimmed off with a Dremel and rough edges can be sanded off. The edges of the cuts will be sanded down to slightly reduced diameters, creating couplers to aid the assembly of the vehicle. On the 73.62" body tube, slots corresponding to the placement of the fins will be measured and cut.

7.1.3 Oxidizer Tank

The aluminum sheet stock is first measured to its appropriate dimensions matching the design specifications of the tank body. A sheet metal brake will be used to cleanly cut the sheet to a length of 6.48" and width of 24.18". Between 0.06" and 0.08" worth of margin are to be leftover for welding the seams. The sheet will be rolled along its length using a metal sheet roller into a cylindrical body measuring an outer diameter of about 7.7". With a Scotch-Brite, impurities are brushed from the metal surface and a clean work table will be prepared.

The seams of the oxidizer tank body will be attached by way of TIG welding. It is decided that while surfaces are typically chamfered for better ease of welding, a chamfer is not needed in the case of the oxidizer tank because the sheet stock is relatively thin. Instead, some overlap will be allowed to be welded at the seams.

The aluminum round bar will be measured and cut into two equal halves to be machined into the spherical end caps of the oxidizer tank. One of the halves will be chucked in the lathe and turned until its inner spherical profile is developed and the required inner diameter of 7.46" is reached. Because the oxidizer tank is made of aluminum, a faster feed rate can be employed in the process of machining the end caps. The same process will be repeated for the other spherical end cap. With the outer cylindrical profile of the stock exposed to the tool, the cap will be milled to gradually shape the outer spherical profile. The operation will be halted when an outer diameter of 7.68" is achieved. The same milling process is to be applied to the other cap.

The inner and outer surfaces of both end caps will be polished with sand paper to a smooth finish. With a Scotch-Brite, impurities are cleaned from the edges of the end caps and tank body and a clean work space will be prepared for welding. The end caps and tank body will be joined using TIG welding, after which one end of an aluminum tank skirt will be welded to the top spherical end cap of the oxidizer tank in the same manner. A second tank skirt will be manufactured from aluminum and mild steel to accommodate the different materials from which the oxidizer tank and combustion chamber were fabricated. The aluminum end of the second tank skirt will be TIG welded to the bottom spherical end cap. The tank is allowed to sit and cool to room temperature before a post-welding heat treatment is performed to restore material strength properties. After it has cooled again, the tank will be bathed in sulfuric acid for a type II anodizing finish. The acid should be properly disposed of while the tank and work areas will be carefully cleaned.

Type II anodizing is often the most common, cost-effective, and easiest anodizing process to be performed in-house. However, one challenge inherent to the manufacturing of the oxidizer tank will be achieving the type II anodized finish despite limitations in materials, equipment, knowledge, as well as concerns over safety and environmental impact. Of these factors, the safety of the work space is paramount because the type II anodizing process will be involving a hazardous chemical such as sulfuric acid. Proper protective gear will

need to be worn and instructions pertaining to the handling and disposal of sulfuric acid to be carefully reviewed and understood by all participants in the process. A typical type II anodizing of aluminum 6061 will involve a repeated cycle of soaking the component in a heated tub of concentrated sodium hydroxide, rinsing with de-ionized water, and bathing in concentrated sulfuric acid. Toxic waste from the rinse water and concentrated chemical baths may not always comply with local sewage standards and will need to be adequately removed elsewhere in accordance with local regulations. Exhaust fans and ducts with high corrosion resistance will be required to ensure the fumes are appropriately ventilated from the work space. A lack of experience or knowledge about the process or a limited availability of the appropriate containers for these chemicals will have the potential to pose danger to the personnel in the surrounding work space.

7.1.4 Pressurant Tank

The pressurant tank is manufactured by first measuring and cutting the aluminum 6061 round bar into two shorter, identical bars measuring 4.2" in height. Between approximately 0.06" and 0.08" of extra height are allowed to remain for welding. Chucking one work piece into a lathe, the work piece will be turned to carve out an inner hemisphere with a 2.86" radius. Because the tank is built from aluminum, it is appropriate to employ a faster feed rate during the machining process. In the lathe, the work piece will be turned to create a 0.85" long cylindrical inner profile extending from the edges of the inner hemisphere. The inner radius of the cylindrical extension should be maintained at 2.86". Moving the work piece to a mill, the outer hemisphere will be developed to measure an outer radius of 3.35". A 0.85" long cylindrical outer profile extending from the edges of the outer hemisphere will be milled to keep the outer radius of the cylindrical body at 3.35". The process is to be repeated for the other work piece.

When both spherical caps have been finished, sand paper is used to polish the inner and outer profiles. The edges of each spherical cap are cleaned with Scotch-Brite and a clean work space will be readied for welding. The caps will be joined by TIG welding. Similar to the oxidizer tank, one end of the aluminum tank skirt will be joined with the spherical end cap of the pressurant tank through TIG welding. The welded pressurant tank is cooled to room temperature before a post-welding heat treatment is performed to restore material strength properties of the completed tank.

7.1.5 Injector

The injector is fabricated by first measuring and cutting the stainless steel 304 round bar to the required length of 3.94". An excess 0.5" worth of length will be leftover for the machining of the flange. The round stock is chucked in the lathe and sufficient material will be removed such that the ends are straight and square. Because the injector is made of stainless steel, the lathe can be operated at a feed rate faster than that of carbon steel but slower than those of graphite and aluminum.

In the lathe, the injector inlet will be turned to a diameter of 0.79", shaping the inlet side contour in the process. Using a drill bit, the oxidizer inlet port will be created. The oxidizer manifolds will be lathed using a dog leg tool and a skinnier boring tool to enable more flexible access to small, tight spaces. On a drill press, the injector is oriented such that the inlet side was up. Bolt holes will be drilled and tapped along the circumference of its flange. The contour of the injector flange is machined such that the thickness of the flange will allow a press fit slightly over the combustion chamber when bolted to the flange mount.

From the remainder of the stainless steel round bar, a thin disc will be measured and cut to manufacture the injector face plate. Chucking the plate into a lathe, the contour of the injector face will be machined. On a drill press, 36 oxidizer injection holes measuring diameters of 0.055" will be carefully drilled into the face plate. The oxidizer injection holes and oxidizer manifolds will be carefully deburred.

Using a Scotch-Brite, the metal edges of the injector body and injector face plate will be cleaned. A clean work surface will be prepared for welding. The injector face plate will be joined to the injector body through TIG welding. The welded injector is allowed to cool to room temperature before a post-welding heat treatment is applied to restore material strength properties.

It will be expected to be difficult to drill the extremely fine oxidizer injection holes and to machine the intricate patterns of the injector contours and manifolds. The dog leg tool can be used to offset the tool rest and access the otherwise hard to reach sections. The machining of the injector will also be operated at a slower feed rate than is typically necessary for stainless steel to minimize the chance of errors.

7.1.6 Combustion Chamber

The combustion chamber is manufactured by first measuring the mild steel sheet stock to their intended length and width of 48.4" and 24.18", respectively. The sheet stock will be cut into 2 pieces using a sheet metal brake. The stock used to fabricate the fuel grain housing section of the chamber is measured to match the length of the fuel grain, 42.7", while the remainder of the stock is used to manufacture the post-combustion section of the chamber. Between 0.06" and 0.08" worth of margin will be reserved for welding of the seams as well as joining the fuel grain housing and post-combustion compartments of the chamber. It is noted that low-carbon steel is more difficult to machine than aluminum, graphite, and stainless steel; a slow feed rate will be used when machining the combustion chamber.

Both mild steel sheets will be rolled along their lengths into cylinders measuring an outer diameter of 7.7" using a metal sheet roller. Impurities are cleared from the metal surfaces using a Scotch-Brite while a clean work area is prepared. Due to the thinness of the metal sheet, the edges of the sheet where welding will be done are not chamfered. Instead, the seams will be allowed to overlap by the amount of margin determined in the beginning of the fabrication process.

The seams are melted and joined by metal inert gas, or MIG, welding. The shorter rolled work piece, or post-combustion chamber, is set aside. A groove with a depth of approximately half the chamber thickness will be milled inside each end of the fuel grain housing. Two internal retaining rings will be machined by chucking the low-carbon steel rod into a lathe and cutting about 0.25" worth of stock. The removed stock is machined to make two rings with diameters matching the depths of the internal grooves in the fuel grain housing. With another 0.75" of the low-carbon steel rod, two disks measuring the same lengths will be cut. The injector mount flange will be machined to have a press fit over one end of the fuel grain housing tube. The nozzle housing mount flange is likewise machined to have a press fit over one end of the post-combustion chamber tube.

Using a drill bit, injector mount holes will be drilled and tapped at one end of the fuel grain housing, taking care that the internal grooves are not distorted in the process. Between 0.03" and 0.05" of additional thickness will be leftover to be machined away after welding the mount to the chamber. Nozzle housing mount holes will be drilled and tapped along the other end of the post-combustion chamber. Additional thickness is allowed to remain until machined away after welding the mount to the chamber. From the remainder of the mild steel sheet, two concentric circles measuring the inlet diameter of the nozzle (1.87") and the outer diameter of the combustion chamber (7.7") will be carved out using a waterjet cutter. Impurities will be cleaned from the metal surfaces using Scotch-Brite while a clean work surface is prepared.

Using MIG welding, the annular end plate will be fixed to the end of the post-combustion chamber. The ends of the fuel grain housing and the post-combustion chamber are fused together using the same welding method. The injector mount flange will be attached to the outside of one end of the fuel grain housing compartment while the nozzle mount flange is attached to the outside of the opposite end of the chamber by MIG welding. Using the same welding technique, the mild steel end of the second tank skirt will be joined to the body of the combustion chamber. The finished chamber is allowed to cool to room temperature before a post-welding heat treatment will be applied to restore material strength properties. In a lathe, the injector mount flange will be faced where the flange seats and cut to reach a final flange thickness. The thickness is determined such that the chamber was still able to slide into the body tubes.

7.1.7 Nozzle

The graphite stock used to fabricate the rocket nozzle will first be measured and cut to a required nozzle length of 4.87" with about 0.08" extra length presuming that the cut is not square. Chucking the work piece

in the lathe, enough material will be removed such that both ends are straight and squared. The length of the nozzle should be equal to the specified nozzle length. The lathe can be operated at a feed rate slower than that of aluminum, but faster than that of stainless steel. Material will be turned from the outer surface such that the outer diameter of the nozzle work piece measures 7.6".

Operating at a slower rate, a groove will be carefully machined along the outer surface of the nozzle near the nozzle exit. Using the drilling bit, a hole is made at the center of the work piece on both ends. Measuring a hole with the size of the nozzle throat diameter (1.09"), the work piece is drilled about halfway through before it is turned around to drill the remainder. The throat will be bored through to its design diameter.

The inner converging taper of the nozzle will be shaped using a boring tool. The work piece will be reversed and bored to its inner diverging taper. The diverging profile will be turned down to the required diverging angle. The inlet and exit diameters will be turned to measure 1.87" and 3.12", respectively. The roughness of the inner flow surface can be smoothed out with sand paper. The graphite dust should be cleaned from the floor using a vacuum and from the hands using soap and warm water.

The tapering of the inner diverging profile is expected to be the most time-consuming and laborious step in the nozzle manufacturing process. Using a boring tool to carve out the entire conical section at once is a common yet effort demanding approach. Given the small size of the nozzle and the significance of achieving the correct design parameters, careful attention and a slower feed rate will be required of this process. A second approach that can be implemented in replacement is the use of a drilling bit instead of a boring tool to drill successive, incremental sizes. A "stepped profile" will be the result of this drilling and will be bored to its final smooth profile. The drilling method is expected to reduce the time and effort required in the shaping of the diverging section. The only caveat intrinsic to this method is that the depth of each drilling increment will need to be meticulously determined for adequate tolerance of inaccuracies. This method was adapted from the machining experiences documented in *Machining of Rocket Nozzles*.

7.1.8 Fins

Using a Dremel, 4 right trapezoidal profiles with bases matching a root chord of 7" and tip chord of 3", height measuring the span at 4", and a sweep measuring 7", are cut from the plywood sheet. A pencil is used to mark guiding lines for beveling the trailing and leading edges. The result is intended to be a smooth, symmetric profile matching that of the NACA 0012 airfoil. With a sanding block, the leading edge of one fin will be sanded at an angle of 45°. The fin is flipped over and the same process will be repeated along the leading edge.

Flipping the fin back over to the opposite surface, the angle of the sanding block will slowly be decreased. The process should be paused frequently to check that the profile is smooth and even. The fin will gradually be sanded from the edge down to the marked line where the bevel is intended to begin. The fin is continuously sanded until the original 45° bevel is gone and the entire bevel is even and straight. Turning the fin over, the same will be done to the other surface. In a back-and-forth motion, the sanding block will slowly be maneuvered around the leading edge to round it off. The same procedure is repeated for the trailing edge, sanding it to a narrow edge and leaving it square.

The fin profiles will be traced and wax paper will be overlaid onto a 1:1 scale drawing of the fin. The profiles are outlined with a sharpie, making sure to leave a substantial amount of space in between each sketch. A thin layer of 3M Super 77 adhesive spray will be applied onto the wax imprints. The wax paper will be laid over a fiberglass sheet, taking care to prevent creases and air pockets from forming. With an X-Acto knife, the drawings will be cut and placed on a work surface with the fiberglass facing up. Epoxy resin is mixed in with the epoxy hardener at a weight ratio of 100:27, leaving only about 2 hours to work.

With putty knives, the epoxy mixture will be applied to the fiberglass at a 45°. The fiberglass cutouts are separated from wax paper and wrapped over the plywood fin core. Air bubbles can be removed by pressing down gently with the fingers. Approximately 0.25" of excess fiberglass will be allowed to overlap between

cutouts. After curing the fins for at least 24 hours, the fins will be sanded off and trimmed with a Dremel to completion.

The beveling of each individual fin is not expected to be an impeccable mirroring of the NACA 0012 airfoil. The handcrafting of the fins will be expected to result in slight discrepancies and a lack of perfect uniformity across all 4 fins. The sanding of the leading and trailing edges will be largely dependent on the judgements of the person carrying out the process, making it difficult to ensure accurately beveled profiles across all 4 fins. While the challenge of fin beveling will be taken into consideration, it is not expected to produce large deviations such that the analysis and design of the fins are rendered invalid.

7.1.9 Bulkheads

The aluminum round bar is cut into 6 discs measuring 0.57" each. Chucking one disc into a lathe, the outer diameter will be turned to measure 7.8", the diameter of the rocket body. With the disc flat and one circular face up, the contour of the bulkhead will be milled. The disc is flipped over to expose the opposite face, after which the corresponding contour will be milled. Employing the clocking tool in this procedure will assist in rotating the work piece without moving the cutter, for ease and better accuracy in the milling of bulkhead contours. Repeating the process for all the bulkheads, their surfaces will be polished with sand paper for a smooth finish.

7.1.10 Fuel Grain Casting

Two concentric circular profiles will be made on the plywood sheet using a waterjet cutter. The annular end caps are cut to match the fuel grain outer diameter and inner diameter of 7.63" and 6.18", respectively. The paraffin wax bar will be melted in a boiler and stirred slowly and periodically. The casting environment is set up by carefully placing an aluminum pipe in the center of a cylindrical stand. One end will be enclosed by an end cap and secured in place with sealant tape. The outermost surface of the aluminum pipe will be lubricated with petroleum jelly to prevent the HTPB resin from binding to the metal.

The casting tube will be slid over the aluminum pipe sitting on the cylindrical stand. Melted paraffin wax, R45M HTPB resin, and the Papi 94 curative will be carefully poured into the casting tube, pooling around the aluminum pipe at the center. The top of the casting tube will be closed off with the other end cap and sealant tape. Moving the casting assembly to a lathe, the fuel grain will be spun at a low rotational speed to cure for about 2 hours. This fuel grain casting technique was incorporated based on research results presented in "UCLA Rocket Project Paraffin System". This will enable more uniform mixing of the raw materials and prevent air pockets from forming inside the fuel grain. After it has had sufficient time to cure, the fuel grain will be gently removed from the casting tube.

7.2 Assembly and Integration

7.2.1 Motor Assembly

The nozzle, nozzle housing, combustion chamber, phenolic liner, and injector are gathered together on a clean, flat work surface. Sliding the fuel grain inside the phenolic liner, the fuel grain will be secured. It is noted that the liner can be further sanded down to a more desired thickness. The internal fuel grain grooves will be filled with an RTV sealant such as Permatex. Permatex will be added to the inside corners of the internal retaining rings, after which the fuel grain is carefully slid into the place from the injector end of the chamber. Before wiping excess Permatex from the ring joints and the injector end of the chamber, it will be ensured that the fuel grain is securely seated.

Applying Permatex to the nozzle retaining ring and the groove near the nozzle exit, the nozzle will be secured inside the nozzle housing. Sliding the nozzle housing such that it is a slight press fit over the combustion chamber, the nozzle will be firmly seated as the housing is bolted into the corresponding housing mount flange on the post-combustion chamber. Excess sealant will be wiped away. The injector will be cleaned and its inlet port capped to prevent contamination from entering through the opening. Sliding the

injector into a press fit over the combustion chamber, the injector is clocked such that its flange matches the bolt holes on the flange mount. It will be bolted into place.

A pressurant bulkhead is to be fitted and fastened at the bottom of the pressurant tank while a thrust bulkhead is similarly fitted and fastened at the top of the oxidizer tank. The pressurant and oxidizer tanks will be connected by fastening the welded sections of the aluminum tank skirt to the corresponding bolted middle section of the tank skirt. In a similar manner, the welded sections of the second tank skirt will be bolted to its matching middle section, effectively attaching the tank assembly to the combustion chamber.

7.2.2 Fin Can Assembly

One at a time, the fins and fin can are to be coated with epoxy along the surface where the fins will be fixed. Sliding a fin into its slot in the fin can, the fillet is shaped by filling the angle between the components with epoxy. Once completed for all 4 fins, excess epoxy outside the desired thickness of the fillets will be cleaned away.

7.2.3 Recovery and Payload Installation

The first recovery bulkhead will be fitted and secured to the aft end of the 16.54" body tube. The drogue parachute, a 45' shock cord, and two carbon dioxide ejection systems are carefully folded and packed into the drogue parachute bay at the bottom of the tube. A second recovery bulkhead will be fitted and secured atop the drogue bay in the same body tube. The avionics bay, containing the altimeters, perfboard, and batteries, will be installed. A third recovery bulkhead is fitted and secured between the avionics bay and main parachute bay, after which the 16.54" body tube will slide into the 8.66" body tube until the coupler is no longer visible. The tubes will be bolted together at their points of separation. Shear pins will be screwed in at the second recovery bulkhead situated between the avionics and drogue bays and again at the third recovery bulkhead located between the main and avionics bays.

The main parachute, a 36' shock cord, and black powder will be folded and packed into the main parachute bay sitting atop the third recovery bulkhead. Each of the bays will be vacuum-sealed to prevent pressurization leakage using an epoxy mixture and sealant tape. A fourth recovery bulkhead is fitted on top of the main parachute bay. The payload will be installed and secured on top of the fourth recovery bulkhead, after which the nose cone slides into the 8.66" body tube until the coupler is no longer visible. The nose cone and body tube will be bolted together at their points of separation.

7.2.4 Final Rocket Integration

A long work table will be set up to support a horizontal stand to hold the rocket components during the integration procedure. Sliding the fin can over the aft end of the motor assembly, the fin can will be bonded to the motor with epoxy. It is noted that it is not commonly good practice to use an adhesive on metals. The metal surface of the motor where the fin can will be fixed will be lightly scratched to create a more porous surface, enabling a better bond.

The motor assembly will be slid into and secured inside the 73.62" body tube, allowing the fins to protrude from the slots cut during the fabrication of the carbon fiber body tubes. The integration of the motor into the body tube will be difficult due to the extreme length of the 73.62" tube. The motor will be comprised of multiple heavy components and delicate, costly plumbing instrumentation. Extra caution should be taken when fitting the motor into the body tube to avoid the possibility of disrupting any joints or damaging any plumbing instrumentation. The final two assembled bodies will be combined and fastened at their points of separation. It is noted that the pressurant and oxidizer tanks will be able to vent through their respective pressure relief valves, disposing the need for vent lines.

7.3 Budget Plan

The projected budget for the rocket has taken into consideration the estimated costs of raw materials, consumables, tools, and commercial off-the-shelf components for all systems. Highlighted in Table 41, the total taxed cost was calculated to be $7,785.81 assuming a standard Los Angeles Country sales tax rate of 9.5%. According to this number, it was determined that approximately 52% of the allotted budget of $15,000.00 will be spent, leaving an excess of $7,214.19. The remainder of the allotted budget will be directed towards funding a wide range of expenses including materials and equipment for static fire testing, costs of traveling, components requiring professional rapid prototyping services, and replacements for defective materials or electronics.

Table 41: Estimated costs of each system, total cost before and after tax, and the original allotted budget

System	Total Cost
Structures	$1,478.98
Propulsion	$1,997.27
Recovery	$572.32
Avionics	$208.10
Plumbing	$2,853.66
Total	$7,110.32
Total (Tax Included)	$7,785.81
Allotted Budget	$15,000.00

Shown in Figure 86, the two most financially demanding systems were determined to be plumbing and propulsion. Together, the costs of propulsion and plumbing accumulated to comprise 68% of the total expenses, more than twice the amount projected to be spent on recovery, avionics, and structures combined. According to Table 42, the cost of acquiring plumbing instrumentation would dominate the majority of the budget spent on commercial off-the-shelf parts.

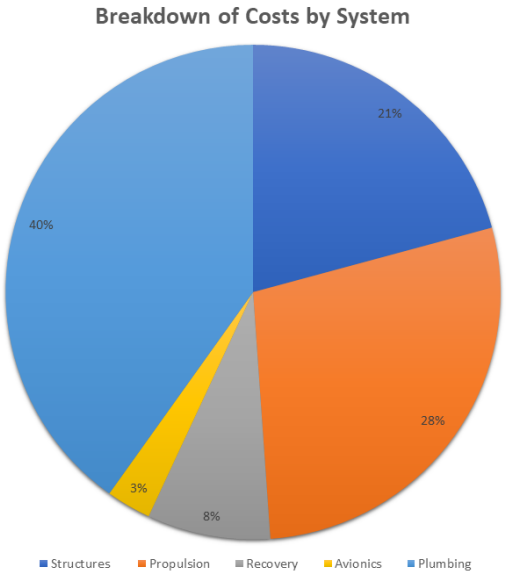

Figure 86: Pie chart displaying the projected material expenses of each system

Due to the presence of liquid oxygen in the motor, the purchase of several plumbing components was

decided on the basis of whether it was capable of tolerating cryogenic fluids. Often, this criteria became a limiting factor that hindered the search for these components as cryogenic pneumatics are low in commercial availability and high in price. Amongst the plumbing instrumentation, cryogenic-tolerant components were only found for pressure gauges, solenoid valves, and pressure relief valves, their prices and vendors displayed in Table 42. The remaining components, for which their cryogenic counterparts were not found, were assumed to be able to withstand cryogenic temperatures. All plumbing components considered for purchase were chosen to accommodate a $\frac{3}{8}$" line size, the respective desirable tank pressures, and maximum operational temperatures assuming a launch site in the desert.

The most expensive plumbing component to be purchased, shown in Table 42, is the KPF series pressure-reducing regulator manufactured and distributed by Swagelok. Situated between the pressurant and oxidizer tanks, the Swagelok regulator was customized to endure a maximum inlet pressure of 6000 psi and offer high flow capabilities with a flow coefficient, C_v, of 1. Assuming an FOS of 1.5, it was computed that the maximum upstream pressure expected to be withstood by the regulator would be 3825 psi. It was decided that the specifications of the Swagelok KPF pressure-reducing regulator would be more than sufficient to warrant the intended performance of the tanks.

Table 42: List of commercial off-the-shelf components, their prices, and vendors, pertaining to each subsystem

System	Component	Price	Vendors
Recovery	Main Parachute	$65.50	Rocketman Chutes
	Drogue Parachute	$67.16	Apogee Rockets
	Nylon Webbing Shock Cord	$71.46	Fruity Chutes
	Peregrine CO_2 System Kit	$338.00	Fruity Chutes
	Black Oxide U-Bolts	$30.20	McMaster-Carr
Avionics	EasyMini Altimeters	$184.62	Apogee Rockets
	9V Li Batteries	$13.49	Amazon
	Perfboard	$9.99	Amazon
Structures	Stainless Steel Flat Head Screws	$8.87	McMaster-Carr
	Nylon Shoulder Screws	$9.26	McMaster-Carr
	Permatex RTV Sealant	$14.61	Amazon
Plumbing	Pressure Gauges	$122.88	McMaster-Carr, Ashcroft
	Solenoid Valves	$384.38	McMaster-Carr
	Needle Valves	$356.86	McMaster-Carr
	Pressure Relief Valves	$130.68	McMaster-Carr
	Pressure Transducer	$309.92	McMaster-Carr
	Check Valves	$46.66	McMaster-Carr
	KPF Pressure-Reducing Regulator	$1,241.60	Swagelok
	Quick Release	$37.90	Amazon
	Flat 1 Pneumatic Actuator	$145.28	Bimba
	Threaded On-Off Valves	$77.50	McMaster-Carr

8 Conclusion

Over the past 10 weeks, our team has worked relentlessly to design a rocket from scratch. It was a learning experience for us all but in the end we all learned a lot about the iterative design process, working in a team, communication, and rockets! This report is a culmination of everyone's hard work and dedication to the project.

Starting from week one, the pace of the class was fast moving. Team roles were assigned, everyone learned FEA and a conceptual plan was developed. Weeks two and three the trajectory code for the rocket is in progress and a preliminary design is underway. Week four propellant trade studies are performed, the weight of propellant is estimated, and tanks are sized. Major motor components such as the nozzle and injector also get designed. Apogee predictions are obtained from the trajectory code and a design plan for structural components is written. Week five is the PDR and with all the feedback we were able to improve many areas of the motor and move towards the final stages of the project. The weeks after the PDR until now have been spent on structural analysis, CFD analysis and on the dynamic stability of the rocket as well as budget and manufacturing. The nozzles performance was evaluated using CFD, FEA on bulkheads was performed and a complete trajectory code was developed giving us confidence in the design.

The final design is a hybrid rocket with an elliptical nose cose and pressure fed system. The fuel grain is a 50-50 wt% HTPB - Paraffin composite. The gas and oxidizer tanks and combustion chamber are structural components of the carbon-fiber airframe held by tank skirts. Every component was designed by the team and simulations (CFD, FEA, CEA) were performed to verify hand calculations. The apogee reached by the rocket is 34,327ft and max mach number of 1.9 at burnout.

Given more time, some areas that could be improved are the heat transfer analysis of the combustion chamber, the dynamic stability of the rocket, and the analysis of some structural components that time did not permit for FEA. Overall, the rocket was designed from scratch, from the motor to bolts and everyone learned something new along the process. This class has been challenging for us all but none the less fun. We only wish that we had been able to manufacture our design and see it launch!

9 Acknowledgements

We would like would like to thank Professor Spearrin for his feedback in the PDR and CDR which helped us improve our designs. We would also like to thank Anil for his help with the trajectory portion of the project and all the suggestions and resources he provided to us at our weekly team meetings! We also want to thank David for the tutorials he provided and his lectures on CFD. Lastly, we want to thank all the teaching assistants, Anil, David, Chuyu and Quincy for their help with the labs which were stepping stones in completing this project.

Additionally, the team would like to acknowledge Aimee Pak who was voted by the team as the MVP for her contributions to CFD and for designing the nozzle, injector and CADing the motor components!

Lastly, we want to Congratulate Aimee Pak, China Hagström, and Anna Zhong who are graduating seniors! Aimee accepted an offer with Boeing, China is headed to MIT and Anna to UC Davis!

References

1. Pastrone, D. Approaches to low fuel regression rate in hybrid rocket engines. *International Journal of Aerospace Engineering* **2012** (2012).
2. Sutton, G. P. & Biblarz, O. *Rocket propulsion elements* (John Wiley & Sons, 2016).
3. Gamper E., H. R. Design and test of nitrous oxide injectors for a hybrid rocket engine (2013).
4. Mathur, J. *Introduction to wind energy systems: basics, technology and operation* (Springer, 2009).
5. in, 1–18 (2004).
6. Barrowman, J. S. The practical calculation of the aerodynamic characteristics of slender finned vehicles (1967).
7. Hagstrom, C. Project Prometheues at UCLA (2019).
8. Michaelson, B. *Rocketman Parachutes* `https://the-rocketman.com/chutes-html/` (2018).
9. *Apogee Components* `https://www.apogeerockets.com/Building_Supplies/Parachutes_Recovery_Equipment/Parachutes/High_Power/24in_Classic_Elliptical_Parachute` (2019).
10. Nakka, R. *Machining of Rocket Nozzles* `https://www.nakka-rocketry.net/nozmach.html` (2020).
11. Tirumalareddy, R. & Sivaram, S. UCLA Rocket Project Paraffin System (2010).

10 Team Roles

Table 43: Team Member Lead Roles (∗) and Contributions (✓)

	Aimee Pak	Anna Zhong	China Hagström	Jesus Legorreta	Jose Guerrero	Willy Teav
Project Engineer					∗	
Trajectory & Stability		✓		∗	∗	
Motor Design	∗				✓	
Structural Analysis			∗	✓	✓	✓
CFD Analysis	✓				∗	
CAD Design	✓					∗
Vehicle Layout			✓			∗
Production Plan		∗				
Budget		∗				

Vehicle Layout Section 2.1 was written by Willy. Section 2.2 was written by China.

Motor section was written and reviewed by Aimee and Jose. Analysis and writing of sections 3.1 - 3.4 was done by Jose. Analysis and writing of sections 3.5 - 3.7 was done by Aimee. The entire motor CAD and assembly was also done by Aimee.

Trajectory and Stability sections were written by Jesus, Jose and Anna. Sections 4.1 and 4.3 - 4.5 were written and reviewed by Jesus and Jose. Section 4.2 was written by Anna and reviewed by Jesus.

Structural Analysis was written by China, Jesus and Willy and reviewed by Jose. Sections 5.1 - 5.2.4 were written by China. Section 5.3.1 was written by Jesus and reviewed by Jose. Sections 5.3.2 and 5.3.3 were written by Willy.

CFD sections were written by Jose and Aimee. Sections 6.1 and 6.3 was written by Jose. Section 6.2 was written by Aimee.

Production and Budget Section 7 was written by Anna and reviewed by China and Aimee.

Appendix

A G. V. R. Rao bell nozzle

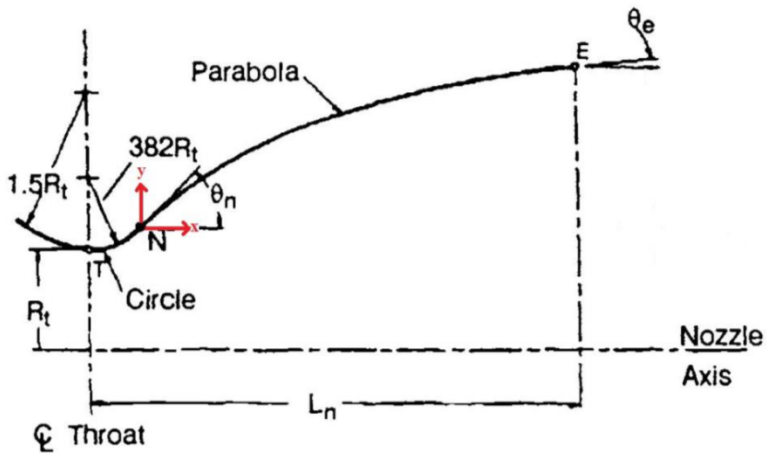

Figure 87: Bell nozzle design

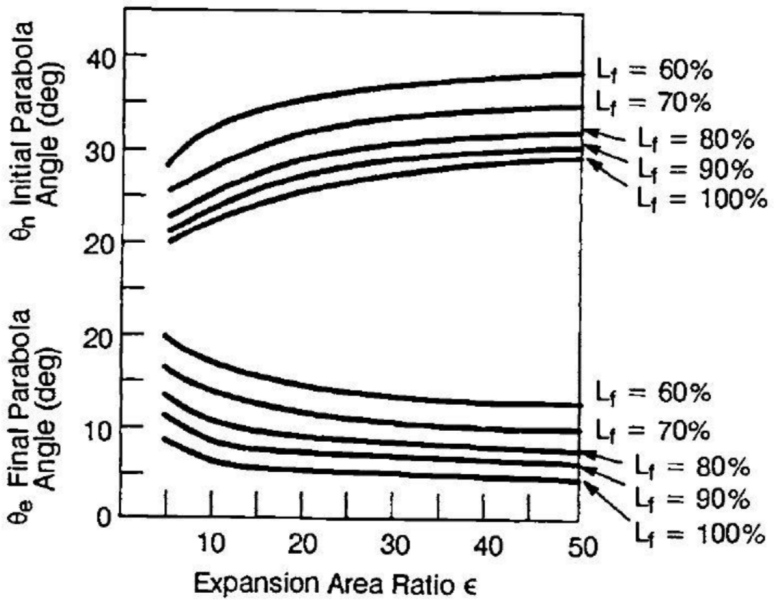

Figure 88: Bell nozzle initial and final parabolic angles

B NASA CEA Output File

```
        NASA-GLENN CHEMICAL EQUILIBRIUM PROGRAM CEA2, FEBRUARY 5, 2004
                  BY  BONNIE MCBRIDE AND SANFORD GORDON
     REFS: NASA RP-1311, PART I, 1994 AND NASA RP-1311, PART II, 1996

*******************************************************************************


### CEA analysis performed on Fri 05-Jun-2020 21:15:59

# Problem Type: "Rocket" (Infinite Area Combustor)

prob case=_______________7779 ro equilibrium

# Pressure (1 value):
p,psia= 800
# Chamber/Exit Pressure Ratio (1 value):
pi/p= 54.42177

# Oxidizer/Fuel Wt. ratio (1 value):
o/f= 2.4

# You selected the following fuels and oxidizers:
reac
fuel C4H6,butadiene    wt%= 50.0000
fuel paraffin          wt%= 50.0000
oxid O2(L)             wt%=100.0000

# You selected these options for output:
# short version of output
output short
# Proportions of any products will be expressed as Mole Fractions.
# Heat will be expressed as siunits
output siunits
# Transport properties calculated
output transport


# Input prepared by this script:prepareInputFile.cgi

### IMPORTANT:  The following line is the end of your CEA input file!
end

             THEORETICAL ROCKET PERFORMANCE ASSUMING EQUILIBRIUM

          COMPOSITION DURING EXPANSION FROM INFINITE AREA COMBUSTOR

Pin =   800.0 PSIA
CASE = _______________
```

```
            REACTANT                    WT FRACTION      ENERGY      TEMP
                                         (SEE NOTE)     KJ/KG-MOL      K
FUEL        C4H6,butadiene               0.5000000         0.000      0.000
FUEL        paraffin                     0.5000000  -1860600.000    298.150
OXIDANT     O2(L)                        1.0000000    -12979.000     90.170

O/F=    2.40000  %FUEL= 29.411765  R,EQ.RATIO= 1.369937  PHI,EQ.RATIO= 1.369937

                CHAMBER   THROAT     EXIT
Pinf/P            1.0000   1.7321   54.422
P, BAR            55.158   31.845   1.0135
T, K             3668.21  3481.64  2405.09
RHO, KG/CU M    4.2996 0 2.6526 0 1.2985-1
H, KJ/KG         -559.45 -1241.19 -4629.35
U, KJ/KG        -1842.31 -2441.72 -5409.90
G, KJ/KG        -41384.0 -39989.3 -31396.3
S, KJ/(KG)(K)    11.1293  11.1293  11.1293

M, (1/n)          23.774   24.113   25.619
(dLV/dLP)t      -1.04111 -1.03529 -1.00252
(dLV/dLT)p        1.7042   1.6389   1.0645
Cp, KJ/(KG)(K)    6.2222   5.9827   2.4473
GAMMAs            1.1391   1.1357   1.1734
SON VEL,M/SEC     1208.9   1167.7    957.0
MACH NUMBER        0.000    1.000    2.981

TRANSPORT PROPERTIES (GASES ONLY)
  CONDUCTIVITY IN UNITS OF MILLIWATTS/(CM)(K)

VISC,MILLIPOISE   1.1142   1.0753  0.83360

 WITH EQUILIBRIUM REACTIONS

Cp, KJ/(KG)(K)    6.2222   5.9827   2.4473
CONDUCTIVITY     14.3872  13.2661   3.8884
PRANDTL NUMBER    0.4819   0.4849   0.5247

 WITH FROZEN REACTIONS

Cp, KJ/(KG)(K)    1.9610   1.9533   1.8798
CONDUCTIVITY      3.4179   3.2607   2.3346
PRANDTL NUMBER    0.6393   0.6441   0.6712

PERFORMANCE PARAMETERS

Ae/At                      1.0000   8.3609
CSTAR, M/SEC               1780.8   1780.8
CF                         0.6557   1.6021
Ivac, M/SEC                2195.8   3126.6
```

```
        NASA-GLENN CHEMICAL EQUILIBRIUM PROGRAM CEA2, FEBRUARY 5, 2004
                  BY  BONNIE MCBRIDE AND SANFORD GORDON
     REFS: NASA RP-1311, PART I, 1994 AND NASA RP-1311, PART II, 1996

*******************************************************************************


### CEA analysis performed on Fri 05-Jun-2020 21:15:59

# Problem Type: "Rocket" (Infinite Area Combustor)

prob case=_______________7779 ro equilibrium

# Pressure (1 value):
p,psia= 800
# Chamber/Exit Pressure Ratio (1 value):
pi/p= 54.42177

# Oxidizer/Fuel Wt. ratio (1 value):
o/f= 2.4

# You selected the following fuels and oxidizers:
reac
fuel C4H6,butadiene    wt%= 50.0000
fuel paraffin          wt%= 50.0000
oxid O2(L)             wt%=100.0000

# You selected these options for output:
# short version of output
output short
# Proportions of any products will be expressed as Mole Fractions.
# Heat will be expressed as siunits
output siunits
# Transport properties calculated
output transport


# Input prepared by this script:prepareInputFile.cgi

### IMPORTANT:  The following line is the end of your CEA input file!
end

             THEORETICAL ROCKET PERFORMANCE ASSUMING EQUILIBRIUM

          COMPOSITION DURING EXPANSION FROM INFINITE AREA COMBUSTOR

Pin =   800.0 PSIA
CASE = _______________
```

C NASA's Atmospheric Model

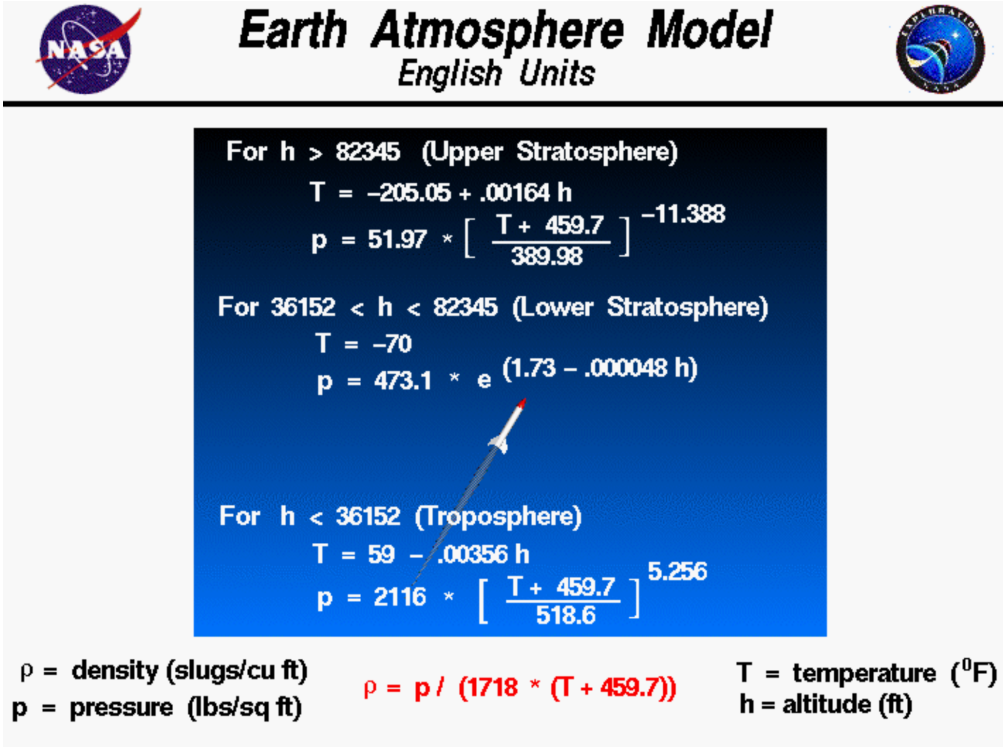

Figure 89: `https://www.grc.nasa.gov/WWW/K-12/airplane/atmosmet.html`

D Built-To Drawings

D.1 Rocket Overview

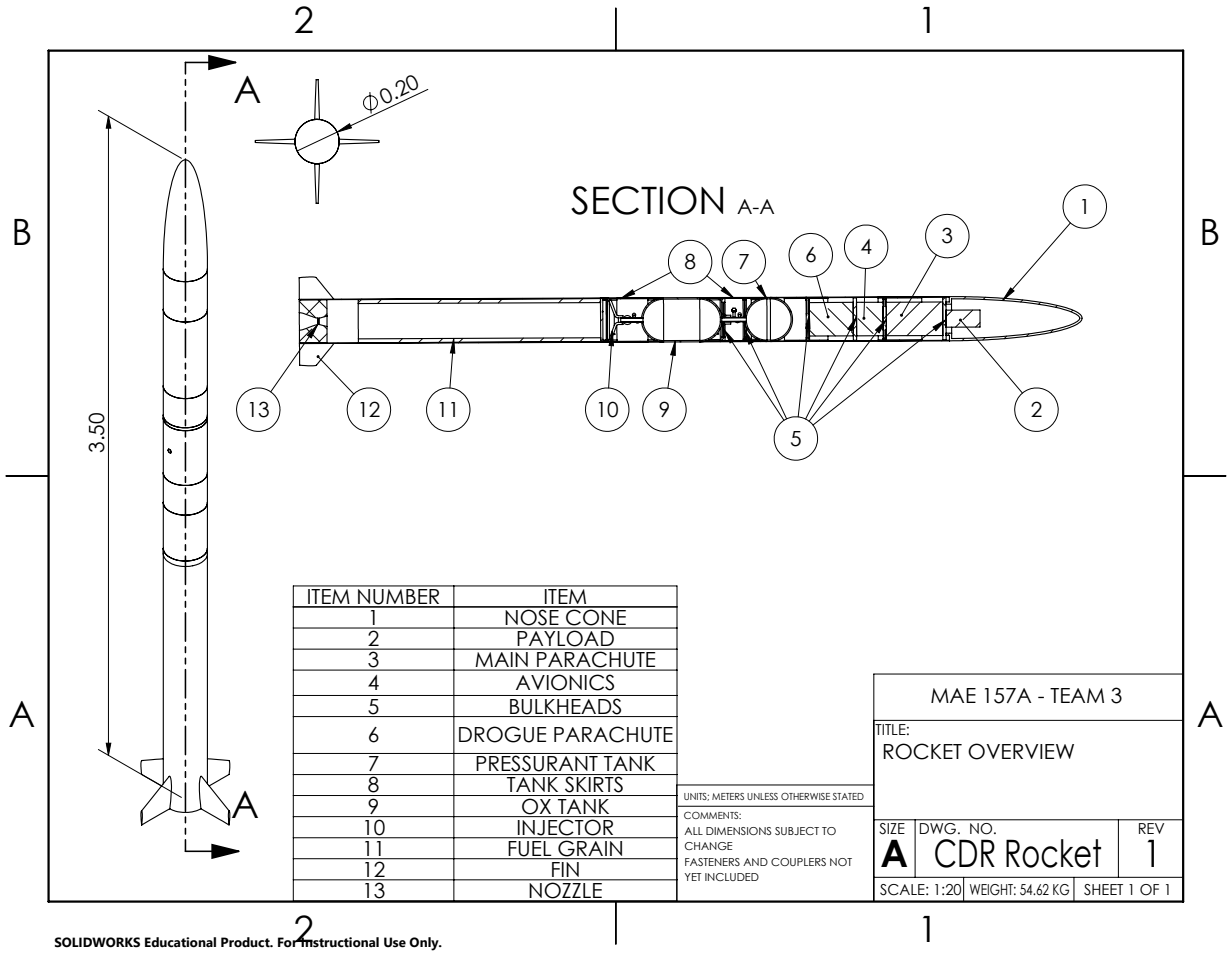

D.2 Recovery System Overview

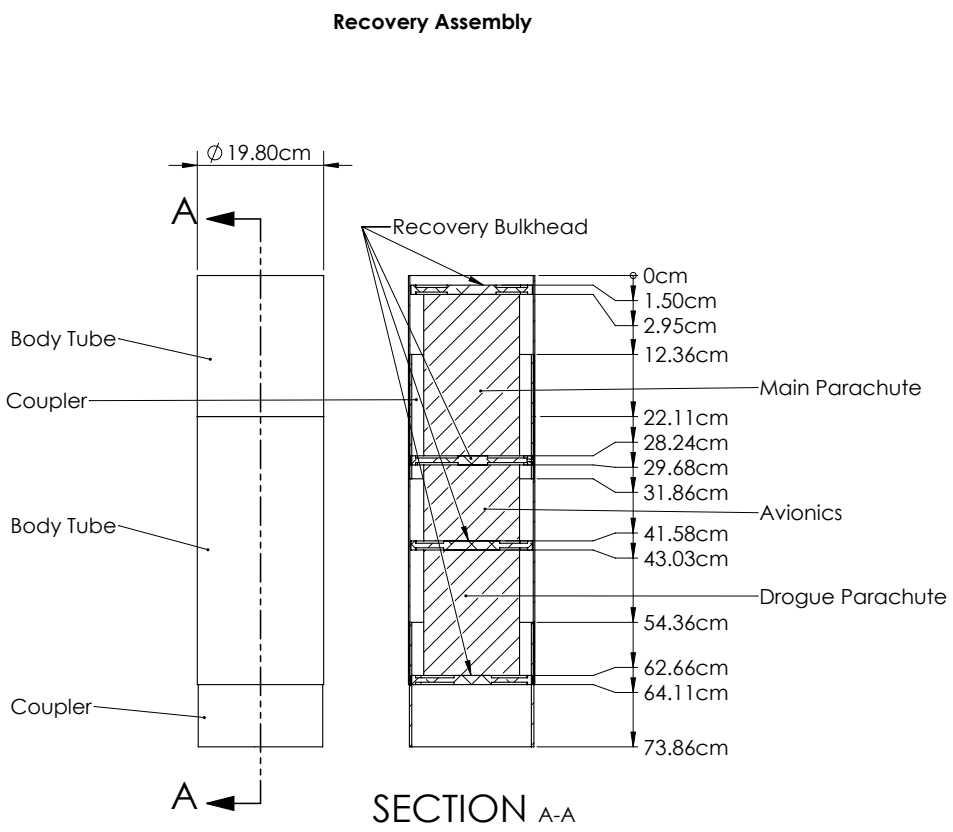

D.3 Motor Overview

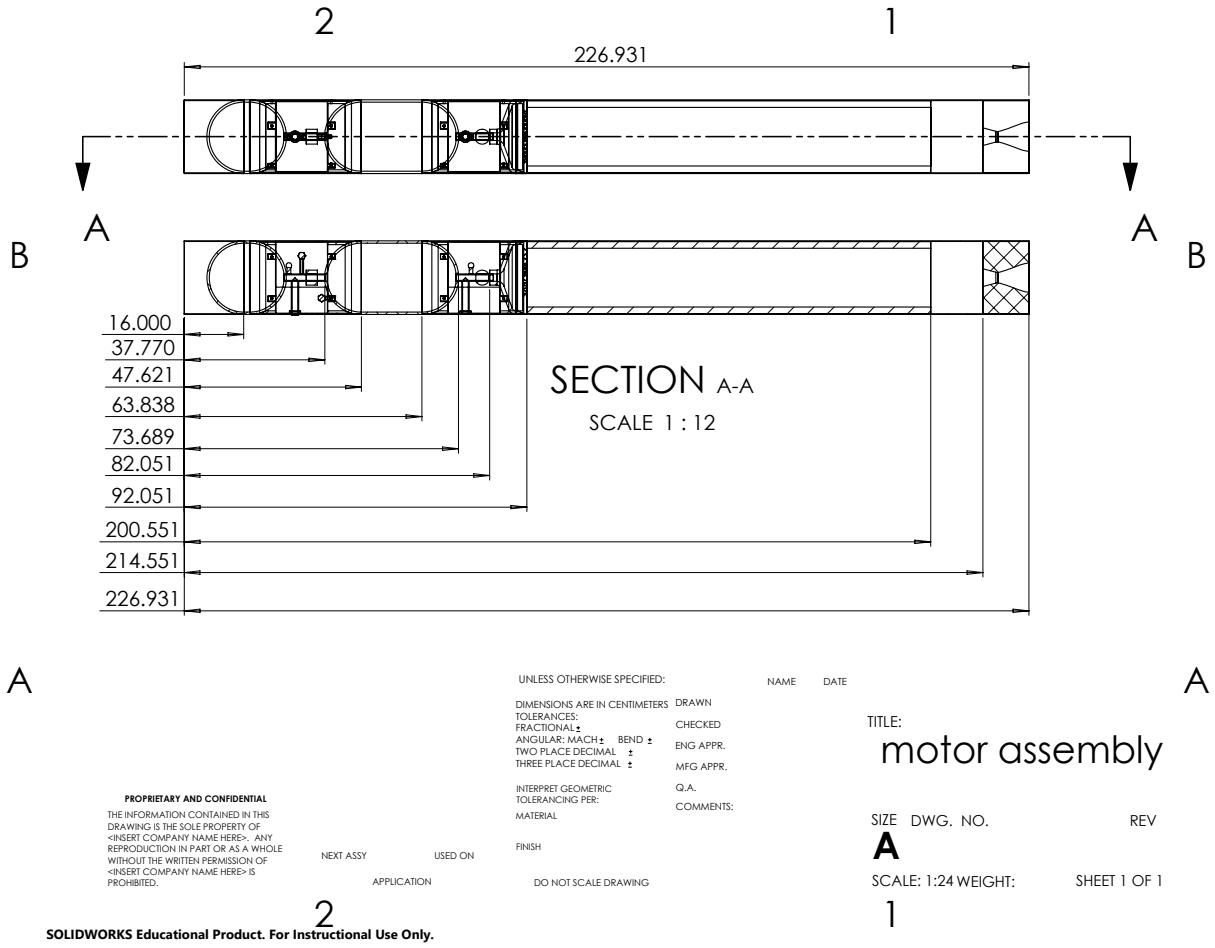

D.4 Bulkheads

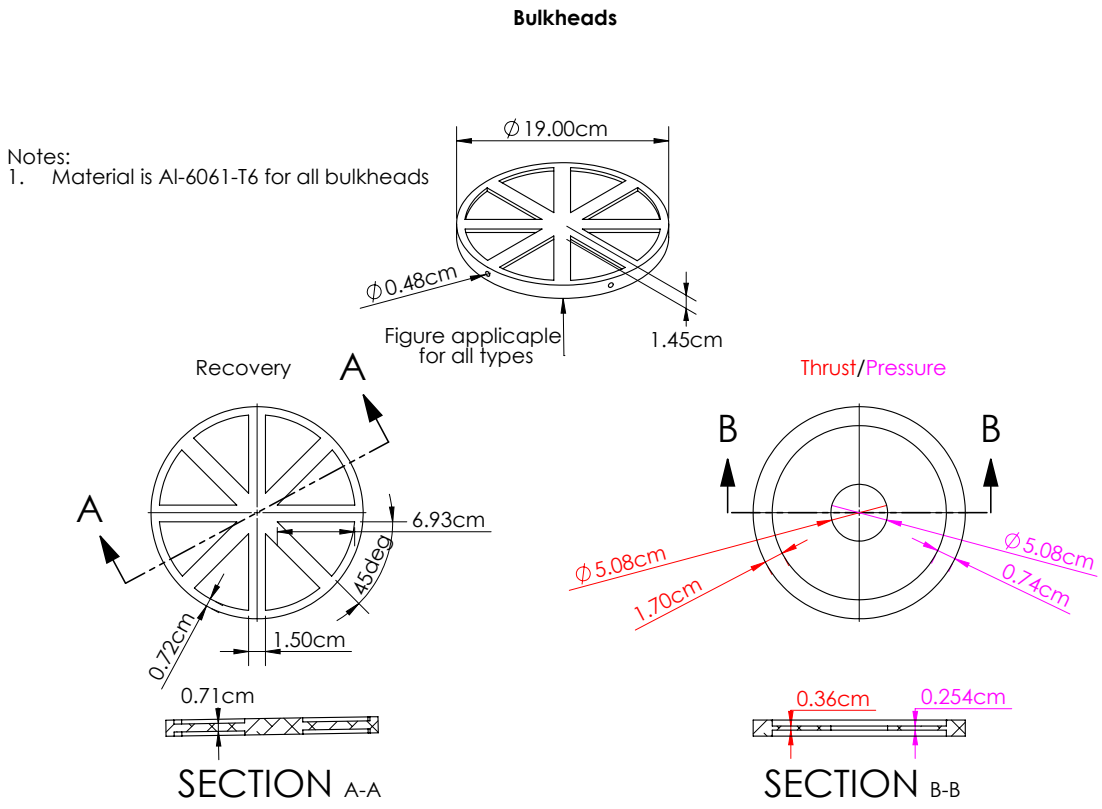

D.5 Pressurant Tank

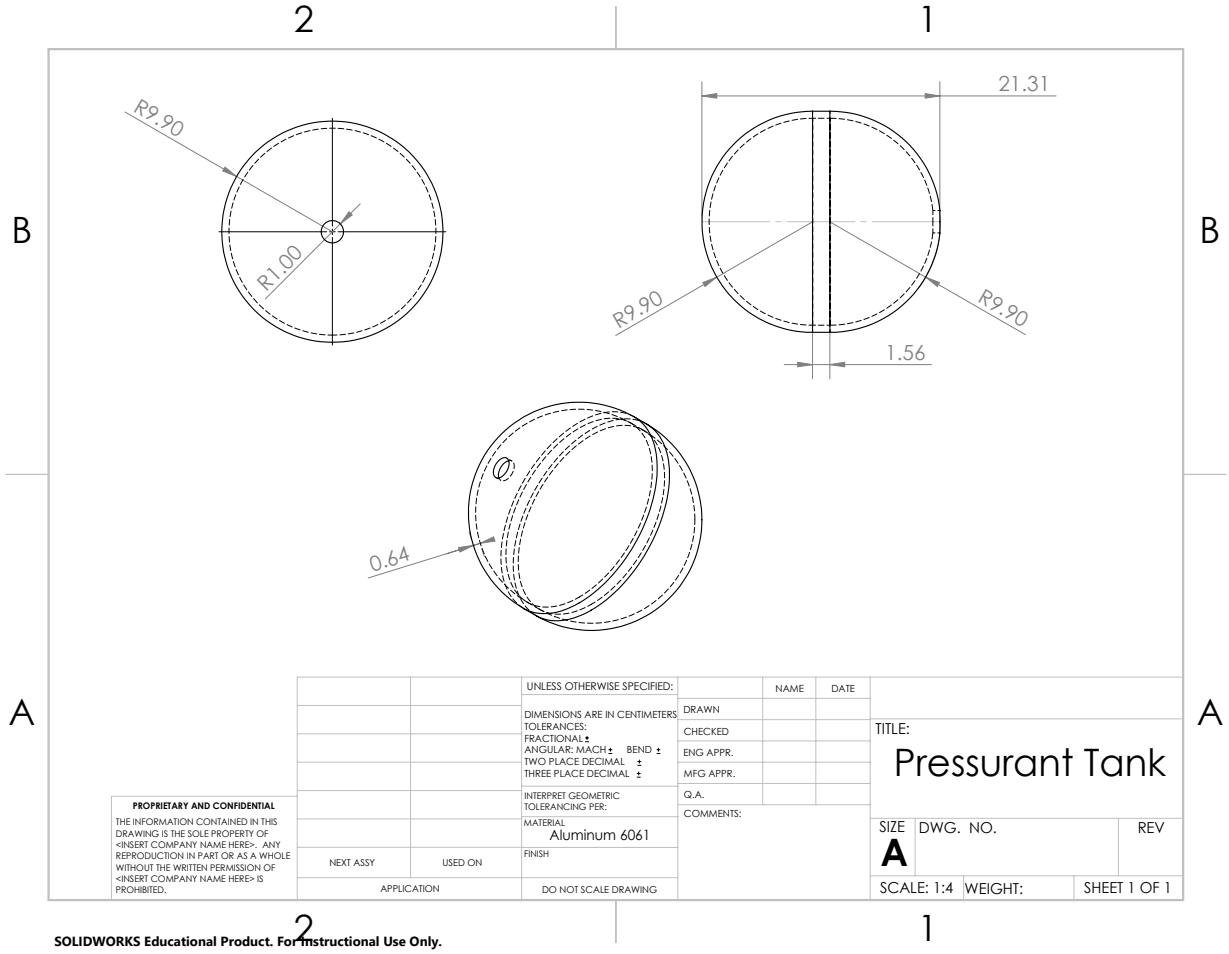

D.6 Oxidizer Tank

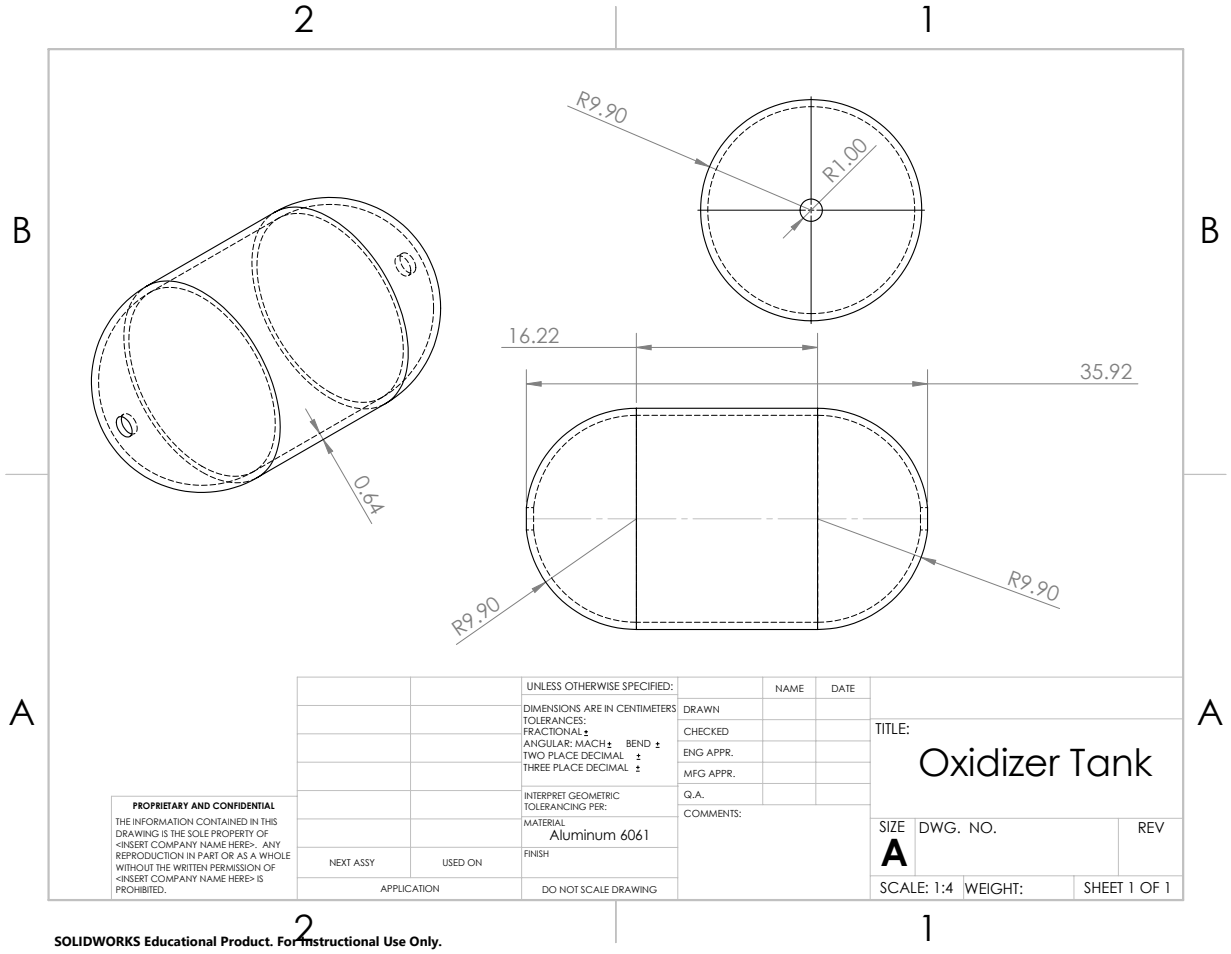

D.7 Tank Skirts

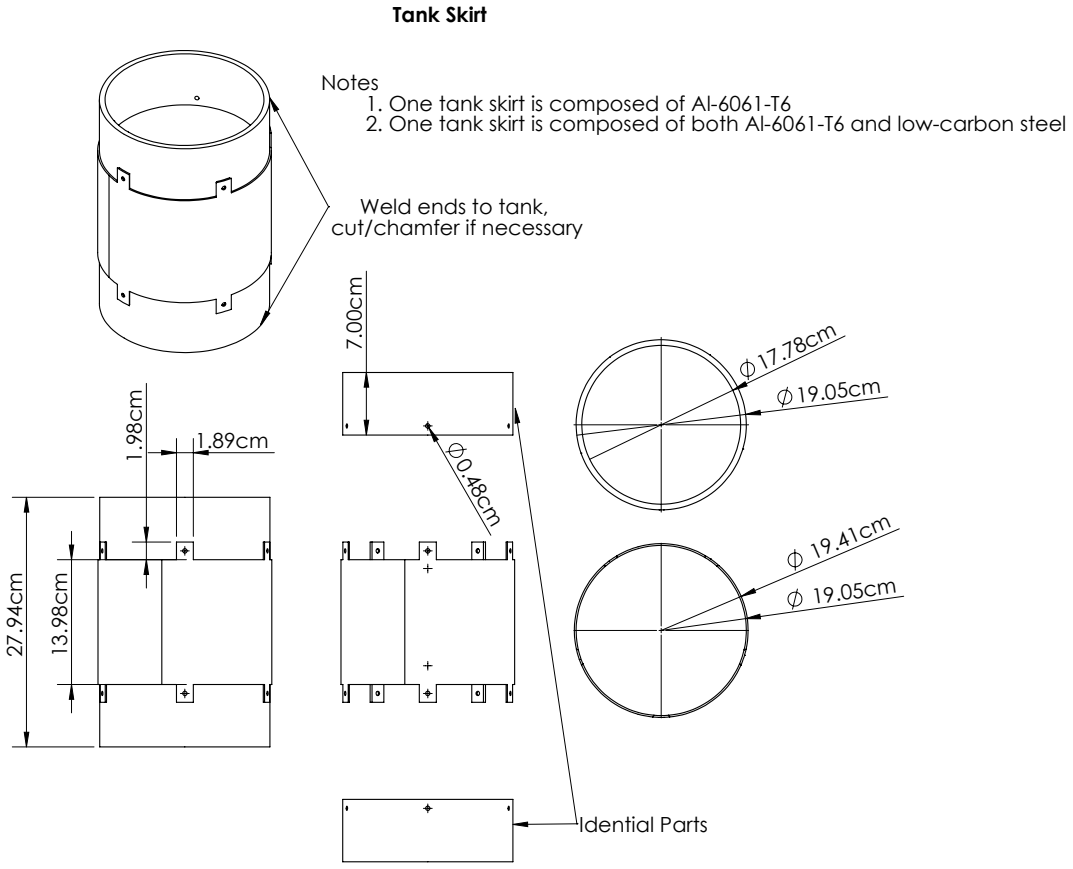

D.8 Injector

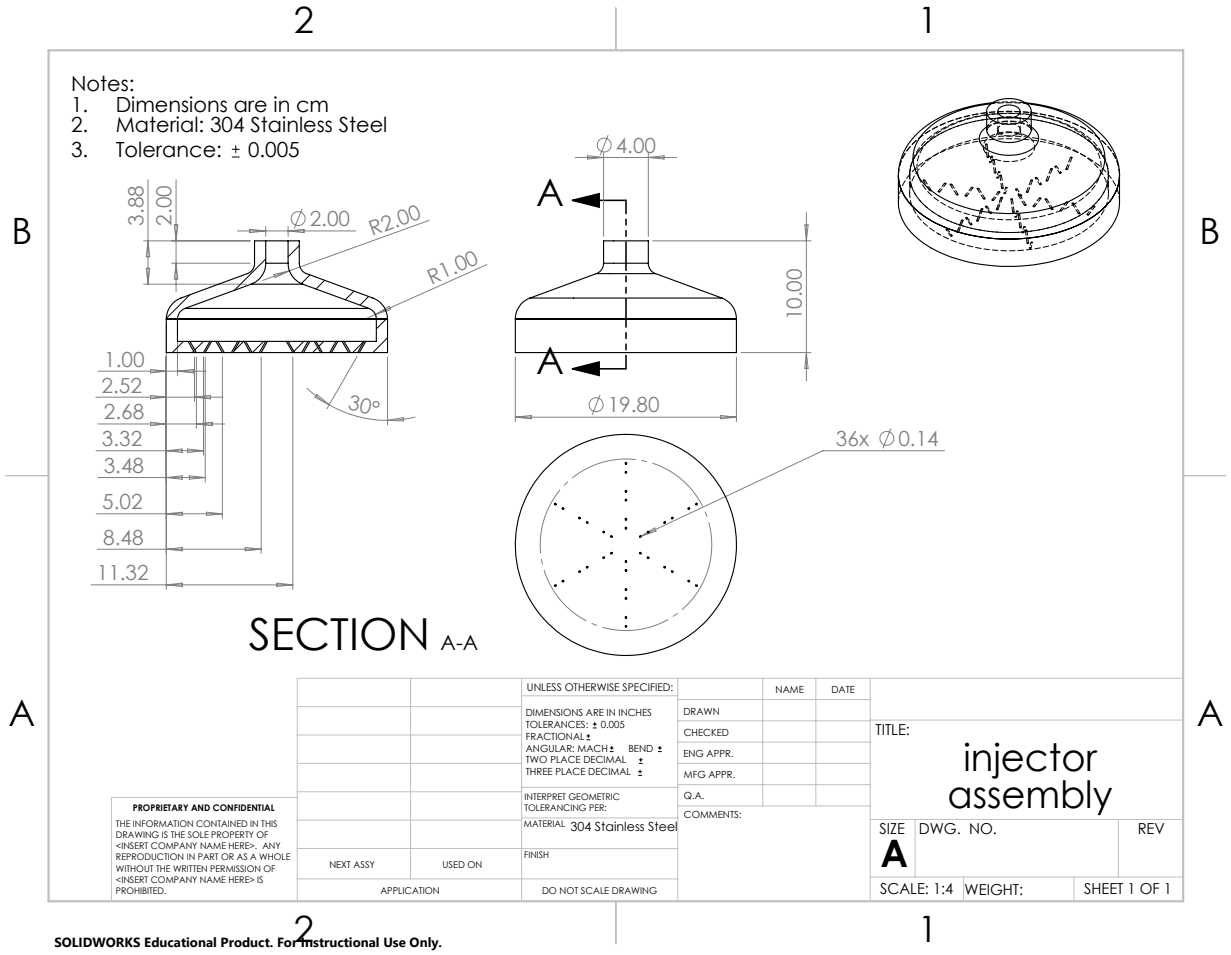
2
1
B
B
A
A
Notes:
1. Dimensions are in cm
2. Material: 304 Stainless Steel
3. Tolerance: ± 0.005
3.88
2.00
∅2.00
R2.00
R1.00
1.00
2.52
2.68
3.32
3.48
5.02
8.48
11.32
30°
SECTION A-A
∅4.00
A
A
10.00
∅19.80
36x ∅0.14
UNLESS OTHERWISE SPECIFIED:
DIMENSIONS ARE IN INCHES
TOLERANCES: ± 0.005
FRACTIONAL ±
ANGULAR: MACH ± BEND ±
TWO PLACE DECIMAL ±
THREE PLACE DECIMAL ±
INTERPRET GEOMETRIC TOLERANCING PER:
MATERIAL 304 Stainless Steel
FINISH
DO NOT SCALE DRAWING
NAME
DATE
DRAWN
CHECKED
ENG APPR.
MFG APPR.
Q.A.
COMMENTS:
TITLE:
injector assembly
SIZE A
DWG. NO.
REV
SCALE: 1:4
WEIGHT:
SHEET 1 OF 1
NEXT ASSY
USED ON
APPLICATION
PROPRIETARY AND CONFIDENTIAL
THE INFORMATION CONTAINED IN THIS DRAWING IS THE SOLE PROPERTY OF <INSERT COMPANY NAME HERE>. ANY REPRODUCTION IN PART OR AS A WHOLE WITHOUT THE WRITTEN PERMISSION OF <INSERT COMPANY NAME HERE> IS PROHIBITED.
SOLIDWORKS Educational Product. For Instructional Use Only.

D.9 Nozzle

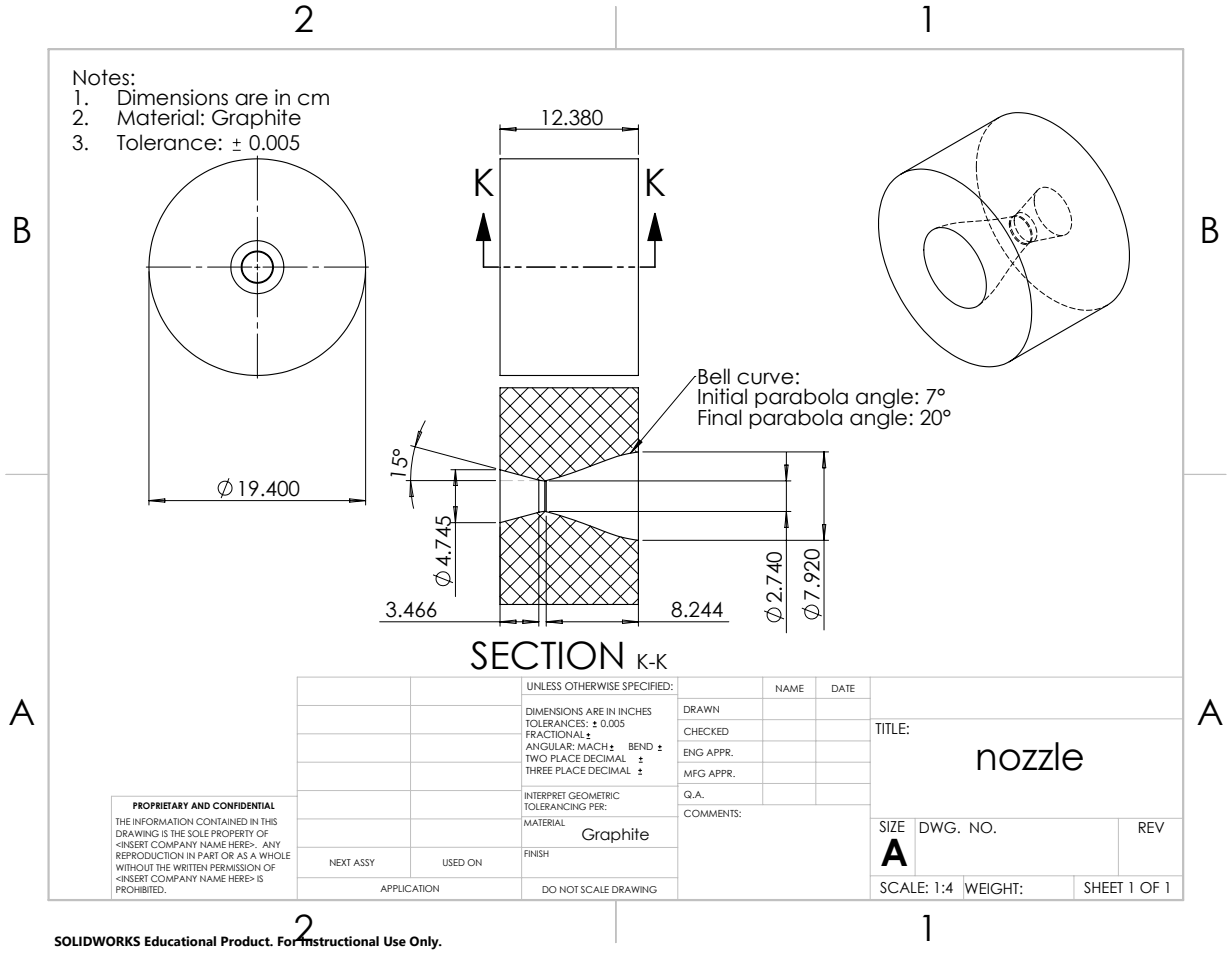
Notes:
1. Dimensions are in cm
2. Material: Graphite
3. Tolerance: ± 0.005
12.380
K
K
Bell curve:
Initial parabola angle: 7°
Final parabola angle: 20°
15°
∅19.400
∅4.745
∅2.740
∅7.920
3.466
8.244
SECTION K-K
UNLESS OTHERWISE SPECIFIED:
DIMENSIONS ARE IN INCHES
TOLERANCES: ± 0.005
FRACTIONAL ±
ANGULAR: MACH ± BEND ±
TWO PLACE DECIMAL ±
THREE PLACE DECIMAL ±
INTERPRET GEOMETRIC TOLERANCING PER:
MATERIAL
Graphite
FINISH
DO NOT SCALE DRAWING
NAME
DATE
DRAWN
CHECKED
ENG APPR.
MFG APPR.
Q.A.
COMMENTS:
TITLE:
nozzle
SIZE
A
DWG. NO.
REV
SCALE: 1:4
WEIGHT:
SHEET 1 OF 1
NEXT ASSY
USED ON
APPLICATION
PROPRIETARY AND CONFIDENTIAL
THE INFORMATION CONTAINED IN THIS DRAWING IS THE SOLE PROPERTY OF <INSERT COMPANY NAME HERE>. ANY REPRODUCTION IN PART OR AS A WHOLE WITHOUT THE WRITTEN PERMISSION OF <INSERT COMPANY NAME HERE> IS PROHIBITED.
SOLIDWORKS Educational Product. For Instructional Use Only.